用于多比特量子存储器的低温离子阱系统

Cryogenic Trapped-Ion System for Multiqubit Quantum Memory

(申请清华大学工学硕士学位论文)

培 养 单 位 ： 计算机科学与技术系

学　　科 ： 计算机科学与技术

研 究 生 ： 薛 瑞 尼

指 导 教 师 ： 郑 纬 民　教 授

副指导教师 ： 陈 文 光　教 授

二〇二三年三月

Cryogenic Trapped-Ion System for Multiqubit Quantum Memory

Thesis submitted to

Tsinghua University

in partial fulfillment of the requirement

for the degree of

Master of Science

in

Computer Science and Technology

by

Xue Ruini

Thesis Supervisor: Professor Zheng Weimin

Associate Supervisor: Professor Chen Wenguang

March, 2023

学位论文指导小组、公开评阅人和答辩委员会名单

指导小组名单

李 1XX	教授	清华大学
王 XX	副教授	清华大学
张 XX	助理教授	清华大学

公开评阅人名单

刘 XX	教授	清华大学
陈 XX	副教授	XXXX 大学
杨 XX	研究员	中国 XXXX 科学院 XXXXXXX 研究所

答辩委员会名单

主席	赵 XX	教授	清华大学
委员	刘 XX	教授	清华大学
	杨 XX	研究员	中国 XXXX 科学院 XXXXXXX 研究所
	黄 XX	教授	XXXX 大学
	周 XX	副教授	XXXX 大学
秘书	吴 XX	助理研究员	清华大学

关于学位论文使用授权的说明

本人完全了解清华大学有关保留、使用学位论文的规定，即：

清华大学拥有在著作权法规定范围内学位论文的使用权，其中包括：（1）已获学位的研究生必须按学校规定提交学位论文，学校可以采用影印、缩印或其他复制手段保存研究生上交的学位论文；（2）为教学和科研目的，学校可以将公开的学位论文作为资料在图书馆、资料室等场所供校内师生阅读，或在校园网上供校内师生浏览部分内容；（3）按照上级教育主管部门督导、抽查等要求，报送相应的学位论文。

本人保证遵守上述规定。

作者签名：_____　　导师签名：_____

日　　期：_____　　日　　期：_____

摘 要

量子存储器是量子技术的一个重要组成部分，它在量子计算机和量子网络中得到了广泛的应用，而存储寿命和容量是表征其性能的两个重要因素。得益于控制性与扩展性，离子阱系统展现出了其利于量子存储和量子计算的能力，并且被认为是最先进的平台之一。

我们设计、搭建并检验了这套离子阱系统。这个物理装置的性能达到了世界一流水平，表现在：其常温区真空度达到了 3×10^{-10} mbar，能够实现多离子稳定囚禁，实验数据证明对于离子数超过 200 的一维离子链能够囚禁 24 小时以上，通过测量多离子 zig-zag 构型的寿命等方法可以估算出低温区域的真空度低于 1×10^{-12} mbar；精巧的机械和光学设计使其具有进行量子计算的潜力，振动和电学噪声得到很大的抑制；使用协同冷却技术极大地提升了其作为量子存储器的存储寿命和容量。在这套系统中，我们探索并实现了一种进行多离子稳定囚禁的方法，并将整个过程标准化使其成功经验能够被复制；在这套标准化的流程中，我们将重要环节精细化，包括真空腔体的处理、获取超高真空的流程、光学模块的搭建、电子控制模块中硬件系统和软件系统的优化；同时我们也实现了离子囚禁和量子操控的自动化，得益于此我们可以进一步探索多离子稳定囚禁的上限。在实验技术上，我们实现了高保真度的初态制备和末态探测（基于 EMCCD 的空间可分辨的探测系统使得不同离子之间的串扰很小，保真度达到 97%），分析并压制了来自于机械和电学系统的造成退相干的噪声来源。

利用这个离子阱系统，我们实现了在 zig-zag 构型中稳定地捕获 200 个以上的离子，并通过测量几个任意选择的离子的相干时间，证明了多量子比特容量和长存储寿命的结合，其相干时间为数百毫秒。我们比较了有无协同冷却激光下的量子存储器的性能，从而毫不含糊地表明协同冷却对于长时间存储多个离子量子比特的必要性。

通过这项工作，我们展现了离子阱系统可以作为一种强大的量子存储器，其长时间连贯存储大量量子比特的能力对于未来具有深度电路的量子计算任务来说是至关重要的。

关键词：离子阱；冷阱；量子计算；量子存储器

ABSTRACT

The quantum memory is an important building block in quantum technology, which is widely used in quantum computing and quantum networks, and storage lifetime and capacity are two important factors to characterize the performance of a quantum memory. Owing to its controllability and scalability, the trapped ion system has demonstrated its ability to facilitate quantum memory and quantum computing, and is considered to be one of the most advanced platforms.

We have designed, built and tested this trapped ion system. The performance of this physical device is state-of-the-art, as evidenced by: a pressure of 3×10^{-10} mbar in the room temperature region, the ability to achieve multi-ion stable trapping, experimental data demonstrating that one-dimensional ion chains with ion numbers over 200 can be trapped for more than 24 hours, the pressure in the cryogenic region can be estimated to be below 1×10^{-12} mbar, for example by measuring the lifetime of the multi-ion zig-zag configuration; the delicate mechanical and optical design provides the capability for quantum computing, with significant suppression of vibration and electrical noise; the use of sympathetic cooling technique greatly enhances its storage lifetime and capacity as a quantum memory. In this system, we have explored and implemented a method for multi-ion stable trapping and standardized the process so that this device is abled to be replicated; in this standardized process, we have refined important aspects, including the handling of the vacuum chamber, the process of obtaining ultra-high vacuum, the construction of the optical module, and the optimization of the hardware and software systems in the electronic control module; we have also automated the process of ion trapping and quantum manipulation, thanks to which we can further explore the upper limits of stable trapping of multiple ions.

In terms of experimental techniques, we have achieved high fidelity initial state preparation and final state detection (the EMCCD-based spatially resolvable detection system allows for minimal crosstalk between different ions with a fidelity of 97%), analyzed and suppressed the sources of noise from mechanical and electrical systems that induce decoherence.

Here we report the stable trapping of above 200 ions in a zig-zag structure, and demonstrate the combination of the multi-qubit capacity and long storage lifetime by mea-

suring the coherence time of several arbitrarily chosen ions to be on the order of hundreds of milliseconds. We compare the performance of the quantum memory with and without the sympathetic cooling laser, thus unambiguously show the necessity of sympathetic cooling for the long-time storage of multiple ionic qubits.

With this work, we show that trapped ion systems can act as a powerful quantum memory, and that their capability to coherently store a large number of qubits for long time is crucial for the quantum computing tasks in the future with deep circuit depth.

Keywords: Trapped Ions; Cryogenic Trap; Quantum Computing; Quantum Memory

LIST OF FIGURES

LIST OF TABLES

LIST OF SYMBOLS AND ACRONYMS

PI	聚酰亚胺
MPI	聚酰亚胺模型化合物，N-苯基邻苯酰亚胺
PBI	聚苯并咪唑
MPBI	聚苯并咪唑模型化合物，N-苯基苯并咪唑
PY	聚吡咙
PMDA-BDA	均苯四酸二酐与联苯四胺合成的聚吡咙薄膜
MPY	聚吡咙模型化合物
As-PPT	聚苯基不对称三嗪
MAsPPT	聚苯基不对称三嗪单模型化合物，3,5,6-三苯基-1,2,4-三嗪
DMAsPPT	聚苯基不对称三嗪双模型化合物（水解实验模型化合物）
S-PPT	聚苯基对称三嗪
MSPPT	聚苯基对称三嗪模型化合物，2,4,6-三苯基-1,3,5-三嗪
PPQ	聚苯基喹噁啉
MPPQ	聚苯基喹噁啉模型化合物，3,4-二苯基苯并二嗪
HMPI	聚酰亚胺模型化合物的质子化产物
HMPY	聚吡咙模型化合物的质子化产物
HMPBI	聚苯并咪唑模型化合物的质子化产物
HMAsPPT	聚苯基不对称三嗪模型化合物的质子化产物
HMSPPT	聚苯基对称三嗪模型化合物的质子化产物
HMPPQ	聚苯基喹噁啉模型化合物的质子化产物
PDT	热分解温度
HPLC	高效液相色谱（High Performance Liquid Chromatography）
HPCE	高效毛细管电泳色谱（High Performance Capillary lectrophoresis）
LC-MS	液相色谱-质谱联用（Liquid chromatography-Mass Spectrum）
TIC	总离子浓度（Total Ion Content）
ab initio	基于第一原理的量子化学计算方法，常称从头算法
DFT	密度泛函理论（Density Functional Theory）
E_a	化学反应的活化能（Activation Energy）
ZPE	零点振动能（Zero Vibration Energy）
PES	势能面（Potential Energy Surface）
TS	过渡态（Transition State）
TST	过渡态理论（Transition State Theory）

$\Delta G^{\neq}$	活化自由能（Activation Free Energy）
κ	传输系数（Transmission Coefficient）
IRC	内禀反应坐标（Intrinsic Reaction Coordinates）
ν_i	虚频（Imaginary Frequency）
ONIOM	分层算法（Our own N-layered Integrated molecular Orbital and molecular Mechanics）
SCF	自洽场（Self-Consistent Field）
SCRF	自洽反应场（Self-Consistent Reaction Field）

CHAPTER 1 INTRODUCTION

1.1 Trapped-ion system

During the 1950s, Wolfgang Paul and Hans Dehmelt have made significant contributions to the invention and development of the ion trap technology. The first experiment on ion and atom trapping was carried out by Paul's group in Bonn, Germany. They demonstrated the use of a six-pole magnetic field to confine atoms in a beam. Subsequently, they demonstrated that ions with various masses could be separated while passing through this device by utilizing four-pole electrodes with a radio-frequency field overlaid. Since then, the Paul trap[1] has evolved into a mass filter and is utilized extensively in a variety of fields, including mass spectroscopy and ultra-high vacuum pumps.

Trapped ions platform is a promising candidate for quantum computing and quantum simulations for its long coherence time, high fidelity qubit state detection and entanglement. Despite all of these achievements in this field, there is still much room for development. Scalability remains a difficulty. When the number of qubits rises, high-delity detection may be degraded by detection crosstalk, and entanglement techniques may become more complicated, particularly in quantum computing. The quantum information is encoded in a chain of qubits, each of which is a two-level system of the internal states of an ion that has been trapped. Primarily, there are two types of qubits. As a qubit, a metastable excited state and a ground state are selected for the optical qubit. And the other is the hyperfine qubit, which is comprised of two hyperfine levels in the ground-state manifold. The relaxation time T_1 of a hyperfine qubit is unlimited , and the anticipated coherence time T_2 might be greater than one hour utilizing the dynamic decoupling approach. In our lab, we concentrate on manipulations with $^{171}Yb^{+}$ ions, therefore the hyperfine qubit is often employed.

1.2 Quantum computer

The potential capabilities of quantum computers[2-3] are now drawing a significant deal of research attention from the scientific community. As a result, the study of quantum computing has become a central topic of contemporary physics with a vast array of applications. To create universal quantum computing, numerous technologies have been

suggested, including NMR, trapped ions, superconducting circuits, NV core, quantum dots, topological systems, etc[4]. Each has its own benefits and drawbacks. For instance, superconducting circuits benefit greatly from contemporary micro fabrication technologies, which makes superconducting qubits the most acknowledged by electrical engineers. The coherence duration for trapped ions may be as long as an hour, and the gate can be operated with the utmost precision, but at a significantly slower rate. Topological qubits are more difficult to fabricate, but theoretically, the requirements for quantum computing may be significantly reduced with high fidelity and inherent quantum error correcting benefits.

Trapped ions and superconducting circuits are now the most promising possibilities in development. There have been several demonstrations involving tens of qubits, and universal gates can be built with a high degree of accuracy over the threshold necessary for error correction. Especially, quantum superiority is proved by certain NP problems, such as the boson sampling, and numerous devices, including superconducting qubits and photonic qubits, are now capable of exhibiting the potential of quantum computing beyond conventional computers.

1.3 Quantum memory

The quantum memory is an important building block in quantum technology[5]. For long-distance quantum communication and quantum cryptography, it lies at the core of the quantum repeater protocol which has an exponential improvement in the communication efficiency[6-7]. For quantum computation, it synchronizes the qubits by appending identity gates between different quantum operations, and it allows the preparation of ancilla states in advance, which comprises the major cost of the fault-tolerant quantum computing[8-9]. Furthermore, matter qubits like trapped ions and superconducting circuits[10] by themselves can be regarded as quantum mem-ories, whose performance fundamentally bounds those of all the quantum operations on these qubits.

Several figures of merit are used to characterize a quantum memory, such as its storage delity, lifetime and capacity[5]. For applications in quantum networks, conversion delity and efficiency between matter qubits and photonic qubits are also concerned. For example, atomic ensembles have demonstrated single-excitation storage lifetime around 0.2 s[11], single-qubit storage delity of 99% and efficiency of 85%[12], and storage capacity of 105 qubits respectively in individual experiments; solid-state spins based on

rare-earth-doped crystals have achieved storage lifetime of tens of milliseconds[13] and the capacity of tens of temporal modes[14], and a spin ensemble coherence time above 6 hours[15]; the NV center in a diamond has also realized 10-qubit storage for a life-time above one minute[16]. As one of the leading quantum information processing platforms, trapped ions keep the record for the longest single-qubit storage life-time above one hour[17]. Entanglement between ionic and photonic qubits has also been demonstrated[18-22] as a plausible way to scale up the ion trap quantum computer[20,23]. As for the multi-qubit storage capacity, above 100 ions have been trapped in one-dimensional (1D) structure with spatial resolution[24], and the global operation and the individual readout of above 60 ions have also been achieved[25]. Shallow-depth quantum circuits composed of high-delity single-qubit and two-qubit gates have been realized for tens of ions[26-27], which provide an upper bound on the noise for a storage time below milliseconds.

Various laser cooling methods have been used to suppress the thermal motion of the ions such as the Doppler cooling[28], electromagnetic-induced-transparency (EIT) cooling[29-30], polarization gradient cooling[31], and sideband cooling[28].. However, all these cooling mechanisms rely on the transition between internal levels of the ions, thus will destroy the stored quantum information. Previously for the single-ion quantum memory, sympathetic cooling through a different ion species has been exploited[17,32-34]. For longer ion chains, sympathetic cooling has also been achieved via focused laser beams on an optimized small fraction of ions[35]. Here we take this approach to maintain the stability of 218 ions in a quasi-1D zigzag structure by sympathetically cooling the ions in the middle, and demonstrate that the arbitrarily chosen storage ions on the edges can achieve a typical storage lifetime above hundreds of milliseconds. Our work thus showcases the multi-qubit storage capacity and the long storage lifetime of the quasi-1D structure of the trapped ions, which can find applications in deep quantum computing circuits and quantum networks.

CHAPTER 2 ION TRAPPING

2.1 The $^{171}Yb^{+}$ qubit

With a mass factor of 171 and a nuclear spin of 1/2, $^{171}Yb^{+}$ has been selected as the qubit system candidate in our laboratory. In the experiment, we use an RF trap to trap the $^{171}Yb^{+}$ ion. Hyperfine clock states are used to encode the qubit. They are stable against magnetic fluctuations. The two hyperfine states of the $^{2}S_{1/2}$ manifold are encoded as $|\downarrow_z\rangle \equiv |F=0, m_F=0\rangle$ and $|\uparrow_z\rangle \equiv |F=1, m_F=0\rangle$. The $^{2}S_{1/2} \leftrightarrow {}^{2}P_{1/2}$ transition of the $^{171}Yb^{+}$ ion is nearly cyclic, but there are 0.5% of spontaneous emission events that cause the state to decay to $^{2}D_{3/2}$. Consequently, a 935 nm laser is continuously on to repump the state to $^{3}[3/2]_{1/2}$ and subsequently decays back to $^{2}S_{1/2}$ in order to finish the cycle transition. By addressing the transition $^{2}S_{1/2} \leftrightarrow {}^{2}P_{1/2}$ with a 370 nm laser, Doppler cooling, optical pumping, and state detection may be achieved. With the use of acoustic-optic modulator (AOM) and electro-optic modulator (EOM), we put all these operations into practice.

2.1.1 Two-photon ionization

Generating an ion and loading it into a Paul trap is the first step towards a trapped-ion quantum computer. The energy necessary to ionize neutral ytterbium to $^{171}Yb^{+}$ ion is at least a photon with the wavelength below 198.2 nm in the FUV zone, which is hard to produce as a laser. Instead, we adopt a two-photon ionization method to produce $^{171}Yb^{+}$ with a single valance electron through the intermediate level $^{1}P_{1}$. An enriched Ytterbium atomic source can be used to produce neutral atomic flux towards the trap center. Once the flux is ejected into the trap center, a laser at 398.9110 nm illuminates the region to first ionize the atoms to a highly excited state $^{1}P_{1}$ and then another laser with wavelength below 393.1 nm continuously removes the electron, leaving only a valance electron on the atomic orbits.

Two-photon ionization allows for more precise control of isotope choice. The desired atomic source is often enriched, with an abundance as high as 91.7%, the remainder consists of various natural isotopes, such as ^{174}Yb, ^{172}Yb, ^{168}Yb etc. Assume 50 ions in a large-scale trapped-ion quantum computer, and the average number of dark isotopes is 4. Thankfully, the intermediate level 398.91 nm transition exhibits an isotope-shift, which

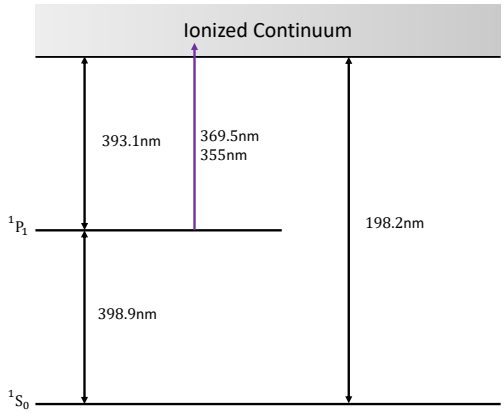

Figure 2.1 Two-photon ionization scheme on $^{171}Yb^+$.

may be used to differentiate between isotopes. Doppler shift is a practical consideration that requires further care. The 398.91 nm laser is oriented perpendicular to the atomic flux to mitigate the Doppler effect. Isotope-selective loading of ions is possible in this setup, increasing the likelihood of the desired isotope, and this may be improved by decreasing the power of the 398.91 nm laser to achieve a narrow linewidth , although this might delay loading speed. Clock states, $\left|\downarrow_z\right\rangle \equiv \left|F=0, m_F=0\right\rangle$ and $\left|\uparrow_z\right\rangle \equiv \left|F=1, m_F=0\right\rangle$, encode the qubit. Doppler cooling, optical pumping and state detection all employ the cyclic transition between the $6^2P_{1/2}$ states and the ground state $6^2S_{1/2}$. A magnetic field applied externally causes a splitting of the $|F=1\rangle$ manifolds through the Zeeman effect at a rate of roughly 1.4 MHz/G, whereas the second-order Zeeman effect dominates the clock qubits at a rate of about 310 Hz/G^2.

Routine ion loading procedures include directing an atomic beam to the loading zone, where several laser beams are utilized to photoionize the atoms. A needle and some shards of metal are all that make up the oven, enriched in ^{174}Yb and ^{171}Yb in separate ovens. On the outside, a current loop is created by connecting the needle's head and tail with Kapton wires to the positive and negative terminals of the power supply. No part of the needle should be anchored to the floor of the chamber. That's because doing so would generate a substantial current to flow into the ground. Since current flows preferentially toward a lower potential, this phenomena may be prevented by isolating the negative poles of the current source from the ground. Keep in mind that while powering the oven for the first time, we must increase the current gradually so as not to accidentally ignite it and safeguard the SAES pump. The first time you use an oven, numerous grimy items will likely be fired out, which might cause the SAES gauge current to rise to the order of A. The atoms are expelled into the trap's central zone after the oven is heated for several

minutes.

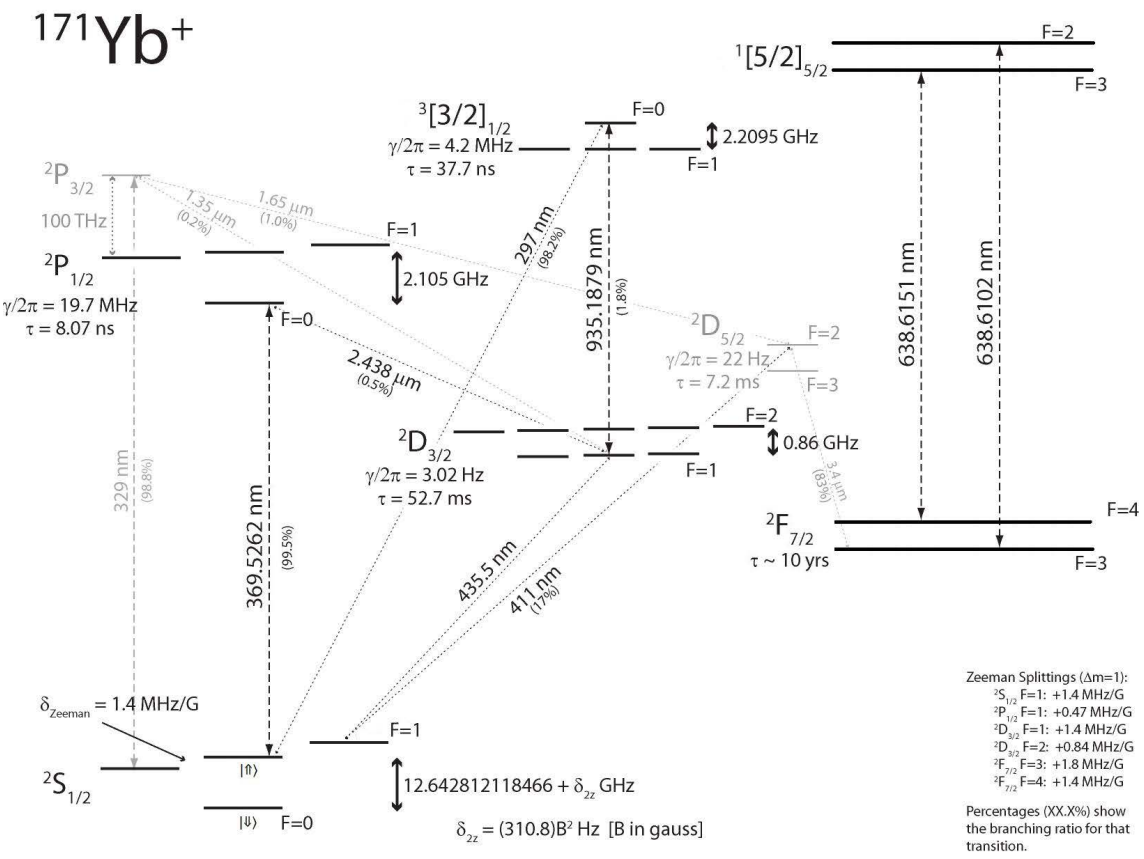

Figure 2.2 $^{171}Yb^{+}$ energy level diagram.

2.1.2 Doppler cooling

Ions have too wide of a motional area to be detected after they have been loaded into the trap since they are still very hot. We must first cool down the heated ions and produce the Coulomb crystal in order to stabilize and crystallize them. Doppler cooling is a method of rapidly cooling ions by utilizing a cyclic transition whose excited state has a very short lifetime and, therefore, a very high cooling rate. Doppler cooling is achieved in the $^{171}Yb^{+}$ system using a red-detuned laser to access $6^2P_{1/2}$ levels with a lifetime of around 8.12 ns, a natural linewidth of 19.6 MHz, and a transition of 369.5263 nm.

Doppler cooling of ions is shown in a simplified model, where ion micromotion is disregarded and the trapping potential is represented by the time-independent pseudo harmonic potential $V(z) = \frac{1}{2}m\omega_z^2 z^2$ just in the z direction. Although the trapped ion's motion is no longer in the quantum domain after Doppler cooling, it can be treated as a classical motion with a velocity that obeys $v(t) = v_0 \cos(\omega_z t)$. Let us consider the hypothetical case of a single, moving laser interacting with a trapped two-level ion consisting only of

S and P states. One cycle of absorption and spontaneous emission occurs in a time period where the ion's velocity does not vary noticeably if the radiative decay rateof the P-level is significantly bigger than the motional frequency. In this scenario, we may represent the average radiation pressure exerted on an ion as a continuous force that varies with its speed. A photon's absorption causes an ion's momentum to increase by $\Delta\mathbf{p} = \hbar\mathbf{k}$ in the direction of the photon's wave vector, and the ion's subsequent spontaneous emission likewise increases its momentum. After many cycles of absorption and emission, the ion will be slowed when the wave vector contains a component along the direction of motion, but the direction of the momentum kick due to spontaneous emission is random across cycles.

The Doppler cooling limit $T_{\min} = \hbar\Gamma(1+\chi)/\left(4k_B\right)$ can be achieved by laser detuning $\Delta = -\frac{\Gamma}{2}$, where χ is the geometrical factor for spontaneous emission, $\Gamma = \sqrt{1+s}\Gamma_0$ is the effective linewidth broadened by power, s is the saturation parameter and the saturation intensity is $I_{\text{sat}} = \frac{\pi hc\Gamma_0}{3\lambda^3} = 510\ \text{W/m}^2$. In addition, re-pumping $|\downarrow\rangle$ back to the cycled transition necessitates an additional frequency component with a detuning of 14.748 GHz. Moreover, the influence of the hyperfine levels must be taken into account, therefore a laser with a wavelength of 935.1880 nm and a sideband of 3.0695 GHz are needed. The branch ratio from level $6^2P_{1/2}$ to level $5^2D_{3/2}$ is non-zero at 0.5%. Doppler cooling may be employed to achieve a final state with a phonon number below 10, where the crystal is stable against certain heating influences from the environment.

2.1.3 Optical pumping

When the ions have been cooled, the $\left|\downarrow_z\right\rangle$ state is prepared using optical pumping. Laser at 370 nm is stimulated when the $^2\,\mathrm{S}_{1/2}\ \mathrm{F} = 1$ to $^2\mathrm{P}_{1/2}\ \mathrm{F} = 1$ transition occurs. If the ion enters the $^2\mathrm{P}_{1/2}\ \mathrm{F} = 1$ manifold, it may spontaneously decay to any of the $^2\,\mathrm{S}_{1/2}$ states. The ion is $\sim$ 10GHz off resonant from the nearest transition. From the $^2\mathrm{P}_{1/2}\ \mathrm{F} = 1$ state, the ion has a 1/3 chance of decaying to the $\left|\downarrow_z\right\rangle$ state. According to the energy diagram, the optical pumping beam has to include both linear and circular components of polarization.

2.1.4 State detection

An experiment's initial step is always preparing the $\left|\downarrow_z\right\rangle$ ion chain. The next step is to actually do the experiment, followed by analysis. When the $\hat{\sigma}_z$ operator is used for measurements, the $|\uparrow\rangle$ and $\left|\downarrow_z\right\rangle$ states of the ions are the only viable results.

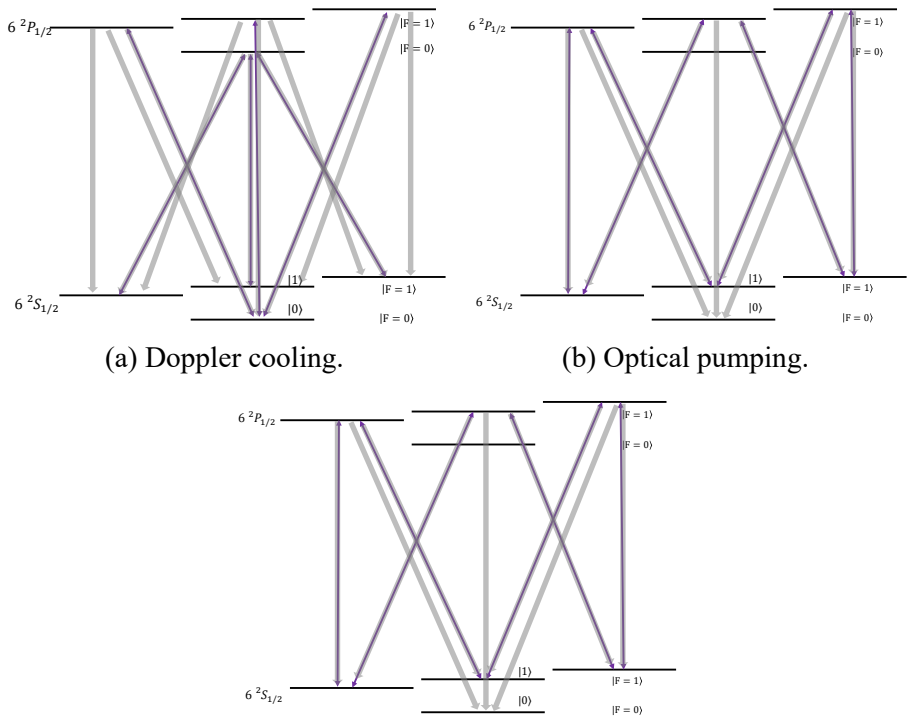

(a) Doppler cooling. (b) Optical pumping.

(c) State detection.

Figure 2.3 The relevant transitions for 369.52 nm laser

It is possible to determine the state of the ion by shining light with a wavelength of 370 nm onto an ion chain that is resonant with the ^{2} $S_{1/2}$ F = 1 to $^2P_{1/2}$ F = 0 transition. This kind of light is known as a detecting light. The detecting light will only resonate with the $|\uparrow\rangle$ state if it is present. It is possible for the ion to decay spontaneously to any of the ^{2} $S_{1/2}$ F = 1 levels. Since it is desirable to have numerous absorption or emission events, the beam has all possible polarization components. This allows the detection process to continue without interruption until sufficient photons have been gathered to determine the ion state. The ion fluoresces isotropically when exposed to the detecting light, and a portion of the light that is emitted by it is gathered by imaging optics and directed onto an EMCCD camera in order to read out the spin state. The detection light has a minuscule chance of off-resonantly exciting either spin state to the $^2P_{1/2}$ F = 1 manifold, where the ion may subsequently decay into the other spin state and induce detection errors. This happens because of the $^2P_{1/2}$ F = 1 manifold.

Doppler cooling, optical pumping, and state detection are all examples of operations that entail spontaneous decay to the ^{2} $S_{1/2}$ F = 1 manifold of states. Hence, if the Zeeman states are degenerate, the mechanism of coherent population trapping may be used to pump the ion into a dark state. As a result, an application of a B-field is made to the ions

in order to disrupt this degeneracy and stop the trapping of coherent populations. In the location where the ions are located, the B-field strength is 5 G, and the Zeeman splitting from the $\left|\uparrow_z\right\rangle$ state is measured 12 MHz.

We are able to determine the state of the spins in the ion chain by capturing the spin-dependent fluorescence using a site-resolving image Andor IXon Ultra 888 EMCCD camera. During the state detection process, a resonant laser with a wavelength of 370 nm is shone between $\left|\uparrow_z\right\rangle$ and $\left|\downarrow_z\right\rangle$. When the qubit is in the $\left|\downarrow_z\right\rangle$ state, a small amount of photons are scattered off, however when the spin state is in the $\left|\uparrow_z\right\rangle$ state, a significant number of photons are scattered off. The binary threshold for spin-state discrimination is determined by calibrating the number of photons dispersed from the bright $\left|\uparrow_z\right\rangle$ state and the dark $\left|\downarrow_z\right\rangle$ state of each spin at the beginning of the process of collecting data on those spins. The bright and dark states of the setup used in this thesis have an average fidelity of more than 97 %, which is suitable for the quantum memory experiments. The off-resonant mixing of spin states during detection, crosstalk between nearby ions, noise from the electronic camera, and noise from the laser are the primary causes of mistake in this case.

2.2 The linear Paul trap

According to one of Maxwell's equations, $\nabla \cdot \vec{E} = 0$, the electric field will not diverge in a region where there is no free charge density. This conclusion may be drawn from the fact that: Earnshaw deduced from this equation that it was mathematically impossible for a charged particle to be connected in a static electric field in all directions at the same time. Yet, in order to condense charged particles, either oscillating electric fields or a combination of static electric and magnetic fields are required. In this experiment, the RF trap is the primary focus.

Assuming for the sake of this discussion that the ions have a positive charge, mathematically express the criteria of an accessible potential that requires minima in any direction as shown below.

$$\frac{\partial \mathbf{E}}{\partial x_i} = -\frac{\partial^2 \Psi}{\partial x_i^2} < 0, x_i \in \{x, y, z\} \tag{2.1}$$

However, Eq. (2.1) contradicts of the Laplacian equation for static electric fields in vacuum, which states that else there would never be a global minimum in any of the directions otherwise $\frac{\partial \mathbf{E}}{\partial x_i} = 0$

$$\nabla^2 \Psi = 0 \tag{2.2}$$

The ion trap technique, which uses a mix of DC and RF oscillating electric fields, offers a fortunate alternative to the traditional method of confining ions in a vacuum environment. It is possible to write down the broad potential of a Paul trap as

$$\Psi(x, y, z) = \frac{U}{2}\left(\alpha x^2 + \beta y^2 + \gamma z^2\right) + \frac{V}{2}\cos(\Omega t)\left(\alpha' x^2 + \beta' y^2 + \gamma' z^2\right) \tag{2.3}$$

$\alpha, \beta, \gamma, \alpha', \beta', \gamma'$ are geometrical factors. A potential of this kind may be generated using hyperbolic electrodes, the geometrical factors involved are precisely $1/r^2$, where r denotes the distance to the electrodes. Unfortunately, the hyperbolic electrodes restrict the optical access. There are some novel designs for traps with high optical access, but the geometrical considerations need to take into account the approximations that are necessary since the hyperbolic electrodes are not ideal. There is an extra restriction for the geometrical factors that must be satisfied in order to satisfy the Laplacian equation

$$\alpha + \beta + \gamma = 0, \quad \alpha' + \beta' + \gamma' = 0 \tag{2.4}$$

To be more specific, a Paul trap with the parameters $\gamma' = 0, \alpha = \beta = -\frac{\gamma}{2}, \alpha' = -\beta'$ is referred to as a linear trap. In a linear trap, charged particles are only confined by a static field in one direction, while RF fields are used to confine them in the other two directions.

2.2.1 Mathieu equation

With a Paul trap, it is possible to decouple the motion of charged particles in three different directions. In this case, we will treat in x for the sake of simplicity following,

$$m\frac{\mathrm{d}^2 x}{\mathrm{d}t^2} = -Q\left(\alpha U x + \alpha' V \cos(\Omega t) x\right) \tag{2.5}$$

substitute $\tau = \frac{\Omega t}{2}, a_x = \frac{4QU\alpha}{m\Omega^2}, q_x = \frac{2QV\alpha'}{m\Omega^2}$, Eq. (2.5) can be simplified as a Mathieu equation

$$\frac{\mathrm{d}^2 x}{\mathrm{d}\tau^2} + \left(a_x x - 2q_x \cos(2\tau) x\right) = 0 \tag{2.6}$$

In this case, the solution of the lowest order is shown together with the assumptions

that $\left|a_x\right|, q_x^2 \ll 1$,

$$\beta_x = \sqrt{a_x + \frac{q_x^2}{2}}, \quad x(t) = 2AC_0 \cos\left(\beta_x \frac{\Omega t}{2}\right)\left[1 - \frac{q_x}{2}\cos(\Omega t)\right] \tag{2.7}$$

This is a bounded solution with periodic frequency $\omega_x = \frac{\beta_x \Omega}{2}$, which is often referred to as secular motion. The second component in frequency $\Omega \pm \omega_x$ represents the intrinsic micromotion that is induced by the RF fields.

In a further approximation, it is possible to construct an effective time-independent potential to describe the dynamics of charged particles in an RF Paul trap. An example in x is presented below, and we assume that the charge is equal to e.

$$E(x,t) = E_0(x)\cos(\Omega t) \tag{2.8}$$

$$F(x,t) = m\ddot{x} = eE_0(x)\cos(\Omega t) \tag{2.9}$$

where $E_0(x)$ is independent of the time-varying potential and solely depends on positional information. Imagine a crystal that has been stabilized such that all of its ions remain in close proximity to their positions of equilibrium. The only new vibrations that occur are those that are caused by the RF fields.

$$x = x_0 - \frac{eE_0(x_0)}{m\Omega^2}\cos(\Omega t) \tag{2.10}$$

This is the first-order solution to the motion, and we may do additional Taylor expansion at the equilibrium location x_0 to the electric field as well, although this is not necessary.

$$\begin{aligned} E_0(x) &= E_0\left(x_0\right) + \left.\frac{\partial E_0(x)}{\partial x}\right|_{x_0}\left(x - x_0\right) \\ &= E_0\left(x_0\right) - \left.\frac{\partial E_0(x)}{\partial x}\right|_{x_0}\left(\frac{eE_0\left(x_0\right)}{m\Omega^2}\cos(\Omega t)\right) \\ &= E_0\left(x_0\right) - \left.\frac{e}{2m\Omega^2}\frac{\partial E_0^2(x)}{\partial x}\right|_{x_0}\cos(\Omega t) \end{aligned} \tag{2.11}$$

$$\begin{aligned} F(x,t) = m\ddot{x} &= eE_0\left(x_0\right)\cos(\Omega t) - \frac{e^2}{2m\Omega^2}\frac{\partial E_0^2(x)}{\partial x}\bigg|_{x_0}\cos^2(\Omega t) \\ &= eE_0\left(x_0\right)\cos(\Omega t) - \frac{e^2}{2m\Omega^2}\frac{\partial E_0^2(x)}{\partial x}\bigg|_{x_0}(1+\cos(2\Omega t))/2 \end{aligned} \tag{2.12}$$

Assess the influence on average, excluding out the variables that are rapidly fluctuating,

$$\bar{F}(x) = -\frac{e^2}{4m\Omega^2}\frac{\partial E_0^2(x)}{\partial x}\bigg|_{x_0} \tag{2.13}$$

where $E_0(x) = -\alpha' V x$ for the general potential, it is a harmonic confinement that does not rely on whether the ions are positively or negatively charged, and it controls the secular motion of ions inside the trap. Additional words include the source of micromotion, which has an oscillation that is much more rapid and is defined by frequency Ω. Hence, one way to define the pseudo potential is as follows,

$$\Psi_{ps} = \frac{e}{4m\Omega^2}E_0^2(x) = \frac{e\alpha'^2V^2}{4m\Omega^2}x^2 \tag{2.14}$$

This re-creates the conclusion that Earnshaw's theorem came to. It is a valid approximation for equilibrium positions and secular motion of charged particles in an RF trap, and it can be used to calculate the principal axes taking both DC and RF fields into account. The secular frequency is $\omega_x = \frac{e\alpha' V}{\sqrt{2}m\Omega}$, which is consistent with the Mathieu equation. The static confinement can also be taken into account, which is also a harmonic term.

2.2.2 Normal modes

Since the normal modes are entirely decoupled from all directions, particularly the transverse modes that we are working on, we employ a chain of trapped $^{171}Yb^{+}$ ions as the quantum memory in a linear Paul trap. This allows us to study the transverse modes. It is necessary for the trap frequencies to adhere to the relation Eq. (2.15) if the Coulomb crystal is to be contained inside a linear chain.

$$\left(\frac{\omega_r}{\omega_z}\right)^2 \geq \frac{N^{1.73}}{2.53} \tag{2.15}$$

where N is the number of ions, ω_r refers to either the transverse mode ω_x or ω_y, and

ω_z refers to the axial mode with DC confinement.

Instead of using the straightforward Mathieu equation, one needs take into consideration the Coulomb interaction that occurs between the ions when there are a greater number of ions fed into the trap. Both the externally imposed pseudo potential and the Coulomb interactions that occur between the ions work together to decide the shape of the ion crystal.

The inter-ion spacings would not be uniform under a harmonic potential similar to Eq. (2.3), where spacings at the center of an ion chain would be much more tight but loose at the edge. This would require much higher RF potential or lower DC potential to satisfy Eq. (2.15), or else there would be an unstable transition to zigzag mode. Here, we consider N ions in In order to solve the issue, quartic potential is required. This is because increasing the number of electrodes along the z-axis will bring the inter-ion spacings closer to being uniform. As the micromotion is negligible in comparison to the secular motion and all of the ions are aligned with the RF null in the required configuration, the property of the ion crystal may be obtained using the pseudo potential while ignoring the time-dependent RF potential.

The potential in its broadest sense may be expressed as

$$U = \sum_i \left(\frac{\alpha}{2} z_i^2 + \frac{\beta}{4} z_i^4 \right) + \sum_{i<j} \frac{e^2}{4\pi\epsilon_0 \left| z_i - z_j \right|} \tag{2.16}$$

Here, we will define the length unit known as $l = \left(e^2 / 4\pi\epsilon_0 \alpha \right)^{1/3}$, and after that, we will be able to rewrite the potential $u_i \equiv z_i / l$ using dimensionless coordinates and dimensionless energy $U' \equiv 4\pi\epsilon_0 l U / e^2$, respectively.

$$U' = \sum_i \left(\frac{1}{2} u_i^2 + \frac{\beta l^2}{4\alpha} u_i^4 \right) + \sum_{i \neq j} \frac{\mathrm{sgn}(\alpha)}{2 \left| u_i - u_j \right|} \tag{2.17}$$

When we have ascertained the total number of ions and the potential configuration $\frac{\beta l^2}{\alpha}$, we will be able to locate the equilibrium locations by minimizing the energy required to do so. Instead, we might try to solve the gradient equations when the system is at equilibrium.

$$0 = \frac{\partial U'}{\partial u_i} = u_i + \frac{\beta l^2}{\alpha} u_i^3 - \mathrm{sgn}(\alpha) \sum_{i \neq j} \frac{u_i - u_j}{\left| u_i - u_j \right|^3} \tag{2.18}$$

We can further reduce the problem to find the solutions of the gradient equations, which is something that can be easily accomplished by some built-in functions of Wolfram Mathematica such as FindRoot or NSolve. As an alternative to performing the optimization with multiple variables, we can use this method.

When the equilibrium locations have been determined, the Hessian matrix may be used to calculate the axial motional modes

$$\frac{\partial^2 U'}{\partial u_i \partial u_j} = \begin{cases} 1 + \frac{3\beta l^2}{\alpha} u_i^2 + \sum_{k \neq i} \frac{2\,\mathrm{sgn}(\alpha)}{\left|u_i - u_k\right|^3}, & i = j \\ -\frac{2\,\mathrm{sgn}(\alpha)}{\left|u_i - u_j\right|^3}, & i \neq j \end{cases} \tag{2.19}$$

Things would turn out differently with regard to the transverse modes. The COM mode has the maximum frequency, and its bandwidth is quite close to that of the axial COM mode; hence, the transverse modes have a significantly higher population density. Moreover, we are able to include the transverse words into the general form.

$$U = \sum_i \left(\frac{\alpha}{2} z_i^2 + \frac{\beta}{4} z_i^4 + \frac{1}{2} m\omega_x^2 x_i^2 + \frac{1}{2} m\omega_y^2 y_i^2 \right) + \sum_{i<j} \frac{e^2}{4\pi\epsilon_0 \left|\mathbf{r_i} - \mathbf{r_j}\right|} \tag{2.20}$$

For a linear chain configuration, the equilibrium positions for transverse x, y are quite clear that $x_0 = 0$, $y_0 = 0$, and we can use the same dimensionless unit l to simplify the potential expression using notation $uz = z/l$, $ux = x/l$, $uy = y/l$,

The equilibrium positions for transverse x and y in a linear chain configuration are quite obvious: $x_0 = 0$, $y_0 = 0$. We can use the same dimensionless unit, l, to simplify the potential expression by notating it as follows: $uz = z/l$, $ux = x/l$, $uy = y/l$. For a linear chain configuration, the equilibrium positions for transverse x and y are quite obvious.

$$\begin{aligned} U' &= \sum_i \left(\frac{1}{2} uz_i^2 + \frac{\beta l^2}{4\alpha} uz_i^4 + \frac{m\omega_x^2}{2\alpha} ux_i^2 + \frac{m\omega_y^2}{2\alpha} uy_i^2 \right) + \sum_{i \neq j} \frac{\mathrm{sgn}(\alpha)}{2\left|\mathbf{u_i} - \mathbf{u_j}\right|} \\ &= U_0 + \sum_i \left(\frac{m\omega_x^2}{2\alpha} ux_i^2 + \frac{m\omega_y^2}{2\alpha} uy_i^2 \right) - \mathrm{sgn}(\alpha) \sum_{i \neq j} \frac{\left(ux_i - ux_j\right)^2 + \left(uy_i - uy_j\right)^2}{4\left|uz_i - uz_j\right|^3} \end{aligned} \tag{2.21}$$

where U_0 is the one only related to coordinates uz_i's. When thinking about the transverse modes, we don't need to take them into account at all since we may ignore them. We may also derive the Hessian matrix for x, y, and the results for x are shown below. As the right hand side of the potential has the same dependency on the sign of α, we can,

in practice, use the absolute value instead.

$$\frac{\partial^2 U'}{\partial u x_i \partial u x_j} = \begin{cases} \frac{m\omega_x^2}{|\alpha|} - \sum_{k \neq i} \frac{1}{\left|uz_i - uz_k\right|^3}, & i = j \\ \frac{1}{\left|uz_i - uz_j\right|^3}, & i \neq j \end{cases} \tag{2.22}$$

2.2.3 Micromotion minimization

Ions in Paul's tarp will go through a process known as forced motion, which is driven by the frequency referred to as Ω. Some of this motion is an intrinsic effect caused by the RF potential, while other motion is caused by forced motion for ions going through a process known as nonzero oscillating force. The force may be created by a residual DC field that moves the ions away from the RF null, and the real-time electric field is not zero. The temporal dependency of the real-time electric field's frequency is characterized by Ω. The motion of ions may, as a matter of course, be explained by the linear superposition of two portions.

$$\begin{aligned} \ddot{x} &= -\omega_x^2 x - \frac{E_0\left(x_0\right) e}{m} \cos(\Omega t) \\ x(t) &= A \cos\left(\omega_x t\right) + B\left(E_0\left(x_0\right)\right) \cos(\Omega t) \end{aligned} \tag{2.23}$$

The periodic force will cause the second term of the solution of $x(t)$, which is given by pseudo potential approximation. The term $B(E_0(x_0))$ is the amplitude of excess micromotion, and it dependends on the strength of the residual electric field $E_0(x_0)$ or the equilibrium position from RF null x_0. In addition, the intrinsic micromotion that is solved by the Mathieu equation is characterized by the frequency $\Omega \pm \omega_x$, and it is related to the transverse secular motion. On the other hand, the excess micromotion are detached from the secular motion. In addition, excess micromotion is degenerate in three directions, and in order to link the micromotion, we require a number of lasers that are not parallel to one another.

In addition to the equation that is described in Eq. (2.23), we are able to utilize the Mathieu equation to determine the motion of the ions in the presence of a stray field, and this motion may be written as

$$\begin{aligned} x(t) &= \left(\frac{eE_R}{m\omega_x^2} + A\cos\left(\omega_x t\right)\right)\left(1 + \frac{q_x}{2}\cos(\Omega t)\right) \\ &= A\cos\left(\omega_x t\right) + \frac{eE_R q_x}{2m\omega_x^2}\cos(\Omega t) + \frac{Aq_x}{2}\cos\left(\omega_x t\right)\cos(\Omega t) + \frac{eE_R}{m\omega_x^2} \end{aligned} \tag{2.24}$$

As can be seen in the figure referenced above, there are four different terms: secular motion, excess micromotion, intrinsic micromotion, and equilibrium position displacement, respectively. Because intrinsic micromotion is born with the RF potential, its amplitude can never be reduced by tinkering with the DC configurations. This is because intrinsic micromotion is only related to the RF potential and the Doppler cooling limit. For secular motion, the amplitude is related to the process of cooling, and $\omega_x = \sqrt{a_x + \frac{q_x^2}{2}}\frac{\Omega}{2}$ for the intrinsic micromotion. It is obvious that the excess micromoiton is associated with the stray field that is exerted on the ions, the amplitude is proportional to $a_x << q_x^2$, in particular for transverse modes in an ion chain, and it can be easily demonstrated that the amplitude will be reduced when increasing the RF level, and in addition to this, the ion position will approach the RF null by factor $\frac{1}{a_x + \frac{q_x^2}{2}}$.

Expanding the electric field is possible within the context of the rotating frame of the ions' secular motion,

$$E(x,t) = E_0 e^{-i\left(\omega_0 t - k_x x(t)\right)} = E_0 e^{ik_x A\cos\left(\omega_x t\right)\left(1+\frac{q_x}{2}\cos(\Omega t)\right)} e^{-i\left(\omega_0 t - \frac{k_x eE_R q_x}{2m\omega_x^2}\cos(\Omega t)\right)} \tag{2.25}$$

So, we are able to make use of the modulation information in order to extract the amplitude of excess micromotion, and the RF modulation may also regulate the fluorescence. A cooling laser is used in this technique to detect the modulation, and of course, non-parallel lasers are required in order to reconstruct the full information of excess micromotion. The fluorescence can be demodulated by using a device called a time-arrival-converter, but this method has some drawbacks. Unfortunately, because of the geometry of the chamber, it is not always possible to send lasers in all three directions, and this difficulty might be considerably more severe for surface planar traps, particularly when the cooling laser is operating in the ultraviolet range. A combination of Raman sideband and EMCCD monitoring ion position is another method that may be used to identify excess micromotion.

In this article, we present the parametric excitation approach for the purpose of min-

imizing excess micromotion because of its ease of use and high degree of accuracy. Although the delivery of laser along the objective might be challenging, the accuracy of micromotion minimization along the objective is completely constrained by the resolution and amplification capabilities of the imaging system. This was covered in the previous section. To be able to detect extra micromotion in any of the three orthogonal directions, parametric excitation just needs a single cooling beam to readily connect to all three directions simultaneously. It is possible to put it into practice by modulating the amplitude of RF fields, using the pseudo potential approximation, the force that is exerted on the ions is

$$\frac{\mathrm{d}^2\bar{x}}{\mathrm{d}t^2} + \xi\frac{\mathrm{d}\bar{x}}{\mathrm{d}t}\omega_x^2\left(1 + 2h\cos\left(\omega_m t\right)\right)\bar{x} = \frac{eE_R}{m} \tag{2.26}$$

where h is the modulation index, $E(r,t) = E_0(r,t)(1 + h\cos(\omega_m t))$, the corresponding pseudo potential is proportional to $E^2(r,t) = E_0^2(r,t)(1 + 2h\cos(\omega_m t))$, and ξ is the damping coefficient of the cooling beam.

The parametric excitation, in contrast to the forced oscillation, will not take place if the initial condition $\bar{x}(0) = 0$, and the parametric excitation will only be excited at the modulation frequency $\omega_m = \frac{2\omega_x}{n}$, where n is a positive integer. The forced oscillation will take place regardless of the initial condition. Depending on the experimental regime, the parametric excitation will either induce a decrease in fluorescence or an increase in it. So, the parametric excitation may be utilized to identify excess micromotion if ions are pushed away from the RF null. Nevertheless, once $\bar{x}$ approaches the equilibrium location of the RF null, the parametric excitation will cease to exist.

In addition, a recent piece of research demonstrates that there is a link between the fluorescence and the amplitude modulation signal. In this example, we will show how parametric excitation may occur when $\omega_m = \omega_x$. The stable solution may be derived by using Floquet theory even in the absence of explicit derivations, which take into account corrections for secular frequency and modulation depth.

$$\bar{x}(t) = \sum_n c_n e^{ic_n\omega_m t} \tag{2.27}$$

$c_n = c_{-n}^*$ for symmetry, and c_0 depends on the first order of modulation, $c_0 = \frac{eE_R}{m\omega_x^2}$.

Then we can extend it to the second order, and we can simplify $\bar{x}(t) = c_0 + 2\mathfrak{R}\left(c_{-1}e^{-i\omega_m t}\right)$, replace it back into Eq. 2.26, and we can easily find the answer for the

second order,

$$|c_{-1}|^2 = \frac{2c_0^2 h^2}{\left(f^2-1\right)+4f^2d^2}, \quad \tan\left(\arg\left(c_{-1}\right)\right) = \frac{2fd}{f^2-1} \tag{2.28}$$

where $f = \frac{\omega_m}{\omega_x}$, $d = \frac{\xi}{\omega_x}$ are normalized frequency and damping factor. The amplitude of c_{-1} is linearly proportional to c_0, and thus E_R.

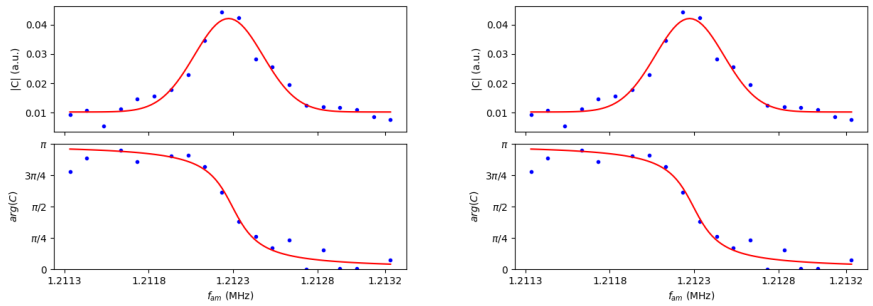

(a) Correlated signal in the x-axis (ω_x). (b) Correlated signal in the y-axis (ω_y).

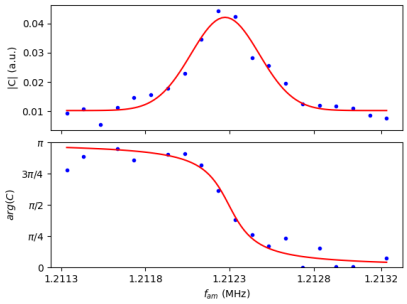

(c) Correlated signal in the z-axis (ω_z).

Figure 2.4 Parametric excitation approach for minimizing excess micromotion.

By scanning the modulation frequency across ω_x, which indicates the resonant frequency, it is obvious that there is a phase shift of π. This phase shift may be aided further by the peak value of c_{-1} that occurs during a frequency scan. The sensitivity is influenced by two factors: (a) the modulation factor h, and (b) the degree to which the modulation frequency is detuned with respect to the secular frequency. Notice that there is a correction to the secular frequency that is related to the modulation, but that it is not represented here. The fundamental physics, however, remains the same.

2.3 Coherent manipulation of ions

The $^{171}Yb^+$ qubits are the primary research topic in our laboratory, the qubit itself is encoded in the ground state manifold's two hyperfine levels. In order to manipulate the

qubit using a laser, one must make use of the Raman transition, which is facilitated by various auxiliary energy levels.

2.3.1 Theory of laser-ion interaction

In this part, I will focus on the interaction of a single ion with the laser. The application of this concept to the situation of several ions is quite simple, with the exception of the laborious indexing required for the normal mode ladder operators. The Halmitonian for the trapped ion that was irradiated by the laser is as follows: $\hat{H} = \hat{H}_0 + \hat{V}$, where $\hat{H}_0$ refers to the non-interacting component and $\hat{V}$ refers to the interaction part. After being cooled by Doppler cooling, it is possible to safely view it as a harmonic oscillator, even if there is just a single ion trapped in the potential. And if we are just concerned with a two-level internal system and a z-axis exterior motion of the ion, then (we shall set $\hbar$ as 1 in the following) $\hat{H}_0 = \omega_0/2\hat{\sigma}_z + \nu\hat{a}^\dagger\hat{a}$, where ω_0 operator for the annihilation of the z-axis motion. We now deduce the laser-ion interaction, denoted by the symbol $\hat{V}$; however, we only take into account the electric-field component of the laser and use a semi-classical point of view, this means that the laser field is not quantized,

$$\mathbf{E} = \frac{\mathbf{E}_0}{2}\left(e^{i(\omega_L t - \mathbf{k}\cdot\mathbf{R} + \varphi_L)} + e^{-i(\omega_L t - \mathbf{k}\cdot\mathbf{R} + \varphi_L)}\right), \tag{2.29}$$

where $\mathbf{R}$ represents the position vector of the ion, $\mathbf{E}_0$ represents the amplitude of the laser field, ω_L represents the frequency of the laser field, and φ_L represents the phase of the laser field. In this context, we will use the example of dipole interaction. The location of the ion along the z axis may be expanded by the ladder operator, $\hat{z} = \bar{z} + z_0(\hat{a}^\dagger + \hat{a})$, where $\bar{z}$ is the average position, z_0 is the motional extent, and $\hat{a}\,(\hat{a}^\dagger)$ was just described above. The motional extent is the distance traveled by the ion along the z axis. The dipole interaction Hamiltonian might therefore be written as

$$\hat{V} = -e\left(\mathbf{r}_{eg}\hat{\sigma}_+ + \mathbf{r}_{eg}\hat{\sigma}_-\right)\cdot\frac{\mathbf{E}_0}{2}\left(e^{i\left(\omega_L t - \eta\left(\hat{a}^\dagger + \hat{a}\right) + \phi\right)} + \text{ H.c. }\right), \tag{2.30}$$

where $\mathbf{r}_{eg} = \langle e|\hat{\mathbf{r}}|g\rangle, \hat{\sigma}_+\left(\hat{\sigma}_-\right)$is $|e\rangle\langle g|(|g\rangle\langle e|), \eta = z_0 k\cos\theta$ is a parameter derived from the Lamb-Dicke equation that describes the relationship between the ion-motional extent and the laser wavelength. This parameter is often considerably less than 1, and in our configuration, it is between $0.07 - 0.09$ away from a transverse mode. And $\phi = \varphi_L - k\cos\theta\bar{z}$ is just a re-defined laser phase factor. In the formulas that have come

before, the symbol θ refers to the angle that exists between the laser wave vector $\mathbf{k}$ and the ion-motional axis z. We put the whole Hamiltonian into the interaction picture of the uncoupled Hamiltonian, $\hat{H}_0$ with $\hat{U}_0 = e^{i\hat{H}_0 t}$,

$$\begin{aligned}\hat{H}_I &= \hat{U}_0 \hat{H} \hat{U}_0^\dagger - i\hat{U}_0 \frac{\partial \hat{U}_0^\dagger}{\partial t} \\ &= -e\left(\mathbf{r}_{eg}\hat{\sigma}_+ e^{i\omega_0 t} + \mathbf{r}_{eg}\hat{\sigma}_- e^{-i\omega_0 t}\right) \cdot \frac{\mathbf{E}_0}{2}\left(e^{i\left(\omega_L t - \eta\left(\hat{a}^\dagger e^{i\nu t} + \hat{a}e^{-i\nu t}\right) + \phi\right)} + \text{ H.c. }\right)\end{aligned} \tag{2.31}$$

By using the rotating wave approximation, we are able to eliminate the high frequency components, which are on the order of $\omega_L + \omega_0$, and get the Hamiltonian that is associated with the interaction picture,

$$\hat{H}_I = -e\mathbf{r}_{eg} \cdot \frac{\mathbf{E}_0}{2}\hat{\sigma}_+ e^{-i(\delta t + \phi)} e^{i\eta\left(\hat{a}^\dagger e^{i\nu t} + \hat{a}e^{-i\nu t}\right)} + H.c. \tag{2.32}$$

where $\delta = \omega_L - \omega_0$ is the detuning. We decided to go with $\Omega = -e\mathbf{r}_{eg} \cdot \mathbf{E}_0 e^{-i\phi}$, which is known as the Rabi frequency, then the $\hat{H}_I$ is

$$\hat{H}_I = \frac{\Omega}{2}\hat{\sigma}_+ e^{-i\delta t} e^{i\eta\left(\hat{a}^\dagger e^{i\nu t} + \hat{a}e^{-i\nu t}\right)} + \text{ H.c.} \tag{2.33}$$

We make the observation that this Hamiltonian is generated from the dipole interaction, nevertheless, for any other sort of interactions, whether quadrupole or Raman interaction, the Hamiltonian of laser and ion is always of the same form. The only thing that is different is the concrete representation of the Rabi frequency, which is denoted by Ω, but we are not too concerned about it since it can be determined by experimentation. As the ytterbium hyperfine qubits are the primary research topic in our laboratory, I will provide an in-depth depiction of the Raman interaction in the next part.

Let us proceed by assuming the following form for the detuning δ of the laser frequency ω_L from the atomic frequency ω_0,

$$\delta = \omega_L - \omega_0 = k\nu,\ k = 0, \pm 1, \pm 2, \ldots \tag{2.34}$$

We apply BCH theorem ① to equation (2.33),

① $e^X e^Y = e^Z$ where $Z = X + Y + \frac{1}{2}[X,Y] + \frac{1}{12}[X,[X,Y]] - \frac{1}{12}[Y,[X,Y]] + \cdots$

$$\hat{H}_I = \frac{\Omega}{2}\hat{\sigma}_+ e^{-\eta^2/2} \sum_{n,m=0}^{\infty} (i\eta)^{n+m} \frac{(a^\dagger)^n}{n!} \frac{a^m}{m!} e^{i\nu t(n-m-k)} + H.c. \tag{2.35}$$

If the laser is tuned at the frequency ω_L such that $k = 0$, the spectral line is called the carrier. For $k > 0$ ($k < 0$), the spectral line is termed the kth blue (red) sideband because the laser is blue (red) detuned from the atomic frequency ω_0.

The spectral line is referred to as the carrier when the laser is adjusted to operate at the frequency ω_L in such a way that $k = 0$. Since the laser is blue (or red) detuned from the atomic frequency ω_0, the spectral line is referred to as the kth blue (or red) sideband when $k > 0$ (or $k < 0$), respectively.

As a result, the Hamiltonian of the kth order, denoted by the symbol $\hat{H}_I^k$, may be written as follows,

for $k > 0$

$$\hat{H}_I^k = \sum_{m=0}^{\infty} \left(\frac{\Omega_{m,m+k}}{2} |e\rangle\langle g| \otimes |m+k\rangle\langle m| + \text{ H.c. } \right), \tag{2.36}$$

for $k < 0$

$$\hat{H}_I^k = \sum_{m=0}^{\infty} \left(\frac{\Omega_{m,m+|k|}}{2} |e\rangle\langle g| \otimes |m\rangle\langle m+|k|| + H.c. \right), \tag{2.37}$$

where for $k > 0$, $\Omega_{m,m+k} = \Omega_{m+k,m} = \Omega e^{-\eta^2/2} (i\eta)^k L_m^k(\eta^2) \sqrt{\frac{m!}{(m+k)!}}$ is the Rabi frequency between the two states, $|g\rangle|m\rangle(|g\rangle|m+k\rangle)$ and $|e\rangle|m+k\rangle(|e\rangle|m\rangle)$, so $\Omega_{m,m+k} = \left|\Omega_{m,m+k}\right| e^{i\frac{k\pi}{2} - i\phi}$.

The $\hat{U}_k = \exp(-i\hat{H}_I^k t)$ notation denotes the temporal evolution operator. In order to discover the rule, we may broaden it and do the calculation $(\hat{H}_I^k)^2$, $(\hat{H}_I^k)^3$.

We are primarily interested in the interactions on the carrier ($k = 0$) and the first red (blue) sideband ($k = -1(+1)$) in terms of quantum coherent manipulations of a single ion. This is because these interactions are the fundamental components for the constructions of a wide class of quantum manipulations, such as sideband cooling and the spin-dependent force.

For $k = 0$

$$\begin{aligned}\hat{U}_c = &\sum_{m=0}^{\infty} \cos\left(\frac{\left|\Omega_{m,m}\right| t}{2}\right)(|g\rangle\langle g| \otimes |m\rangle\langle m| + |e\rangle\langle e| \otimes |m\rangle\langle m|) \\ &- i\sum_{m=0}^{\infty} \sin\left(\frac{\left|\Omega_{m,m}\right| t}{2}\right)\left(|e\rangle\langle g| \otimes |m\rangle\langle m|e^{-i\phi} + \text{ H.c. }\right)\end{aligned} \tag{2.38}$$

For $k = -1\,(+1)$

$$\begin{aligned}\hat{U}_{r(b)} = &\sum_{m=0}^{\infty} \cos\left(\frac{\left|\Omega_{m,m+1}\right| t}{2}\right)(|g(e)\rangle\langle g(e)| \otimes |m+1\rangle\langle m+1| + |e(g)\rangle\langle e(g)| \otimes |m\rangle\langle m|) \\ &- i\sum_{m=0}^{\infty} \sin\left(\frac{\left|\Omega_{m,m+1}\right| t}{2}\right)\left(|e\rangle\langle g| \otimes |m(m+1)\rangle\langle m+1(m)|e^{i\left(\frac{\pi}{2}-\phi\right)} + \text{ H.c. }\right) \\ &+ |g(e)\rangle\langle g(e)| \otimes |0\rangle\langle 0|\end{aligned} \tag{2.39}$$

Even when the average phonon number of the motional state is rather large, the preceding forms may still be applied to the dynamics of the ions even while operating outside of the Lamb-Dicke regime. The majority of the time, especially after ground-state cooling of the ion motion, we only expand the Hamiltonian (2.33) to the first order of the Lamb-Dicke parameter η in the Lamb-Dicke regime. After doing so, the Hamiltonian (2.33) can be approximated to

$$\hat{H}_I = \frac{\Omega}{2}(\hat{\sigma}_+ e^{-i\delta t} + H.c.) + \frac{i\eta\Omega}{2}\left(\hat{\sigma}_+(\hat{a}^\dagger e^{i(\nu-\delta)t} + \hat{a}e^{-i(\nu+\delta)t}) + H.c.\right). \tag{2.40}$$

This is especially true after ground-state cooling of the ion motion. Setting δ close to 0, $-\nu$ and ν accordingly and disregarding the rather rapid rotating terms allows us to quickly get the carrier, the first red sideband, and the first blue sideband from this equation.

2.3.2 Raman coherent control

Consider now how the Raman laser beams would react if they were to contact with a single ion. This laser is called a pump laser and its frequency is ω_p and Rabi frequency Ω_p. The other laser is called a Stokes laser and its frequency is ω_s and Rabi frequency Ω_s. As we can see from Fig. 2.5, there are two laser beams coupling the spin-down state ($|\downarrow\rangle$) and the auxiliary state ($|1\rangle$). The laser-ion Hamiltonian under intraction picture is an extension of the equation that additionally considers the cross coupling terms (i.e. the pump (Stokes) beam also couples $|\uparrow(\downarrow)\rangle$ and $|1\rangle$), as well as the intraction picture.

$$\begin{aligned}\hat{H}_R = &\left(\frac{\Omega_p^{1\uparrow}}{2}\hat{\sigma}_{1\uparrow}e^{-i(\Delta+\omega_0)t} + \frac{\Omega_p^{1\downarrow}}{2}\hat{\sigma}_{1\downarrow}e^{-i\Delta t}\right)e^{i\eta_p(a^\dagger e^{ivt}+ae^{-ivt})} \\ &+\left(\frac{\Omega_s^{1\uparrow}}{2}\hat{\sigma}_{1\uparrow}e^{-i(\Delta-\delta)t} + \frac{\Omega_s^{1\downarrow}}{2}\hat{\sigma}_{1\downarrow}e^{-i(\Delta-\delta-\omega_0)t}\right)e^{i\eta_s(a^\dagger e^{ivt}+ae^{-ivt})} + H.c.,\end{aligned} \tag{2.41}$$

where $\Omega_x^{i,j} = -\frac{e\mathbf{r}_{i,j}\cdot\mathbf{E}_x}{\hbar}e^{-i\phi_x}(i,j = \downarrow,\uparrow,1$ and $x = p,s)$ means the Rabi frequency coupling $|i\rangle$ and $|j\rangle$ via laser x and $\hat{\sigma}_{i,j} = |i\rangle\langle j|$. Δ, δ and ω_0 is explained in the caption of Fig. 2.5.

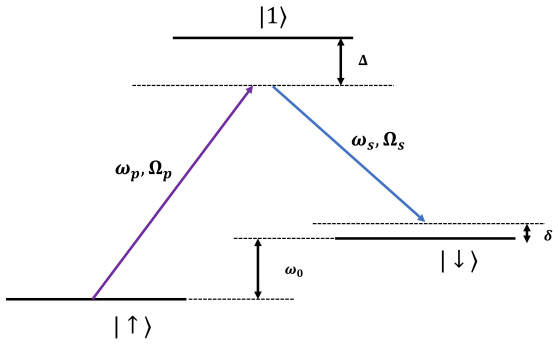

Figure 2.5 Level scheme of Raman transition.

Changing to a new reference frame via $\hat{U} = e^{i\delta t|\uparrow\rangle\langle\uparrow|+i\Delta t|1\rangle\langle 1|}$ allows us to get the Hamiltonian, which is as follows,

$$\begin{aligned}\widetilde{H} = &-\delta|\uparrow\rangle\langle\uparrow| - \Delta|1\rangle\langle 1| + \left[\left(\frac{\Omega_p^{1\downarrow}}{2}\sigma_{1\downarrow} + \frac{\Omega_p^{1\uparrow}}{2}\sigma_{1\uparrow}e^{-i(\omega_0+\delta)t}\right)e^{i\eta_p\left(a^\dagger e^{ivt}+ae^{-ivt}\right)}\right. \\ &\left.+\left(\frac{\Omega_s^{1\uparrow}}{2}\sigma_{1\uparrow} + \frac{\Omega_s^{I\downarrow}}{2}\sigma_{1\downarrow}e^{i(\omega_0+\delta)t}\right)e^{i\eta_s\left(a^\dagger e^{ivt}+ae^{-ivt}\right)} + H.c.\right].\end{aligned} \tag{2.42}$$

For $\delta \ll \omega_0$, and $\Omega_s^{1\downarrow}, \Omega_p^{1\uparrow} \ll \omega_0 + \delta$, it might be possible to omit the cross-coupling phrases. The Hamiltonian equation would therefore be,

$$\begin{aligned}\breve{H} = &-\delta|\uparrow\rangle\langle\uparrow| - \Delta|1\rangle\langle 1| \\ &+\left[\frac{\Omega_p^{1\downarrow}}{2}\hat{\sigma}_{1\downarrow}e^{i\eta_p\left(a^\dagger e^{ivt}+ae^{-ivt}\right)} + \frac{\Omega_s^{1\uparrow}}{2}\hat{\sigma}_{1\uparrow}e^{i\eta_s\left(a^\dagger e^{ivt}+ae^{-ivt}\right)} + \text{H.c.}\right].\end{aligned} \tag{2.43}$$

If we set the internal state as $|\psi(t)\rangle = c_\downarrow(t)|\downarrow\rangle + c_\uparrow(t)|\uparrow\rangle + c_1(t)|1\rangle$, then the evolution equations of $c_\downarrow, c_\uparrow, c_1$ are

$$
\begin{aligned}
i\dot{c}_{\downarrow} &= \frac{\left(\Omega_p^{1\downarrow}\right)^*}{2} e^{-i\eta_p\left(a^\dagger e^{i\nu t}+ae^{-i\nu t}\right)} c_1 \\
i\dot{c}_{\uparrow} &= -\delta c_{\uparrow} + \frac{\left(\Omega_s^{1\uparrow}\right)^*}{2} e^{-i\eta_s\left(a^\dagger e^{i\nu t}+ae^{-i\nu t}\right)} c_1 \\
i\dot{c}_1 &= \frac{\Omega_p^{1\downarrow}}{2} e^{i\eta_p\left(a^\dagger e^{i\nu t}+ae^{-i\nu t}\right)} c_{\downarrow} + \frac{\Omega_s^{1\uparrow}}{2} e^{i\eta_s\left(a^\dagger e^{i\nu t}+ae^{-i\nu t}\right)} c_{\uparrow} - \Delta c_1.
\end{aligned}
\tag{2.44}
$$

If that Δ is far larger than $\Omega_p^{1\downarrow}$ and $\Omega_s^{1\uparrow}$, the population probability of $|1\rangle$ will be very low due to the far detuning. Hence, we will be able to adiabatically remove this irrelevant state by setting $\dot{c}_1$ to zero and obtaining $c_1 = \frac{\Omega_P^{1\downarrow} c_{\downarrow} + \Omega_s^{1\uparrow} c_{\uparrow}}{2\Delta}$. The effective equation for the development of a system with two levels is as follows,

$$
\begin{aligned}
i\dot{c}_{\downarrow} &= \Lambda_{\downarrow} c_{\downarrow} + \frac{\Omega_R^*}{2} e^{-i\eta\left(a^\dagger e^{i\nu t}+ae^{-i\nu t}\right)} c_{\uparrow} \\
i\dot{c}_{\uparrow} &= \frac{\Omega_R}{2} e^{i\eta\left(a^\dagger e^{i\nu t}+ae^{-i\nu t}\right)} c_{\downarrow} + \left(\Lambda_{\uparrow} - \delta\right) c_{\uparrow},
\end{aligned}
\tag{2.45}
$$

$\Lambda_{\downarrow(\uparrow)} = \frac{\left|\Omega_{p(s)}^{1,\downarrow(\uparrow)}\right|^2}{4\Delta}$ is the second-order ac Stark shift of the state, $\eta = \eta_p - \eta_s$ is the Lamb-Dicke parameter of the differential wave vector $\Delta\mathbf{k} = \mathbf{k}_p - \mathbf{k}_s$. The effective Rabi frequency used to couple the two qubit states is denoted by $|\downarrow(\uparrow)\rangle$ and $\Omega_R = \frac{\Omega_p^{1\downarrow} \times (\Omega_s^{1\uparrow})^*}{2\Delta}$. Now, with the help of the aforementioned evolution equations, we can easily get the effective Hamiltonian of the qubit,

$$
\hat{H}_{\text{eff}} = \frac{\Delta_{ss}}{2}\hat{\sigma}_z + \frac{\Lambda_{\uparrow} + \Lambda_{\downarrow}}{2}\hat{I} - \delta\hat{\sigma}_+\hat{\sigma}_- + \left(\frac{\Omega_R}{2} e^{i\eta\left(a^\dagger e^{i\nu t}+ae^{-i\nu t}\right)}\hat{\sigma}_+ + H.c.\right), \tag{2.46}
$$

where $\Delta_{ss} = \Lambda_{\uparrow} - \Lambda_{\downarrow}$ is the differential ac Stark shift of the two qubit levels. By removing an insignificant component from $\hat{I}$ and transferring into the reference frame in terms of $\hat{U}_0 = e^{-i\delta\hat{\sigma}_+\hat{\sigma}_- + i\Delta_{ss}\sigma_z/2}$, we get the effective Hamiltonian that is identical to Eq. (2.33),

$$
\hat{H}_{\text{eff}} = \frac{\Omega_R}{2} e^{-i\mu t} e^{i\eta\left(a^\dagger e^{i\nu t}+ae^{-i\nu t}\right)}\hat{\sigma}_+ + H.c. \tag{2.47}
$$

where $\mu = \delta - \Delta_{ss}$ is a redefinition of the two-photon detuning. On the basis of this Hamiltonian, it is feasible to do all of the manipulations, such as switching between the carrier and the red and blue sidebands.

CHAPTER 3 EXPERIMENTAL SETUP

The rate of background gas collisions with the ion chain is one of the scaling challenges in an ion-trapped system. Such collisions may destroy the qubit's information and result in the loss of the whole chain. Thus, it is essential to construct an extreme high vacuum (XHV) environment to reduce pressure of the background gas in the vacuum system.

3.1 The cryostat

The cryostat is the key equipment of the cryogenic trapped ion system. We need to pay attention to some key technical indicators when choosing the model of the cryostat, designing the internal support structure and the assembly structure of the trap-related components. The most critical technical indicators are cooling capacity and vibration. Low temperature is the advantage of the cryogenic trap over the room-temperature trap. We can achieve low pressure by cryo-pumping to reduce the collision rate of trapped ions with residual background gas, thereby increasing the lifetime of trapped ions. The price of cryo-pumping is additional vibration, however, the vibration can be reduced to a degree that does not affect quantum gate fidelity. In experiments, we often use these two parameters to characterize the cooling capacity. One is the lowest temperature that the system can reach when the cryogenic trap is not temperature stabilized, and the other is the heating power at the sample mount when the temperature of the cryogenic trap is stabilized above the liquid helium temperature zone and the vibration caused by liquid helium is reduced to a certain range. Another key technical indicator of the cryostat is the long-term stability at the sample, including changes in displacement and background electric field. This will affect the calibration period of the ion trap experiment. Calibration that is too frequent indicates a lack of robustness in the experiment system.

There are several different types of cryostats on the market. One of these is the flow cryostat, which has lower cryocooler vibration noise but requires constant replenishment of cold liquid coolant, which is expensive and time-consuming. In contrast, the cryogenic trapped ion system in our lab uses a closed-loop Gifford-McMahon cryostat. This type of cryostat uses closed-cycle helium gas as operation material in cooling cycle and does not require constant refilling of the coolant. It is very convenient to use and cheap to maintain

as it only needs external electric supply. One of the advantages of this closed-loop cryostat is that it has a vibration isolation system (VIS). The vibrating cold finger is mechanically separated from the main vacuum by a helium-filled exchange gas region at a pressure 0.03 bar above atmospheric. The vibration isolation system is the only mechanical coupling between the cold head and the main vacuum apparatus which is mounted on an optical breadboard. In the vibration isolation system region, it is sealed with a helium-confined rubber bellows. The helium gas serves as the thermal link between the cold finger and the sample mount where the ion trap is mounted. Another advantage of this closed-cycle cryostat is that its structure is relatively simple, and we can increase cooling capacity and reduce vibration through optimized design, because it is difficult to optimize each parameter independently in a complex system.

Table 3.1 Refrigeration capacity (typical).

	RDK-408D2	RDK-415D2
First stage	40 Watts @ 43 (50Hz)	35 Watts @ 50K (50Hz)
	50 Watts @ 43 (60Hz)	45 Watts @ 50K (60Hz)
Second stage	1.0 Watt @ 4.2K (50/60Hz)	1.5 Watt @ 4.2K (50/60Hz)

The cryostat is model SHI-4XG-15-UHV, designed and manufactured by Janis Inc. In order to reduce vibration, we provide some design suggestions. The cryostat consists of a cold head, an exchange gas space and a vacuum chamber. The cold head is powered by a helium compressor. The models of cold head and helium compressor are RDK-415D2 and F70-H produced by Sumitomo Corporation of Japan. The cold head features two stages with different refrigeration capacity: the 40 K stage has $\sim$ 35 W, and the 4 K stage has 1.5 W, as shown in Table 3.1. The cold head must be fixed near the vacuum chamber, but there are only three interfaces of the cold head: the power supply, the supply high-pressure helium tube and the return high-pressure helium tube. Therefore, we placed the helium compressor and water cooler in the grey room of the laboratory to further isolate the source of vibration noise. The single continuous running time of the cold head can exceed 10,000 hours, which is enough for us to carry out long-term experiments.

The exchange gas space, as shown in Fig 3.1, is mainly composed of rubber bellow, helium pressure gauge and some helium valves, the top and bottom are respectively connected to the cold head and the vacuum chamber. The role of bellow is to reduce the vibration generated by the cold head and directly transmitted to the vacuum chamber, because rubber is more elastic than stainless steel. I think it is worth trying to replace the

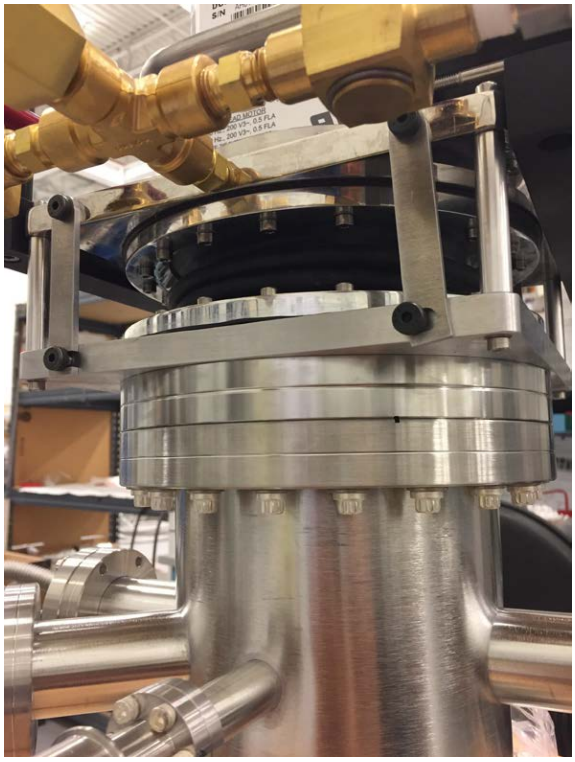

Figure 3.1 Exchange gas space.

rubber bellow with a stainless-steel sheet that has been bent many times, because using a rubber bellow may cause leakage in the long-term operation of the system. Leakage of rubber bellow may come from three aspects. Firstly, the rubber material will deteriorate after a long-time use, our system has a leakage problem after about 2 years of operation, which is manifested as water inside the exchange gas space after the process of cooling down and warming up. Secondly, the rubber bellow is prone to defects during machining, we contacted our supplier to process a new rubber bellow after we found the leakage problem, and found that some of the rubber bellow had defects on the surface during many attempts. Finally, the sealing method of rubber bellow is worse than that of stainless steel, our cryostat uses o-ring to seal rubber bellow. We tried to have the supplier process different rubber bellow to test the leakage, such as testing different materials and thickness of rubber bellow, in some poor cases after a single cooling and reheating process will appear leakage, we finally used silicone rubber bellow and the thickness is twice the original and no leakage has been found so far.

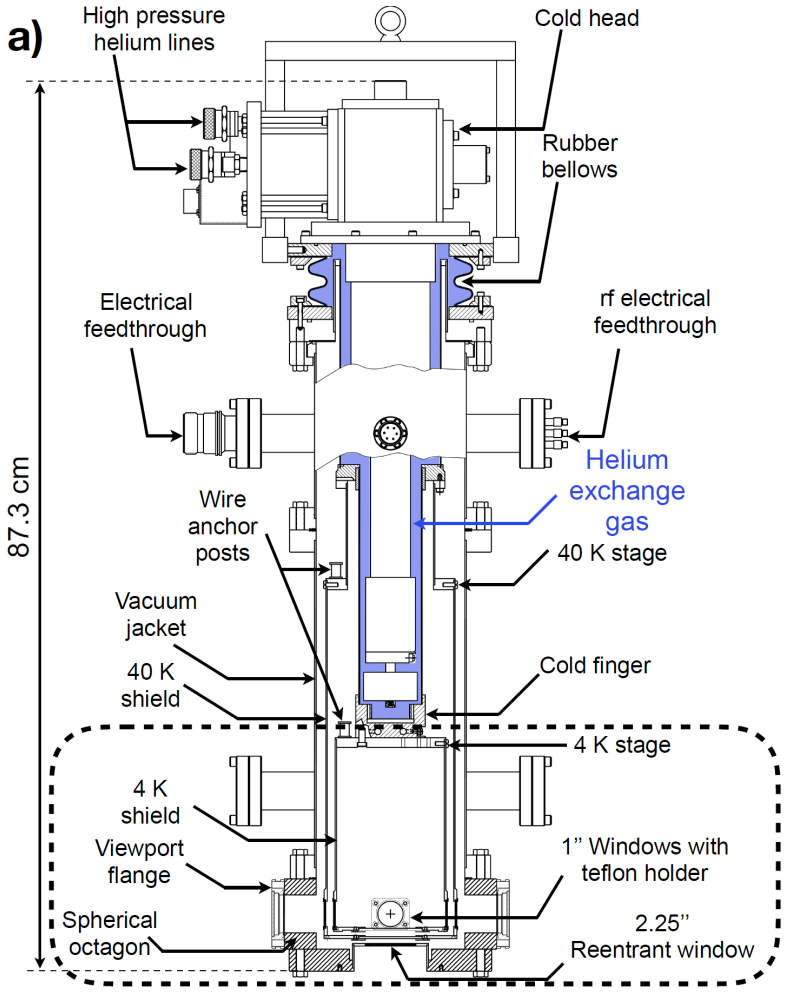

Figure 3.2 The side section view of the Gilford-McMahon cryostat.

3.2 Cryogenic and UHV system

The vacuum chamber resembles a cylinder with a diameter of about 200 mm and a height of about 600 mm. Externally, the upper part of the vacuum chamber has some feedthroughs connecting the electrical equipment to the vacuum equipment, and the lower part is a spherical octagon. The top of the vacuum chamber is in contact with the exchange gas space, and the bottom is the re-entrant window. In our experiments, we used a total of three electrical feedthroughs, one DC feedthrough to drive the voltage signal to the electrodes of the trap, another DC feedthrough to drive the thermometer and heater in the vacuum chamber, and an RF feedthrough to drive the RF signal to the resonator. Below them, there are a total of three Vacuum feedthroughs, one connected to an ion gauge (Agilent UHV-24P) to monitor the vacuum level in the vacuum chamber, one connected to a NEG-Ion pump (SAES NextTorr Z100) to pump out hydrogen, since hydrogen is the least efficiently cryo-pumped gas, and an angle valve to pump out vacuum during

system maintenance. A spherical octagon holds eight 1” diameter windows to provide optical access in the horizontal plane, the windows are made of UVFS and have different wavelength optical coatings according to the optical path design. We replaced one of the windows along the trap axis with an oven feedthrough, and installed both enriched ^{171}Yb oven and enriched ^{174}Yb oven on it, and finally tested them to work. However, assembly errors during installation may cause the Yb flux cannot enter the trap during ion loading, we can increase the translation degrees of freedom when designing the part to solve this problem. According to our experience, because of the large divergence angle of Yb flux, we just need to be able to see the trap and oven through the opposite window. The re-entrant window located at the bottom of the vacuum chamber has a diameter of 2.25”, below which is the imaging system. The maximum numerical aperture allowed for imaging ions along the vertical direction is 0.5. The Re-entrant window is surrounded by a doughnut-shaped aluminum base placed on an optical breadboard, and the base carries the full weight of the vacuum chamber. We tried to fasten between the upper part of the vacuum chamber and the optical breadboard with an aluminum sloped beam, but it did not reduce the vibration of the trap, indicating that the current support structure is solid enough.

Table 3.2 Table of electrical devices connected to the vacuum chamber.

Device	Model
ion gauge	Agilent UHV-24P
NEG-Ion pump	AES NextTorr Z100
DC signal source	Homemade 16-channel AD5791
RF signal source	Rohde & Schwarz SMB-100B

The main components inside the vacuum chamber are the 40 K shield, the 4 K shield and the sample mount. These two shields are used to shield the ion trap from room temperature blackbody radiation, their material is aluminum, but copper may be a better choice because copper material has a higher thermal conductivity. The bottom of the two shields are eight 1” UVFS windows, which correspond to the spherical octagon and have the same optical coating. The glass is fixed in the groove by the Teflon holder in order to keep the windows from being crushed during the cooling procedure, however, because of the elasticity of Teflon, the positioning accuracy of the windows is poor, which may be the main source of optical aberration. The top of the 40 K shield is in contact with the 40 K stage of the cold head through the helium gas in the exchange gas space, which is

usually higher than 40 K, we named it that way just because it is intuitive. The top of the 4 K shield is fixed to the sample mount, which is made of oxygen-free copper with a gold-plated surface to obtain a high thermal conductivity and to prevent oxidation during system maintenance. The sample mount and the 4 K stage of the cold head are separated by a heat exchanger and cryogenic helium gas. The 4 K stage can reach temperatures below 4 K, and the heat exchanger is composed of a series of concentric circular oxygen-free copper sheets, which are designed to increase the cooling capacity at the sample mount. However, if the position between a pair of heat exchangers is shifted during operation and touches each other, it can introduce large vibrations to the sample mount, for example when floating the optical table.

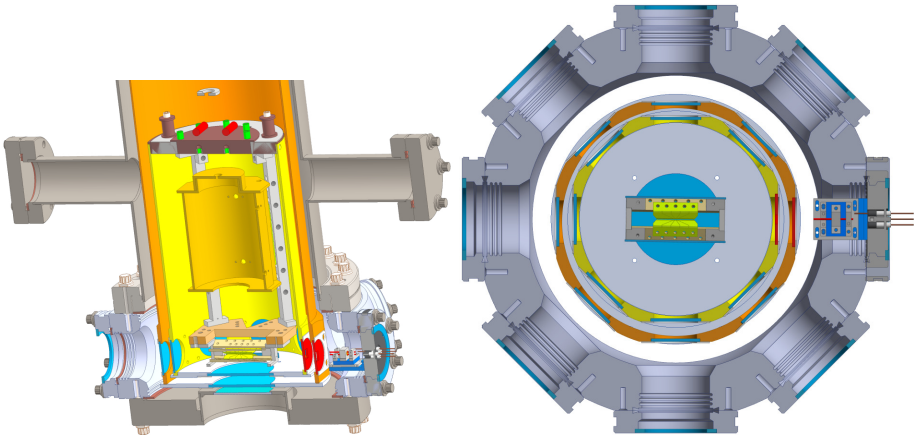

(a) The oblique view of ion trap and vacuum chamber. (b) The top view of ion trap and vacuum chamber.

Figure 3.3 The design and related information of the cryostat.

Although the refrigeration capacity of the 4 K stage in the cold head reaches 1.5 W, the cooling capacity of the sample mount in the vacuum chamber, which is directly available to the user, is much lower. The reduction of the cooling capacity comes from the heat conduction between the 4 K stage and the sample mount and the heat leakage from the environment. In order to improve the heat transfer between the 4 K stage and the sample mount, we can increase the surface area of the heat exchanger, we can also fill the exchange gas space with sufficient helium gas, and it is necessary to use oxygen-free copper to produce thermally conductive parts. In our experiments, we use auto gas charging system to stabilize the helium pressure in the exchange gas space at a fixed positive pressure. It is worth noting that the rubber bellow loses its vibration isolation function under negative pressure, and the life of the rubber bellow is reduced. The auto gas charging system was designed by PHYSIK and is based on the principle of using a

PLC to read the helium pressure gauge and control the opening and closing moments of the helium valves, which will eventually stabilize the helium pressure gauge at 1.03 bar. There are two helium valves to control the helium inlet and outlet, and one safety value to allow excess helium to escape, preventing the bellow from bursting when the auto gas charging system is not working. The temperature stabilize system is a kit we purchased from Janis Inc. and consists of a thermometer, heater and temperature controller. The thermometer (DT-670-CU-HT-1.4H) is located inside the sample mount in the vacuum chamber and has a measurement range of 1.4-500 K, covering the cryostat operating range of approximately 4-300 K. The heater is a 25 Ω resistor very close to the thermometer. The DC lines of the heater and the thermometer are connected to the temperature controller (Model 26 from CryoCon) on the instrument rack via a DC feedthrough on the vacuum chamber. In low temperature operation, the temperature of the sample mount can be stabilized at 6 ± 0.05 K for a long time by setting the appropriate PID parameters, as shown in Fig 3.4. The output power of the heater is about 350 mW, which means that the refrigeration capacity of the sample mount has a margin of 350 mW.

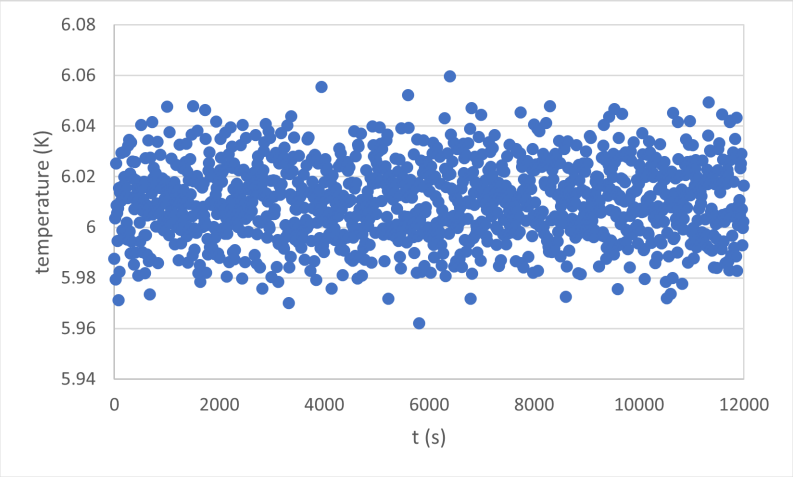

Figure 3.4 The stablized temperature of the sample mount.

The auto gas charging system and the temperature stabilize system are the key systems for the long-term stability of the cryostat. Although the temperature of This cryostat has almost no drift, we can observe that the trap can shift ± 1 μm during the experiment. The operation to avoid the effects of such position shifts by frequent calibration of the system parameters is very complicated, so this instability can be fatal for an experimental system. The long drift of the sample mount comes from the mechanical structure of the cryostat. The auto gas charging system can only stabilize the helium pressure near the rubber bellow, and the 40 K stage and 4 K stage of the cold head are not stabilized.

Therefore, the pressure and temperature in the contact part of the vacuum chamber and the exchange gas space cannot be stabilized for a long time. However, this part is the support point of the sample mount, so the sample mount will be disturbed by these external environmental changes. We can consider fixing the sample mount to the room temperature area of the vacuum chamber, which will not move if the laboratory environment is stable, but this will inevitably increase the heat leakage from the room temperature area. In our experiments, we first pumped the vacuum chamber to 1×10^{-6} mbar at room temperature using the Turbo Pump, then activated the NEG-Ion Pump for about 2 hours, and at the end of the operation the vacuum chamber vacuum level dropped to 1×10^{-8} mbar. The vacuum chamber can reach a vacuum level of 3×10^{-10} mbar with the effect of the cryo-pump.

3.3 Helical resonator and segmented blade trap

The blade trap forms a capacitor of approximately 6 pF. In order to drive this capacitor, i.e. to apply a high voltage signal to it, we need a larger helical resonator to form the LC oscillation circuit and to achieve impedance matching. The two components are therefore closely linked. The helical resonator and the blade trap are both located inside the 4 K shield of the vacuum chamber. The helical resonator is fixed underneath the sample mount and then the blade trap is fixed underneath the helical resonator. This ensures that the helical resonator and the blade trap are very close to each other and that their temperatures are equally stable. At the same time the low temperature allows the resistance in the oscillator circuit to be significantly reduced, which helps to increase the quality factor of the oscillator circuit. The helical resonator and the blade trap are used as a single unit and its input and output are achieved via RF and DC electric feedthrough.

3.3.1 Design of helical resonator

The circuit models for the helical resonator and the blade trap have been well studied. In practice, we have developed a very mature design procedure with a high quality factor, choosing only two parameters b/d and d/D to optimise the performance of the helical resonator with the quality factor as the objective function. We can calculate the loading frequency in the empirical parameter regime using the trap capacitance and the quality factor. Typically, $b/d \approx 1.5$ and $d/D \approx 0.5$ is a good choice, and if the loading frequency meets our requirements we will try to choose the highest quality factor around this param-

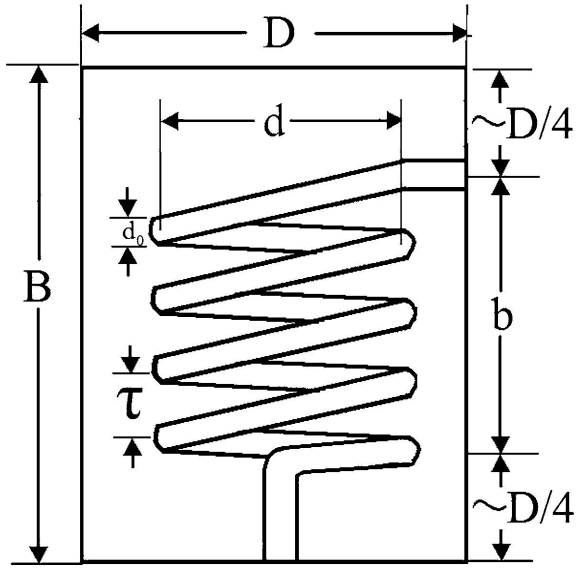

Figure 3.5 The outline design of a helical resonator.

eter range, as shown in Fig 3.5. A two-wire spiral resonator is much more complex than a single-wire spiral resonator because of the coupling between the two coils. However, for the sake of simplicity we are still using the model and we can achieve an accuracy of about ±5 MHz. To ensure that the phase and amplitude of the two coils are the same, we use a parallel capacitor, which is shorted when connected to the RF feedthrough, with a capacitance of approximately 300 nF. The two-wire design is designed to help minimise micro-movements by applying a DC voltage to the RF electrodes, so we need to ensure that the RF signal on the coil is grounded and the DC voltage is not, this is achieved by a 300 nF capacitor connected to the shield. In addition, we added an RC filter before the DC voltage was connected to the coil.

3.3.2 Circuit diagrams of the helical resonator and the blade trap

To facilitate our understanding of the circuit structure of the helical resonator and the blade trap, Fig 3.6(a) shows their equivalent circuit diagrams. In Fig 3.6(b), an external RF signal (RF-In) is fed to a small antenna. The antenna is coupled to a double bifilar helical copper wire, which is short-circuited by a large capacitor (C7, 330nF). The two RF bias signals (RF1 Bias and RF2 Bias) are supplied by the AD5791 and pass through an RC filter consisting of a resistor (R1, R2, 10 $k\Omega$) and a capacitor (C1, C2, 330 nF) to add a DC bias to the respective RF signal. The two capacitively coupled signals (RF1 Pick-off, RF2 Pick-off) can be coupled to a 1% RF resonant signal. The voltage divider circuit uses a small capacitor (C3, C4, 0.2 pF) and a large capacitor (C5, C6, 20 pF) in series. The signal from the two pairs of DC electrodes on the blade trap (DC1, DC2) is

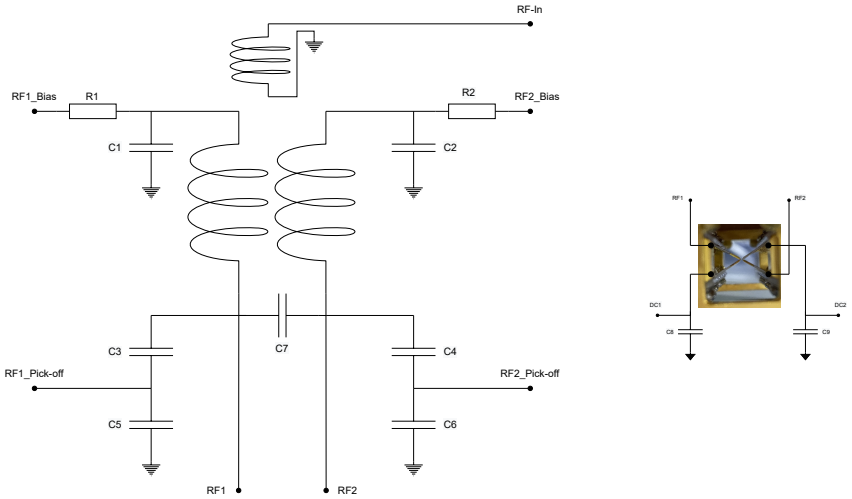

(a) Circuit diagrams of the helical resonator. (b) Circuit diagrams of the blade trap.

Figure 3.6 Circuit diagrams of the helical resonator and the blade trap.

grounded through large capacitors (C8, C9, 820 pF).

Table 3.3 Table of electronic components in the circuit diagrams.

Component	Value	Model	Parameters
Resistor	10 $k\Omega$	RNCF1206TKY10K0	RES 10K OHM 0.01% 1/4W 1206
Capacitor	0.2 pF	VJ1111D0R2VXRAJ	1.5KV
Capacitor	20 pF	800B200JT500XT	CAP CER 500V C0G/NP0 1111
Capacitor	820 pF	C0805C821JCGACTU	CAP CER 500V C0G/NP0 0805
Capacitor	330 nF	C2220C334J1GACTU	100V NP0

3.3.3 Assembly of the helical resonator

The material used for the body of the helical resonator is oxygen-free copper, which is characterised by its very low resistivity and high thermal conductivity. The low resistivity helps to obtain a high quality factor, but the oxygen-free copper is susceptible to oxidation during processing, so the oxide film needs to be removed before assembly. After the helical resonator has been assembled, it needs to be placed in a vacuum enclosure to prevent oxidation.

The main parts of the helical resonator were machined according to the design parameters: the antenna cover, the top cover, the middle part, the bottom cover and the helical coils, which were then cleaned in the ultrasound machine using acetone and ethanol. After

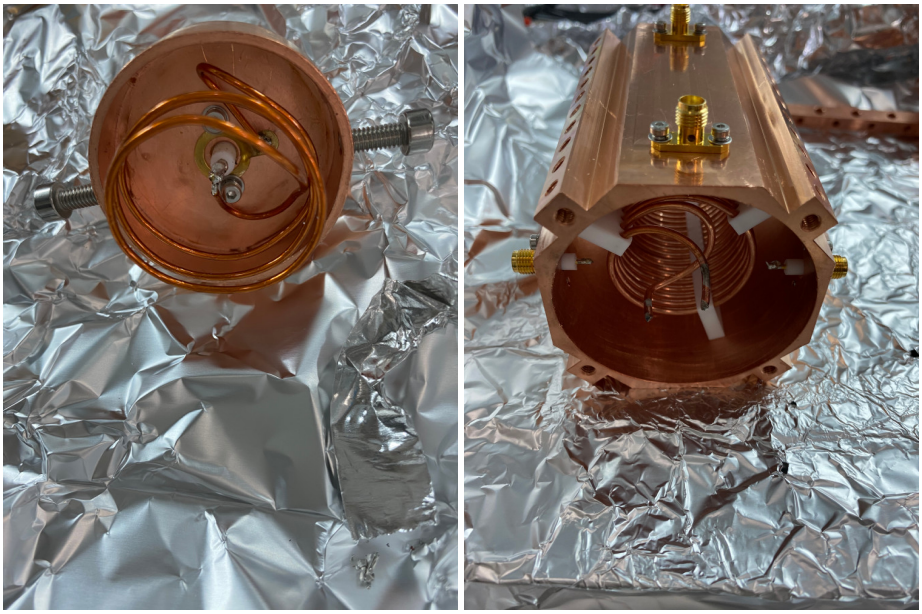

(a) Assembly of the helical resonator antenna.

(b) Assembly of the main section.

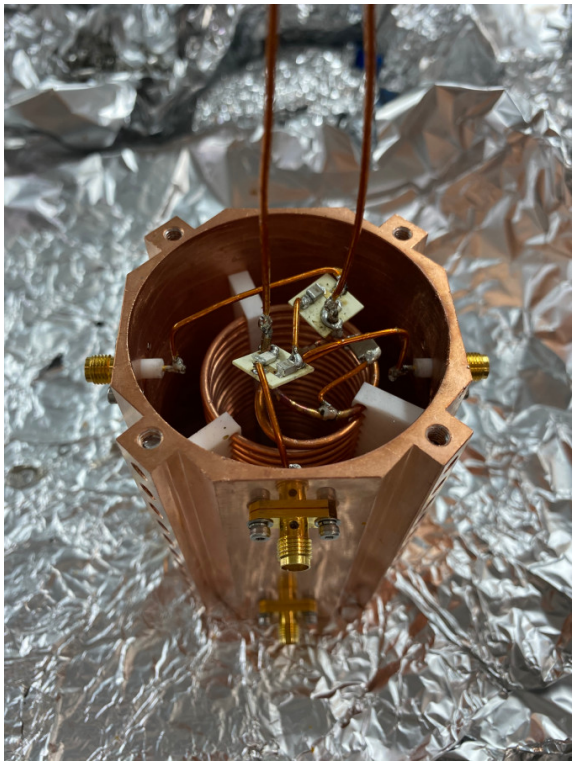

(c) Assembly and soldering of the PCB.

Figure 3.7 Assembly of the helical resonator.

Table 3.4 Assembly procedures of the helical resonator.

Procedure	Content
Preservation	Oxygen-free copper components should not be left in the air for long periods of time and need to be placed in a vacuum enclosure.
Clean	Disassemble the helical resonator and take out the oxygen-free copper components individually into large beakers in preparation for sonication.
	Sonicate them with acetone for 30 minutes and with ethanol for 5 minutes.
	Blow the components dry.
	Soak them in organic acid for 5 minutes, where the surface oxide film can be observed to disappear and turn purplish red.
	Remove residual organic acids from the surface by immerse them in plenty of distilled water.
	Wipe the surface of the oxygen-free copper components with paper, place them in a vacuum hood and evacuate the vacuum enclosure.
Preparation	Cut a number of thick wires into suitable length and trim off the insulation at both ends.
	Prepare the PCB, capacitors, resistors, screw coil retainers, SMA connectors, copper plated components, indium foil, screw sets, spanners.
	Soak the capacitors, resistors and indium foil in acetone for 30 minutes and in ethanol for 5 minutes, sonicate the rest in acetone for 30 minutes and in ethanol for 5 minutes.
Test	Measure the inductance of the helical resonator with an LCR meter. (1.50 μH and 1.41 μH.)
	Measure the scattering parameters of the helical resonator with a vector network analyzer.
	The antenna position and pitch were adjusted to match the impedance when the helical resonator was unloaded. (f = 69.15 MHz, Q = 434.7 U, R = 50.90 dB.)
	After the helical resonator is connected to the Trap, the antenna position and pitch are adjusted so that the impedance matches, and at this point the RC filter is connected. (f = 36.83 MHz, Q = 373.6 U, R = 28.05 dB.)

drying these parts with nitrogen and soaking them in organic acid for 5 minutes, it can be observed that the surface oxide film disappears and turns purplish red. We soak the parts in plenty of distilled water to remove the residual organic acid and then dry the parts with nitrogen. The cleaning of the parts of the main part of the copper tube is now complete. This part needs to be done carefully, as the oxide film on the helical resonator surface affects the quality factor.

We also need to prepare and clean the rest of the parts according to the design parameters to meet the ultra-high vacuum requirements. We then soldered the circuit components together using lead-free solder. The parts are then assembled with stainless steel screws, each requiring a resilient pad to prevent the screws from loosening at low temperatures.

3.3.4 Assembly of blade trap

The advantage of the blade trap is that it is easy to process and assemble, but the disadvantage is that the assembly error is higher compared to the surface trap or the monolithic trap, which causes an asymmetry in the electrostatic potential at the centre of the trap where the ions are located, i.e. a deviation from the linear trap configuration. When designing the blade trap for use in the cryostat, we need to take care that the material has a high thermal conductivity and that the connections between the components are sufficiently tight. In this way we can achieve the lowest temperatures on the blade trap. This helps to obtain a higher vacuum level and to extend the life of the ions.

The blade trap consists of four blade-shaped electrodes, one pair of DC electrodes and one pair of RF electrodes. The blade is processed by laser cutting the ceramic substrate and then plating the surface with a gold layer. The electrodes are machined with a certain amount of error and defects on the surface of the electrode closest to the ion produce a high level of electrical noise, which can be reduced by improving the process. We have machined a sapphire adapter plate and mounted the blade on the sapphire adapter plate and then mounted the sapphire adapter plate on an oxygen-free copper holder. We designed this adapter to avoid a short circuit between the blade and the ground (the blade holder). In order to increase the thermal conductivity, we need to cover these contact surfaces with indium foil. For the fixing of the components we used stainless steel screws and used resilient pads on each screw. This is to prevent the screws from loosening during the cooling down process, and to prevent the blade from being crushed by excessive torque when tightening the screws. Once installed we had to fine-tune the position of the sapphire adapter under the microscope to keep the assembly error small enough. This operation

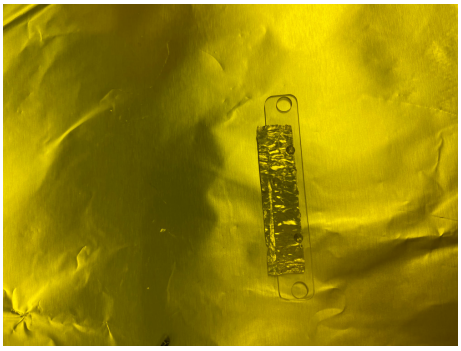

(a) Assembly of the sapphire and indium film.

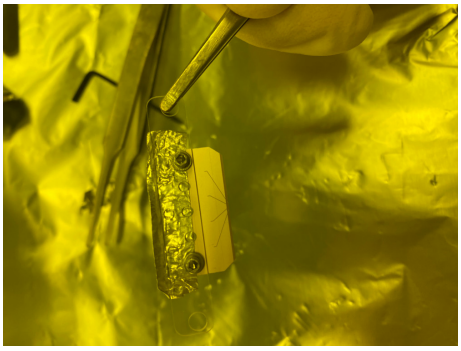

(b) Assembly of the blade.

(c) Assembly of the PCB and the gold ribbon.

Figure 3.8 Assembly of the blade trap.

Table 3.5 Assembly procedures of the blade trap.

Procedure	Content
Checking	Soak the blades in acetone bath for 30 minutes, soak the blades in ethanol bath for 5 minutes, as the blades are very important and fragile.
	Process the DC 820pF capacitors, soak them in acetone bath for 5 minutes, soak them in ethanol bath for 1 minute.
	Lean the blades against the beaker, otherwise it is not easy to be taken out when it sinks.
	The position of the DC capacitor is chosen to allow for clearance for the screws, as well as for the gold ribbon.
	The blades can be soaked in ethanol bath when not in use.
Spot welding	Process the gold ribbon by sonicating it with acetone for 30 minutes and with ethanol for 5 minutes.
	Cover the welding machine with aluminium foil before placing the blades to prevent them from scratching.
Preparation	Prepare hlders, PCBs, sapphire chips, indium foil, M2 and M1.5 screw sets, spanners.
	Make indium foil soaked in acetone bath for 30 minutes and in ethanol bath for 5 minutes, sonicate the rest with acetone for 30 minutes and with ethanol for 5 minutes.
Assembly	Apply indium foil to the sapphire piece, with the front of the indium foil flush with the top of the round hole to prevent short-circuiting the blade.
	Hold the blade parallel to the sapphire piece, remove the excess indium foil and fold the top of the gold ribbon
	Attach indium foil to the holder, then fix the sapphire piece to it, fix the PCB board to the side of the holder and pass the gold ribbon through the air, leaving a certain length of gold ribbon to prevent it from melting when soldering, donnot block the light path.

makes use of the fact that the diameter of the through-hole is slightly larger than the diameter of the screw. Since the assembly is done by hand, this part of the assembly error is unavoidable.

The connection of the blade electrodes is mainly done by means of gold ribbon (AMETEK) and Kapton insulated wire (Accu-Glass Products). When selecting materials we need to be aware of ultra-high vacuum and cryogenic compatibility. Some of the circuit connections are made prior to assembly and the rest is done afterwards. Before assembling the blade, a 820 pF capacitor is fixed with silver epoxy between each DC electrode and ground on the two DC blades. The purpose of this capacitor is to create a low impedance between the DC electrodes and ground, reducing the voltage splitting of the RF signal on the DC electrodes. The gold ribbon is connected to the electrodes with the spot welder at one end and to the pads of the PCB with solder at the other. We will later connect the pads to the corresponding connections with Kapton insulated wire, where the DC electrode wires are connected to the corresponding wires from the DC feedthrough through the heat sink twice, and the two RF electrode wires are connected to the two wires at the output of the helical resonator.

3.4 Yb oven

In order to generate the atomic beams of Yb, we built two separate ovens from two stainless steel tubes, but integrated into a single feedthrough and both able to be used to load ions. The ^{171}Yb oven has an abundance of 90% and The ^{174}Yb oven has an abundance of 98%. As the Yb source is in block form, we need to cut it into small pieces and insert it into the stainless steel tube.

(a) Put all the components together. (b) Connect to feedthrough.

Figure 3.9 Assembly of the Yb oven.

In order to achieve UHV compatibility we chose to use copper, stainless steel and

Macor when machining the parts of the oven. Before assembly and testing, we cleaned all the parts inside the ultrasound machine using acetone and ethanol as solvents. All the parts were assembled according to the drawings and the copper wires on the feedthrough were attached to the stainless steel base, which was all screwed in place. We then used a spot welder and welded the stainless steel tube to the stainless steel wire, and the stainless steel wire to the stainless steel base, respectively. As the stainless steel tube has the smallest cross-sectional area, the highest resistance in the whole circuit is at the stainless steel tube, about 0.5 Ω, so the temperature is highest here too. I would recommend having some extra spare parts and testing the parameters of the spot welder in advance, as the stainless steel tube can easily break under unsuitable parameters. Finally the two Yb sources are filled into the corresponding stainless steel tubes.

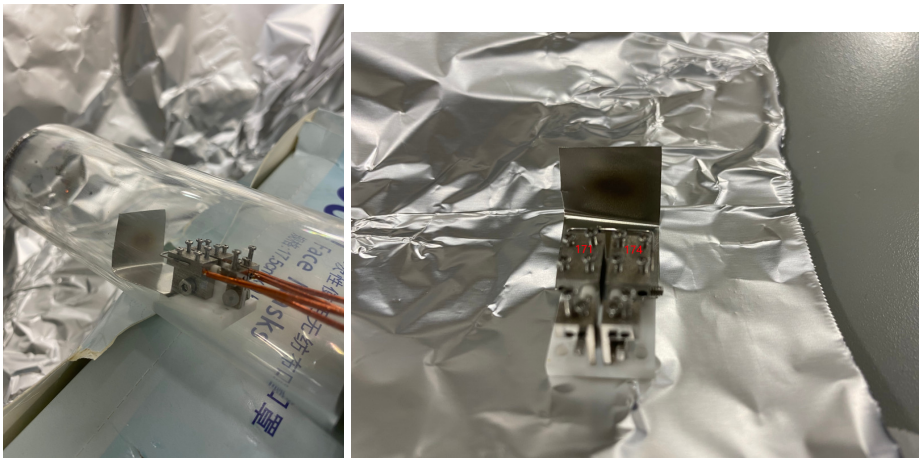

(a) Testing in a vacuum. (b) Observation in the atmosphere.

Figure 3.10 Testing of the Yb oven.

Each oven is mounted in such a way that the outgoing atomic beam is directed towards the trapping area. The oven feedthrough replaces an 1 inch window in the axial direction of the trap. the glass in the corresponding position of the 40 K shield and 4 K shield is also replaced with a round aluminium plate, the centre of which is a square hole with a 5mm side to pass through the Yb flux. As the cryostat has assembly errors, I would recommend preparing round aluminium plates with different opening positions in advance. Ultimately we need to be able to see the trap through the opposite window, with the square hole and the oven in the same line.

In the process of loading ions, when this stainless steel tube is heated resistively by an electric current, a spray of atomic Yb is produced. The temperature reached depends on the current and the time of operation. If either of these two factors is too high or too long, this can lead to rapid evaporation of the Yb and thus the formation of a spray dense

Table 3.6 Parameter variation during Testing the Yb oven.

Oven	Initial vacuum	Ending vacuum	Threshold current
^{171}Yb (Left)	4.0×10^{-6} mbar	8.6×10^{-6} mbar	4.2 A
^{174}Yb (Right)	2.3×10^{-6} mbar	6.5×10^{-6} mbar	3.9 A

enough to cover its surface (e.g. ion trap electrodes or vacuum windows). To prevent this, each oven is tested in advance. A stainless steel sheet is placed in front of the oven and then the oven is placed in a transparent vacuum chamber and the vacuum is reduced to approximately 4×10^{-6} mbar using a turbo-molecular pump, so that a test system can be set up. We tested each oven in turn, starting at 0 A and increasing the current by 0.1 A every 10 seconds, observing the change in vacuum level and the colour of the stainless steel sheet. We can observe both the darkening of the stainless steel sheet and the rapid rise in pressure, at which point the current value is the threshold current for the corresponding oven. ^{171}Yb oven has a threshold current of 4.2 A and ^{174}Yb oven has a threshold current of 3.9A, but the current values we use in practice will be lower than this threshold, the exact values need to be measured in the corresponding experiments. The exact values need to be measured in corresponding experiments, such as observing the fluorescence of Yb atoms and loading Yb ion.

3.5 Optical and imaging system

Whether trapping ions or manipulating them, we need lasers. In our laboratory, tunable diode lasers (Toptica DL pro HP) are used widely, mainly because these products are very well mature. For ion trap systems, a stable light source is very important. Experimentally, we need these lasers to be switched on and off quickly, typically in a few hundred nanoseconds. It is also necessary that these lasers can be stabilised over long periods of time and that these laser controllers have stable software systems. Laser stabilisation covers mode, frequency, power and polarisation. Typical laser stabilisation lasts from a few hours to a day, including laser frequency locking. This is sufficient for our trapped ion experiments, but longer stabilisation times are preferable. In the experiments, these stable lasers are used for: ion loading, Doppler cooling, optical pumping, state detection, repumping and sympathetic cooling. In addition to the laser light path into the cavity, I also built an imaging system to collect the fluorescence emitted by the ions, enabling real-time observation and state detection of the ions.

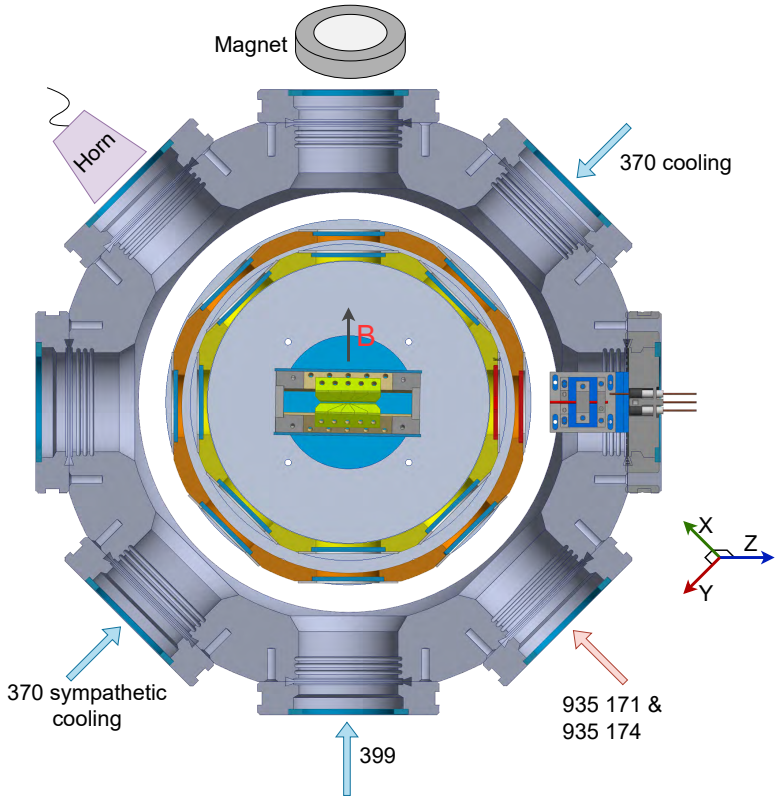

Figure 3.11 Optical layout of the ion trap and the vacuum chamber.

3.5.1 Laser sources and power allocation

The light sources in the laboratory are placed on several separate optical tables. Since the principles of the optical path setup are similar, we can present the light sources and power allocation in a common way, as shown in Fig 3.12. The cryogenic trap platform requires a 370 nm laser (L1), a 399 nm laser (L2) and two 935 nm lasers (L3, L4). The two 935 nm lasers are shared with other ion trap platforms in the lab, one for trapping $^{171}Yb^{+}$ ions and the other for trapping $^{174}Yb^{+}$ ions. The 399 nm laser is used for loading ions. Depending on the type of ion to be loaded, $^{171}Yb^{+}$ or $^{174}Yb^{+}$, we can change the wavelength of the 399 nm laser. This 399 nm laser is also shared with other trapped ion platforms in the lab and only one 399 nm laser is needed. Since loading ions is not very frequent and most of the time we need to load $^{171}Yb^{+}$ ions, and modifying the wavelength of the 399 nm laser will not affect the stable trapping of the loaded ions.

The output power of a semiconductor laser is approximately 10 mW, depending on the wavelength and model, the laser output power may vary a little. The output power of the 370 nm laser (L1) is 13 mW, other lasers have similar output power.

As the nominal light output from the laser is linearly polarised, a power attenuation unit was formed using a half-wave plate(HWP) and polarization beam splitter(PBS)to

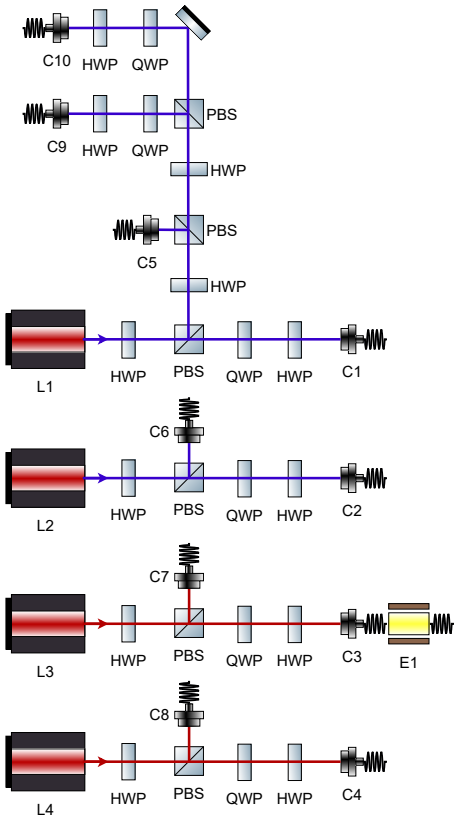

Figure 3.12 Optical path of laser power allocation.

split the laser output into two parts, which are separately coupled into the fibre. Each fibre will act as the light source for the next stage of the optical path, thus making the optical path a modular one. Each laser has one optical fibre connected to the wavemeter (C5, C6, C7, C8). Because polarisation stabilisation is not required, a single-mode fibre is used, with a typical power of approximately 50 μW. The other fibres are the light sources for the rear optical paths (C1, C2, C3, C4) and require high power, typically 5 mW. At the same time their polarisation needs to be stable over time and we use single-mode polarization-maintaining fibres. In order to adjust the polarisation direction to match that of the single-mode polarisation-maintaining fibre, we use a polarisation adjustment unit consisting of a HWP and quarter-wave plate(QWP). We need to maximize the efficiency of the fiber coupling, which requires a good laser output mode and good mode matching, which can be done with a lens pair, I don't show this in the diagram.

The 370 nm laser also has two splits: one (C9) is connected to the optical cavity for narrow linewidth frequency locking of the laser, and the other (C10) is set aside. $^{171}Yb^{+}$ repumping beam requires 3.0695 GHz sidebands, so the 935 nm laser (L3) has a fibre EOM (E1) in the rear optical path.

Table 3.7 Wavelengths of lasers in the laboratory corresponding to loading different isotopes.

Isotope	370 Laser (nm)	399 Laser (nm)	935 Laser (nm)
$^{171}Yb^{+}$	369.526334	398.911150	935.188
$^{174}Yb^{+}$	369.525228	398.911570	935.180

3.5.2 Laser frequency stabilization

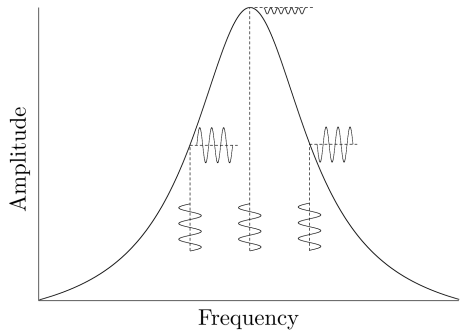

Figure 3.13 Illustration of simple frequency modulation for optical cavity.

The target linewidth of the laser frequency locking determines the laser frequency locking scheme. In my experiments there is no need for ultra-narrow linewidth laser locking, so the laser locking scheme is relatively simple and I have mainly optimised the automatic control of the frequency locking process. The measurement and locking of the laser frequency can be achieved with a wavelength meter, which has a relatively low bandwidth of about 10 Hz because the sum of the measurement time of the multi-channel wavelength meter and the computer readout time is about 100 ms, as shown in Fig 3.14(a). The standard deviation of the output frequency of the laser locked with this scheme is about 1 MHz, which meets my needs with a 399 nm laser and two 935 nm lasers, or if only to trap a small amount of ions then also my requirements for a 370 nm laser. The outgoing light from the laser is transmitted by optical fibres (C5, C6, C7, C8) to the input of the wavemeter, which is programmed to read the frequency on our PC and then programmed to adjust the voltage signal from the laser controller, thus creating a closed loop that locks the laser frequency. The wavemeter's measurements are affected by the environment, mainly air pressure and temperature. Therefore this frequency locking scheme will cause the locked laser frequency to be inaccurate due to inaccurate measurements, but this error is slow and periodic over time. So for 399 nm laser and 935 nm lasers we don't take this into account. I only calibrate the 370 nm laser once in 1 hour or longer, by measuring the resonant frequency of the Yb^{+} ion and feeding it back to the wavemeter's lock point. It would be possible to automatically calibrate the wavemeter for measurement errors if the

wavemeter had a locked reference light all the way through, such as a 780 nm laser, but we have not done this because it is not necessary. The implementation of an automatic frequency lock is necessary as it will simplify the steps of daily operation. By laboratory standards these lasers need to be switched off when they are not in use, for example every night. I will adjust the operating parameters of the laser so that the laser mode can be stabilised back to a specific frequency range for approximately 10 minutes after each switch-on operation, which requires us to find a stable operating parameter for the laser. We then only need to program to communicate with the laser and the wavemeter to achieve automatic laser control and frequency locking.

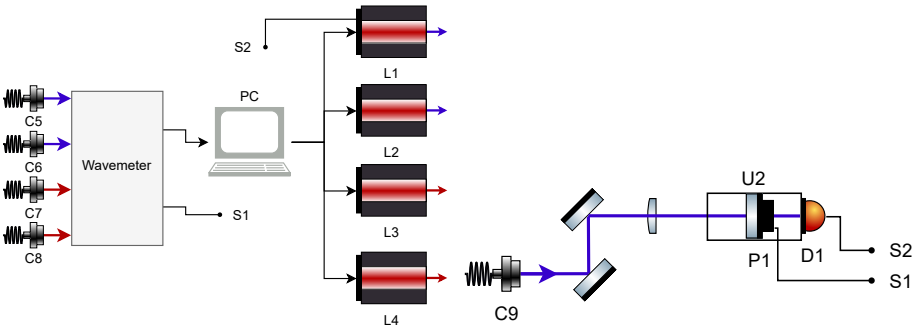

(a) Optical path of the wavelength meter. (b) Optical path of the optical cavity.

Figure 3.14 Optical layout of laser frequency stabilization system.

Figure 3.15 Demodulated signal of the optical cavity photo diode.

The results of targeting the 370 nm laser with a wavemeter are not good enough because the feedback speed is too slow. We can increase the feedback speed with the assistance of an optical cavity, as shown in Fig 3.14(b), which reduces the standard deviation of the output frequency of the 370 nm laser to 300 kHz. I built this optical path on a breadboard in which an optical cavity (U2; SA200-3B, Thorlabs) was placed. The

outgoing light from the 370 nm laser (C9) is incident to the optical cavity. mode matching of the optical cavity is achieved by a pair of reflectors and lenses. Locking the 370 nm laser to the optical cavity is achieved by feeding the output signal of the photodiode (D1) back to the voltage signal of the 370 nm laser controller. In order to have the lock point at the point of maximum transmission light intensity of the optical cavity, I added a modulation signal to the current signal of the 370 nm laser and demodulated the signal from the photodiode (D1). This solution uses a simple optical cavity to increase the bandwidth of the laser locking. This scheme uses a simple optical cavity to increase the bandwidth of the laser locking. However, because environmental factors can cause the cavity length of the optical cavity to change, the locked frequency will change rapidly as the cavity length changes. I connected the voltage signal (S1) from the wavemeter output to the piezoelectric ceramic (P1) of the optical cavity, thus achieving a locking of the optical cavity length to the wavemeter.

3.5.3 Laser modulation

Making the laser modulation a separate module allows for modularisation of the optical path, which facilitates maintenance and testing, and also reduces the size of the optical path into the cavity, which in turn reduces the area of the breadboard where the cryogenic trap vacuum chamber is located. Optical layout of laser frequency stabilization system is shown in Fig 3.16. The main source of laser leakage during laser modulation is the higher order modes of the laser and stray light from the crystal during modulation. Adding a stage of fibre coupling can act as a spatial filter and help reduce leakage.

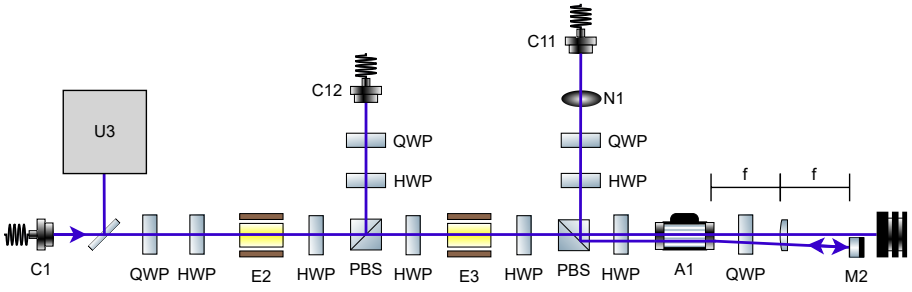

Figure 3.16 Optical layout of laser modulation system.

Experimentally, I need to add sidebands to the 370 nm laser, the 14.7 GHz sideband (E2) for Doppler cooling and the 2.105 GHz sideband (E3) for optical pumping. the electro-optic modulator (EOM) can implement these features. The frequency and modulation depth of the sidebands can be controlled by controlling the frequency and amplitude of the EOM input microwave signal. In addition, I need to control the frequency shift

and power of the 370 nm laser. This is because the difference in frequency required for Doppler cooling and state detection is approximately 12 MHz, and the frequency variation measured during calibration of the system can be compensated for by adjusting the frequency shift of the 370 nm laser. The acousto-optic modulator (AOM) provides these features. By controlling the frequency and amplitude of the microwave signal input to the AOM (A1) the frequency of the laser shift and the laser power can be controlled. However, the AOM modulation efficiency is affected by the microwave signal, as shown in Fig 3.17,and we need to compensate for this using software control during experimental operation.

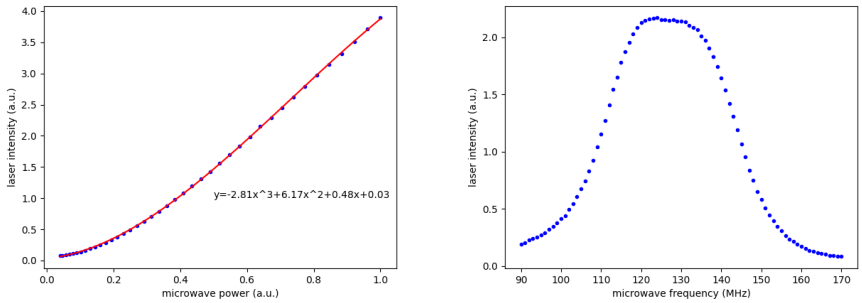

(a) Laser intensity versus microwave power. (b) Laser intensity versus microwave frequency.

Figure 3.17 AOM modulation efficiency influenced by microwave signal.

The light source from the 370 nm laser is fed to the laser modulation module via a single-mode polarization-maintaining fibre (C1), which is reflected by a beam sampling mirror and enters the laser monitoring module (U3). A number of signal acquisition modules are integrated into the laser monitoring module to help me monitor the quality of the light source over time, including measurements of power , polarisation, laser mode and others. The main light source is modulated by two cascaded EOMs, the modulation depth of which can be maximised by adjusting the HWP. Part of the laser is coupled into the fibre (C12), which is then used for sympathetic cooling. To achieve the frequency shift, I built a double-pass configuration based on a 4f optical system, where the PBS serves to separate the incident light from the returned light by 90°, adjusting the HWP at the front to maximise the efficiency of the incident light and the HWP at the back to maximise the efficiency of the diffraction from the AOM. When the laser passes through the AOM, 0 order light is discarded and +1 order light is returned to the AOM by a 4f optical system consisting of a lens and a D-shaped pickoff mirror. The +1 order beam from the reflected beam passes through the QWP twice and is then reflected by the PBS into the fibre (C11),

this light is then used for global cooling, pumping and detection. There is a mechanical shutter (N1) in front of the fibre, which serves to completely shut off the light and reduce leakage.

3.5.4 Optical layout of the cryostat breadboard

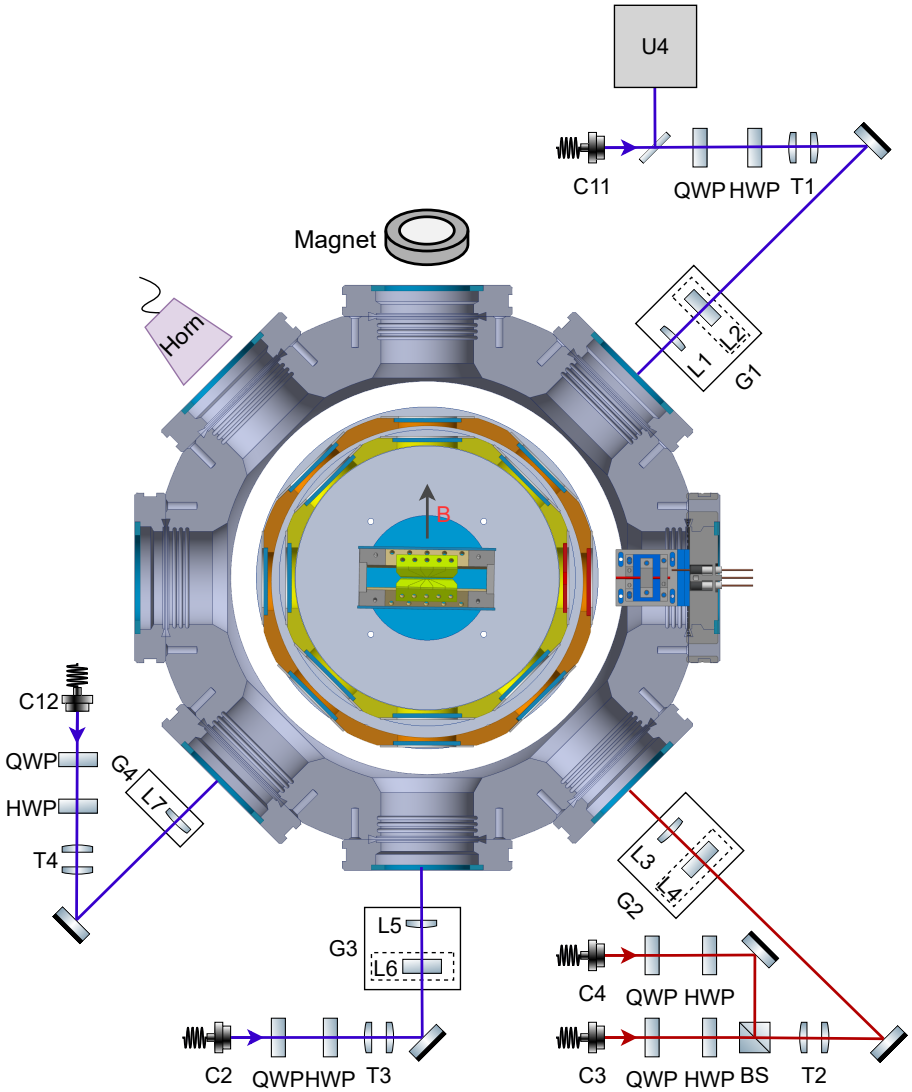

Figure 3.18 Optical layout of the cryostat breadboard.

Due to the large base area of the cryostat, the area left for the optical path on the breadboard is relatively small. the main function of the optical path built on the breadboard of the cryostat is to shape the beam into a specific shape and then inject it into the cavity. There are four windows on the Cryostat that are used to inject the laser. The laser light exiting the fibre collimator (C2, C3, C4, C11, C12) is first polarised by the QWP and HWP and then expanded by the lens pairs (T1, T2, T3, T4) to a suitable spot size, typically with a Gaussian diameter of approximately 10 mm. It is then incident on a long-

focus lens (L1, L3, L5, L7) into the cavity and forms a small spot in the centre of the trap, typically with a Gaussian diameter of about 20 μm. The long-focus lenses are mounted on a 3-axis linear stage (G1, G2, G3, G4; M-461-XYZ-M, Newport) with a Picomotor actuator (8301NF, Newport) in each axis of the stage to achieve high precision control of the beam position.

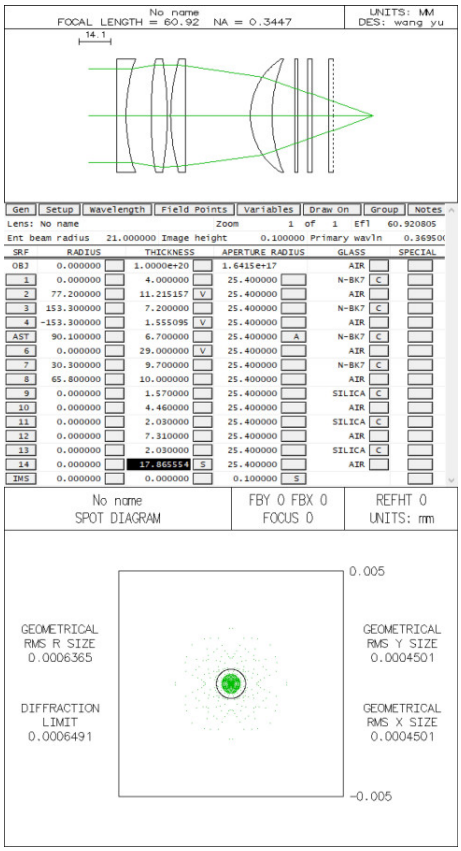

Figure 3.19 Design of the objective.

Reducing the spot diameter at the trap is necessary to increase the power density, reduce stray light and improve the signal to noise ratio. It also helps me to monitor the displacement of the spot relative to the ions over time, which helps me to find unstable components or modules in the system at the beginning of the construction of the system. But when the length of the ion chain in the trap increases, I need some light spots to expand in the horizontal direction to about 500 μm in diameter. It is advantageous to be able to easily adjust the spot diameter in the horizontal direction. I added cylindrical lenses (L2, L4, L6) to the optical path where I needed to adjust the horizontal diameter, and by artificially introducing astigmatism, I was able to shift the horizontal focal position along the optical axis. A long-focused cylindrical lens with a focal length of approximately 1000 mm is generally used, mounted on a rotatable lens mount so that the tilt angle of the

elliptical spot can be adjusted and the cylindrical lens can be removed when the elliptical spot is not required.

The stability of the 370 nm laser (C11) is so important to the experiment that a laser monitoring module (U4) has been installed at the outgoing point of the fiber. This light is global light and is required for ion loading, Doppler cooling, optical pumping, and state detection. In order to trap both $^{171}Yb^{+}$ and $^{174}Yb^{+}$, two 935 nm lasers (C3 and C4) were combined into the cavity and their function was rupumping. Combining these two 935 nm lasers at the front stage would have been a better option, but this was not done due to space planning in the laboratory. The 399 nm laser (C2) is used for ion loading and the 370 nm laser (C12) is used for sympathetic cooling.

A permanent magnet is placed in front of one window to generate a magnetic field at the centre of the trap, approximately 5 Gauss, perpendicular to the direction of the ion chain. A horn is placed in front of one of the windows to apply microwaves.

3.5.5 Imaging system

The objective is specifically designed for cryogenic trap system to collect fluorescence from the ions. The thickness of the glass inside the chamber is 5.63 mm. The numerical aperture of the fluorescence collection objective has to be as large as possible and the currently used objective has a numerical aperture of approximately 0.35. The design of the objective is shown in Fig 3.19

We use the PMT (Hamamatsu H11890) for State Detection of one single ion and the EMCCD (Andor iXon Ultra 888) for State Detection of multiple ions, where the average SPAM error is 3%.

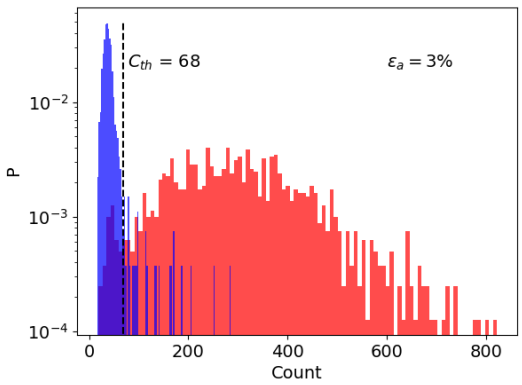

Figure 3.20 Detection error analysis.

3.6 Coherent microwaves

Table 3.8 Measurement of microwave frequency and rabi rate.

Energy level	microwave frequency	π-time
$\|1,0\rangle$	200.0344 MHz	122.3
$\|1,-1\rangle$	188.0974 MHz	78.3
$\|1,1\rangle$	211.9524 MHz	78.2

The system is outfitted with a microwave horn in order to coherently drive global spin rotations. The $|\downarrow\rangle$ and $|\uparrow\rangle$ states are directly coupled by a magnetic dipole moment, so the microwaves can directly drive rotations. Microwave signals are generated by mixing high frequency signals (Rohde & Schwarz SMB-100A, 11 dBm @ 12.4428 GHz) with low frequency signals (Analog Devices AD9910, around 200 MHz). The signals then passes through a high frequency amplifier and is output to a microwave speaker. Measurement of microwave frequency and rabi rate for different energy levels is shown in Table 3.8. Here the microwave frequency is added to 12.4428 Ghz to get the absolute frequency of the corresponding energy level.

CHAPTER 4 CRYOGENIC EXPERIMENTAL TECHNIQUES

4.1 Cool-down and warm-up procedures

The cryogenic trapped-ion system is a relatively complex experimental system, and we need the system to be stable over a long period of time so that the reproducibility of the measurement results is high. Although the cryostat's core component, the cold head, can run continuously for more than 10000 hours, the maximum time this cryostat can run continuously is limited by the stability of the power supply, the stability of the laboratory temperature and humidity, and whether the exchange gas space is leaking, as shown in Fig 4.1. It took us about three years to get the system into a stable long-term state, after which we conducted a series of physical experiments on the experimental platform. However, during the three-year commissioning process, we inevitably need to conduct the cycle of cool-down, malfunction, warm-up, and upgrade, during which the standardized operation helps to make the physical parameters of the system more repeatable, so we have developed a standardized operation procedure for this system.

4.1.1 Maintenance of the exchange gas space

Figure 4.1 Observation of leakage in the exchange gas space.

If the cold head does not need to be removed for servicing, the exchange gas space does not require frequent maintenance and is always in an independent and stable state, whether it is being cooled down or warmed up.

The exchange gas space uses helium gas with a purity of 99.999%. When we expose the exchange gas space to atmosphere or when it is first used, the internal gas needs to be purified. According to the cryostat manufacturer's recommendations, a purification is also required after several months of continuous running, but this is not normally done when the system is stable for a long period of time. How often the exchange gas space needs to be purified depends on the rate of impurity gases (nitrogen, oxygen, water vapour etc.) leaking in from the atmosphere.

When we need to purify the helium gas in the exchange gas space, the exchange gas space is first evacuated continuously for 0.5 hours with a dry scroll pump (Agilent IDP-7), then the valve connected to the dry scroll pump is closed and the valve connected to the helium gas is opened. The auto gas charging system will then raise the pressure to 1.03 bar and finally we close the valve to the helium gas. In general, the above operation is repeated three times to purify the helium gas in the exchange gas space.

When we need to cool down or warm up the system, and also when the system is running at low temperatures for a long time, we simply open the valve to the helium gas and keep the auto gas charging system running steadily.

4.1.2 Cool-down

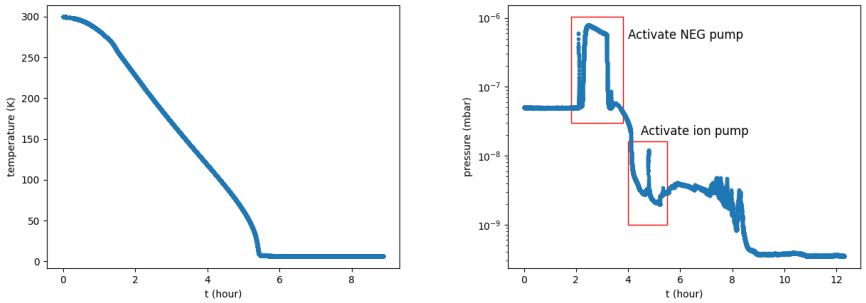

(a) Temperature vs. time. (b) Pressure vs. time.

Figure 4.2 Cryostat temperature and pressure over time during a cool-down.

In the cool-down procedure, the physical parameters of the vacuum chamber are mainly adjusted and observed. The vacuum chamber is first connected to a turbo-molecular pump (TPS-compact Turbo Pumping System) via the angle valve and after approximately 48 hours of continuous operation the vacuum chamber reaches a vacuum

level close to UHV. The ion gauge is switched on and reaches an indication of 5×10^{-8} mbar, at which point we do not need to degas the ion gauge as the room temperature zone of the vacuum chamber does not eventually fall below 1×10^{-10} mbar. Now we need to perform a time limited activation of the NEG Pump for 1 hour, then we perform several degas of the Ion Pump and keep the Ion Pump on. Now that the activation of the NEG-Ion Pump is complete, we close the angle valve and wait about 1 hour for the ion gauge to gradually decrease to 3×10^{-9} mbar, when the vacuum chamber reaches the UHV vacuum level. We turn on the cold head and the temperature stabilize system, which will finish cooling down within 5 hours, but the system will not reach final stabilization for more than 24 hours. The temperature of the 4 K stage is finally stabilised at 6 K and the ion gauge is stabilised at 3×10^{-10} mbar.

4.1.3 Warm-up

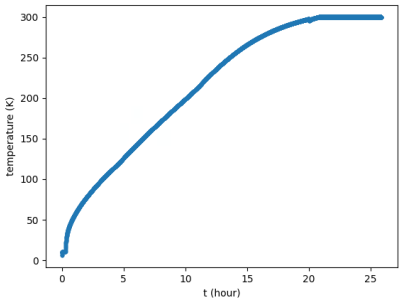

Figure 4.3 Cryostat temperature over time during a warm-up.

The warm-up procedure is much easier than the cool-down procedure because we do not need to obtain UHV during this process. we turn off the cryogenic and vacuum related instruments: the NEG-Ion pump, the ion gauge, the cold head. We can use the heater in the temperature stabilize system to heat the cryostat to speed up the warming process to room temperature, which takes about 24 hours or more. The system can also be allowed to warm up naturally to room temperature, which takes about 48 hours or more. Next, if necessary, we can move the cryostat into the service area for servicing. Before moving it out, we need to record the readings of all optical and electrical instruments. As the imaging system is embedded in the re-entrant window, we usually need to remove the objective lens.

4.2 Characterization of the vibration

A stimulated two-photon Raman process using a pulsed 355 nm laser is used to produce the spin-spin interactions. Because of this, any displacement of the ion chain that occurred during the contact period that was on the order of the wavelength of the Raman laser would create an undesirable phase shift in the ions. As a result, it is of the most importance to minimize the vibration that occurs inside this Gifford-McMahon closed-cycle cryostat.

4.2.1 The Michelson interferometer

Although there are many different instruments for measuring vibration signals, such as capacitive sensors for vibration measurement, most of them are not suitable for use in our systems. Measurement of vibration signals in UHV systems at cryogenic temperatures is mainly done by non-contact measurement, and the use of lasers is a very good solution for non-contact measurement, which is also suitable for our systems. There are two main solutions for measuring position information based on laser, the laser Doppler vibrometer and the laser interferometer. The Laser Doppler vibrometer measures the spectrum of vibration signals mainly according to the Doppler principle. Its measurement accuracy is dependent on the speed of the object's movement and is therefore very accurate for high frequency signals. However, the cryostat vibration signal does not generally exceed 200 Hz. we are concerned on the one hand with vibration signals that may change the relative phase between the ion and the laser during the laser manipulation sequence, which can usually be measured on the cryostat at frequencies between 10 Hz and 200 Hz and amplitudes between 1 nm and 100 nm. In this frequency range, the laser Doppler vibrometer is not very accurate. On the other hand, we are concerned with the displacement of the trap relative to the optical path over a long experimental period, e.g. one hour. The accuracy of the Laser Doppler vibrometer in measuring this long term drift is very low, typically measured with an error of no less than 100nm, mainly due to the fact that most laser Doppler vibrometers use a velocity integration method to calculate the displacement.

The laser interferometer is a class of instrument that is commonly used for measuring displacement and its principle and performance meet our requirements for vibration measurement. Unlike the more industrially used dual-frequency laser interferometer, I have built a very simple Michelson interferometer in my laboratory, as shown in Fig 4.4, because commercially available laser interferometers are generally not compatible with

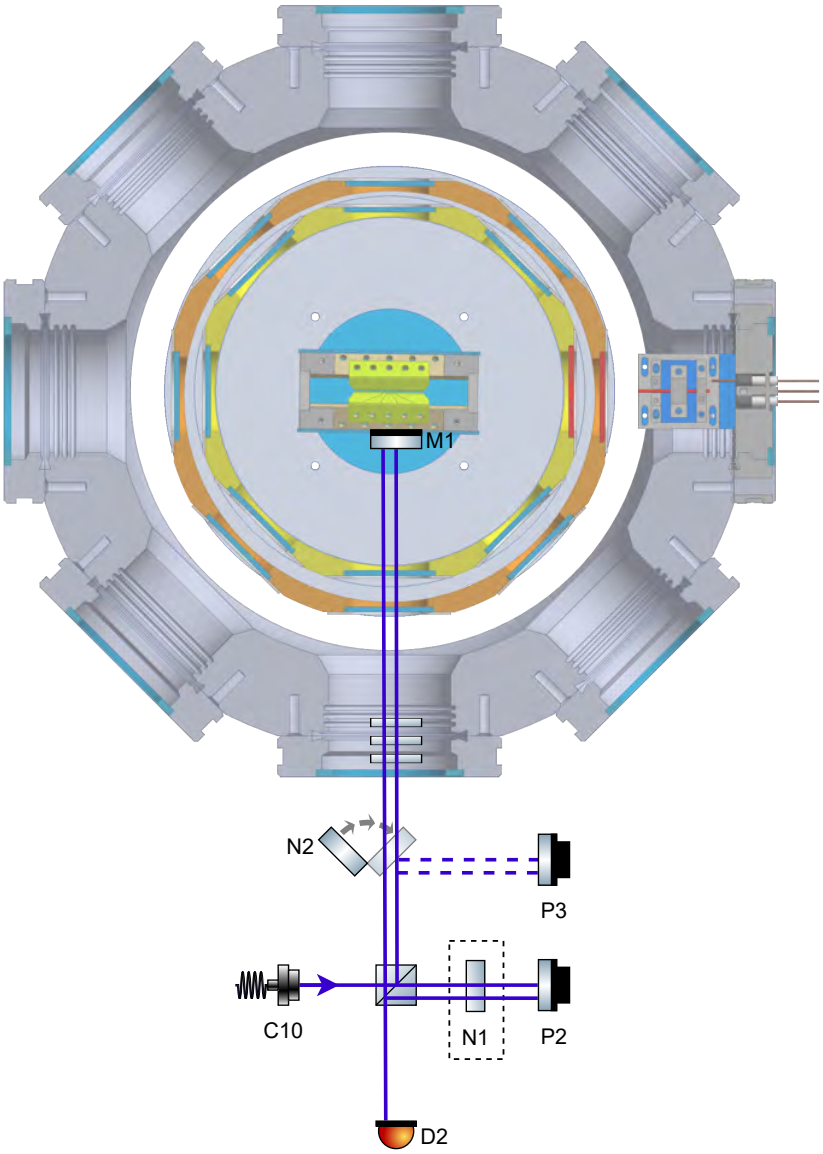

Figure 4.4 Optical layout of the Michelson interferometer.

ultra-high vacuum systems and are not suitable for use in very compact chambers.

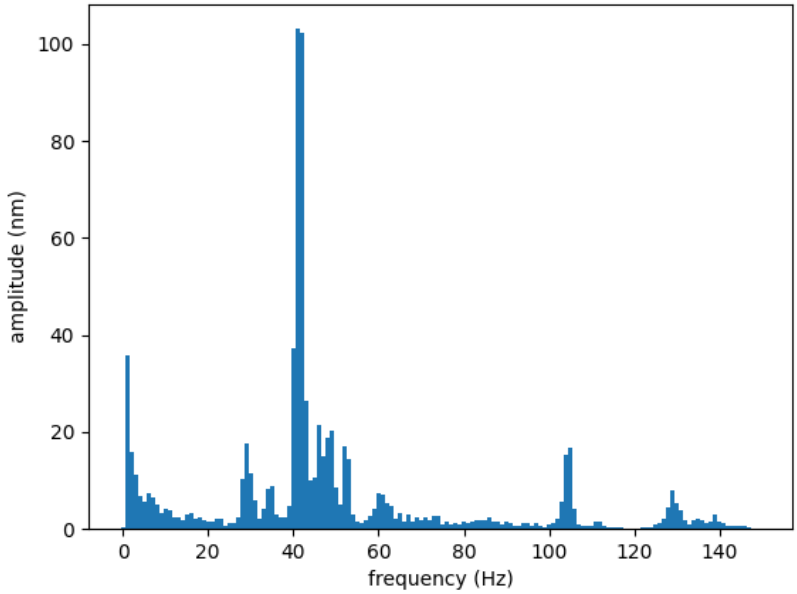

Figure 4.5 Vibration in the horizontal plane of this cryostat.

Experimentally we will fix a small reflector (M1), about 6mm in diameter, to the trap holder, which is located in the 4 K reigon inside the cryostat. We have tried using silver epoxy to hold the mirror to the trap holder, but usually the epoxy is detrimental to our ability to obtain XHV and it would be better to use UHV compatible plastic screws to hold the mirror in place. Since it is so well fixed, we believe that the trap displacement can be calculated by measuring the change in the relative optical path of the reflector. The laser is emitted from outside the chamber and then returned from inside the chamnber through six transmissions and one reflection from the reflector, 4 K shield glass, 40 K shield glass and the viewport of the vacuum chamber. Therefore, it is often necessary to place an optical coating on the surface of these glasses to increase the transmission and reflectivity and thus improve the signal-to-noise ratio of the interferometric signal. If the coating of the glass does not match the wavelength of the laser, some measurement accuracy may be lost, but this is not fatal and it is advantageous to relax the wavelength range required for the optical coating for a more scalable cryostat design. We have tried using retroreflectors instead of mirrors. Since retroreflectors are not sensitive to changes in angle, if the reflector is disturbed by a vibration pulse during the measurement resulting in a change in angle, the signal-to-noise ratio of the interferometric signal is significantly reduced, which can be avoided by using a retroreflector. However, due to the UHV and

the very small size of the chamber, the signal-to-noise ratio of the interferometric signal from the retroreflector is significantly lower than that of the interferometric signal from the reflector. On the other hand we have optimised the design to reduce the vibrations and the angular shift generated by this pulsed signal is suppressed, so that for systems with small vibrations the use of a reflector is a better option.

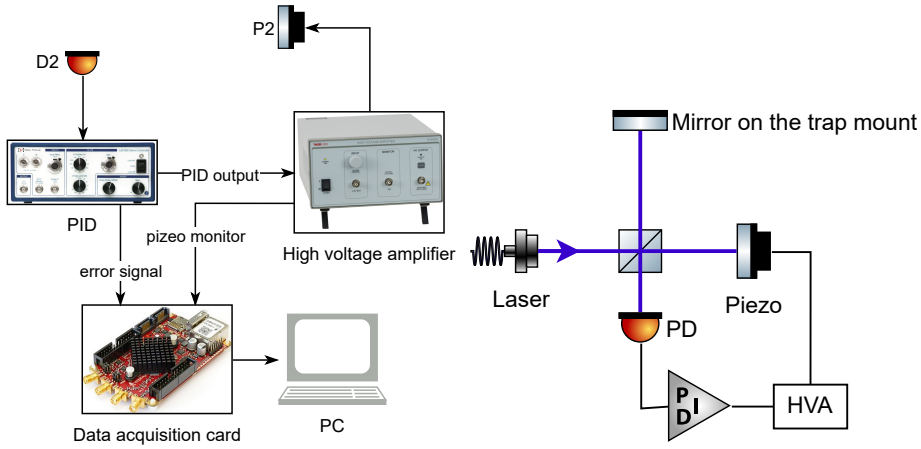

(a) Picture of real products. (b) The circuit diagram.

Figure 4.6 The circuit diagram of the Michelson interferometer.

A Michelson interferometer-based measurement solution requires a very stable laser source. Or rather the measurement error is directly related to the jitter of the laser source. This is because we do not currently use a solution similar to the Mach-Zehnder interferometer, so the PID can only be locked to the rising edge of the fringe of the signal, and the addition of a modulation module would reduce the interference caused by laser source jitter, i.e. improve the signal-to-noise ratio. Experimentally, the coherence length of a single-frequency laser should be much greater than 1 m, and the power and polarisation jitter should ideally be less than 1%, and at worst no more than 5%. Fortunately, the 370nm laser (C10) we use meets these requirements and can be used as the laser source for the laser interferometer, thus reducing the cost of building the instrument ourselves. One arm of the interferometer comes from the return laser from the reflector on the trap holder and the other arm comes from the return laser from the reflector fixed to the optical table (P2; PA44LEW Throlabs), so we can measure the change in the optical range of the trap relative to the optical table. The interferometric laser is directed at the photodiode and the photocurrent is passed through the transimpedance amplifier to generate an interference voltage signal. The error signal generated by the PID module is then output to a high voltage amplifier, which generates a voltage signal to drive the piezoelectric ceramic on the optical stage reflector. This creates a phase-locked loop and by reading the

value of the voltage signal from the piezoelectric ceramic we can determine the change in the optical path of the reflector on the trap holder. The feedback bandwidth of this loop is approximately 1 kHz, which is limited by the bandwidth and linear operating range of the piezoelectric ceramic. We have increased the feedback bandwidth of the phase-locked loop by choosing to use a high bandwidth piezoelectric ceramic and a small mass of reflector as a load on the piezoelectric ceramic.

4.2.2 High-precision long-term vibration measurement

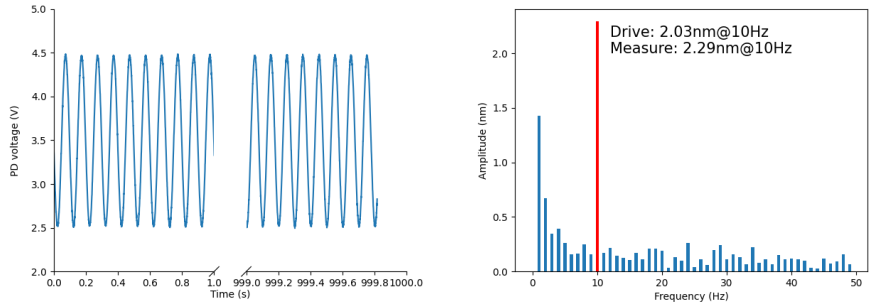

(a) Interferometer with high stability. (b) Interferometer with high precision.

Figure 4.7 Interferometer with high stability and precision.

Before a mature cryostat is developed, we usually debug some experimental phenomena and experimental parameters repeatedly in our experiments. These problems due to the immaturity of the cryostat can arise from mechanical design, optical errors and electrical noise. We usually analyse these problems by comparing a cryogenic trap system with an room-temperature trap system, which is simpler in structure and therefore more stable. So a stable cryostat can greatly guarantee the rapid forward movement of our experimental process. Some stability may be necessary, such as vibrations in the laser manipulation sequence, which may affect the quantum gate fidelity, and long-term drift, which may affect the possibility of individual addressing. It is therefore necessary to experimentally measure the trapped ions with respect to the laser's optical path precisely and over a long period of time to achieve passive stabilisation of the various parameters of the cryostat. Fig 4.7 proves that this interferometer is very stable and the measurement result is precise.

Before carrying out the measurements, I calibrated the instrument. The wavelength of the laser coming out of the single-mode polarisation-maintain fibre (C10) was 370 nm, and I first checked the stability of the power and polarisation of the light coming out of the fibre by connecting it to a power meter and a polarisation analyser respectively. After confirming the stability of the laser source, I also checked the long-term stability of

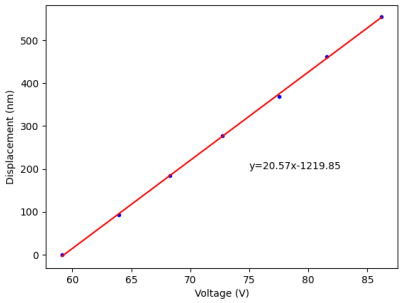

Figure 4.8 Voltage-to-displacement conversion of the piezo.

the interference signal, mainly by measuring the stability of the maximum and minimum values of the interference signal. I used epoxy glue to glue the reflector, piezoelectric ceramic and mirror mount together. Although the product manual for piezoelectric ceramics gives a relationship between displacement and voltage, in practice I have found that the linearity of these mirrors varies considerably from one production to the next, and in some cases the linearity changes after a few months. It is therefore necessary to calibrate the relationship between the displacement of the mirror and the voltage, as shown in Fig 4.8. I use a flipper mirror (N2) to change one arm of the interferometer from the cavity to another mirror on the optical stage, as the change in the interference signal at this point is so small that it can be assumed that there is no additional vibration. I applied a drive signal to the piezoelectric ceramic of the reflector to be calibrated and could see the interferometric signal oscillate. The relationship between the driving voltage and the interference signal deviates from sinusoidal oscillations because the driving relationship is not linear and the change in the angle of the mirror during the application of the driving signal causes a consequent change in the contrast of the interference signal. I calculated the optical path by selecting the eigenpoints of the interferometric maximum and minimum values. In the end, I can calculate the linear coefficients of the driving voltage and displacement for each manufactured reflector. In principle I could measure the vibration signal of the trap immediately, but to ensure that the measurement was correct I carried out a simulation experiment. By applying a drive signal to the mirrors of the other arm of the interferometer, the linear coefficients of voltage and displacement of each mirror were of course calibrated, and then the drive signal of the measured mirrors was read out. A comparison of these two signals gives the measurement accuracy.

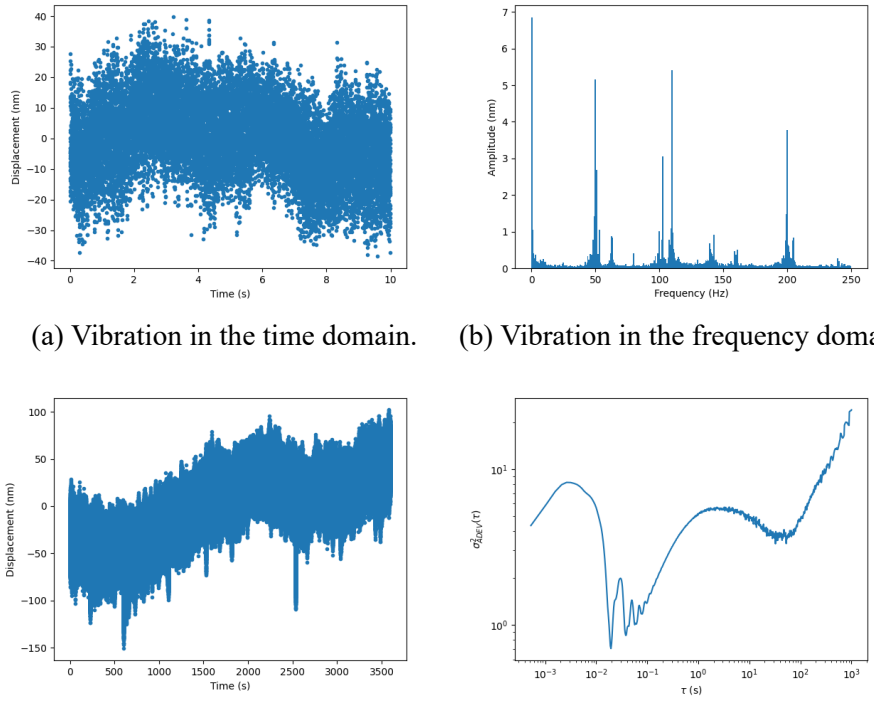

(a) Vibration in the time domain.

(b) Vibration in the frequency domain.

(c) Long-term vibration.

(d) Allan variance of long-term vibration.

Figure 4.9 Vibration in the horizontal plane of the cryostat after optimization.

4.2.3 Minimize vibration of the cryostat

In our laboratory, the vibration of the optical elements on the floating optical platform is around a few tens of nm, and our ultimate goal is to reduce the vibration of the cryostat to this order of magnitude. In our initial cryostat setup, the vibrations were in the order of a few hundred nm, half of which stemmed from the instability of the internal structure of the chamber and the other half from the vibrations caused by the cold head. Since vibrations of several hundred nm were also measured when the chiller was switched off, we decided to reinforce the internal structure of the cavity. In addition to the vibrations over a short period of time, the ions produce a translation of 1-10 μm during the process of doing the experiment, which indicates a long drift inside the chamber in response to environmental changes, as evidenced by the interferometer measurements. We first modified the support point in the 4 K region of the cavity. Previously the support passed through the whole of the exchange gas region and was therefore subject to long drift due to changes in the environment of the exchange gas region. We have now moved the support to the 300 K region and shortened the support material. Although we will lose some refrigeration capacity, we have solved the problem of long drift. We found that the suspension design

did not allow enough support points for the 4 K shield and 40 K shield, so we added PEEK connectors to the bottom of the shield. By optimising the structural design of the cavity, we managed to solve the vibration and long drift problems. Fig 4.9 shows the vibration signal of the optimised cryostat.

4.3 Obtain impedance match of helical resonator

If the RF voltage is applied directly from the RF amplifier to the ion trap, the following problems may be caused. An impedance mismatch between the RF amplifier and the ion trap will cause the RF signal to be reflected from the ion trap, resulting in power dissipation in the output impedance of the RF amplifier. The RF amplifier will also input noise into the ion trap, which may lead to heating of the ions. So we connect the output of the RF amplifier to a helical resonator. Due to the damping effect of the output impedance of the RF amplifier, connecting the helical resonator directly to the RF amplifier will reduce the quality factor of the spiral resonator, so this connection can be achieved by capacitive or inductive coupling, thus decoupling the helical resonator from the resistive output impedance of the RF amplifier, as well as giving the spiral resonator a high quality factor. This technique allows the impedance of the ion trap and the RF amplifier to be matched by varying the coupling, thereby reducing the reflected power and therefore the output power of the RF amplifier when the voltage required to generate the ion trap is reduced. Passing the output of the RF amplifier through a resonator allows the noise to be filtered and its contribution to the ion heating to be reduced to the greatest extent possible due to the high quality factor and narrow bandwidth of the resonator.

This shows that it is very important to obtain a high quality factor and to achieve impedance matching for the blade trap. For the room-temperature trap, we can feed the RF signal into the blade trap via feedthrough after the vacuum chamber has been established, so we can assemble and test the helical resonator that generates the RF signal on the optical stage. For the cryogenic trap we need to place the helical resonator inside the vacuum chamber. This reduces the circuit resistance to obtain a high quality factor, maintains the relative temperature stability of the helical resonator and the blade trap, and reduces electrical noise by reducing the circuit length and temperature. At the same time the quality factor is very much improved at low temperatures due to the reduced resistance compared to a room-temperature trap. However, the impedance matching is disrupted due to the reduced resistance at low temperatures and we need to find a way to

achieve impedance matching at low temperatures. The impedance matching parameters can be found using the dichotomous method by repeated warm-up and cool-down test operations, but a single warm-up operation lasting at least 2 days is too cumbersome. By modelling the RF system and measuring the system parameters in a single run, we can find a convenient way to adjust the impedance matching.

We can indirectly measure the loaded quality factor of the helical resonator by using the S_{11} parameter measured by the vector network analyzer.

$$Q_L = \frac{Q_U}{1+\kappa},\ \kappa = \begin{cases} \text{SWR}, & \text{over couple} \\ 1, & \text{critical couple} \\ 1/\text{SWR}, & \text{under couple} \end{cases},\ \text{SWR} = \frac{1+|\Gamma|}{1-|\Gamma|}, \tag{4.1}$$

where Q_L is the loaded quality factor, Q_I is the unloaded quality factor, κ is the coupling coefficient of the resonator, SWR is the standing wave ratio, Γ is a complex number that describes both the magnitude and the phase shift of the reflection.

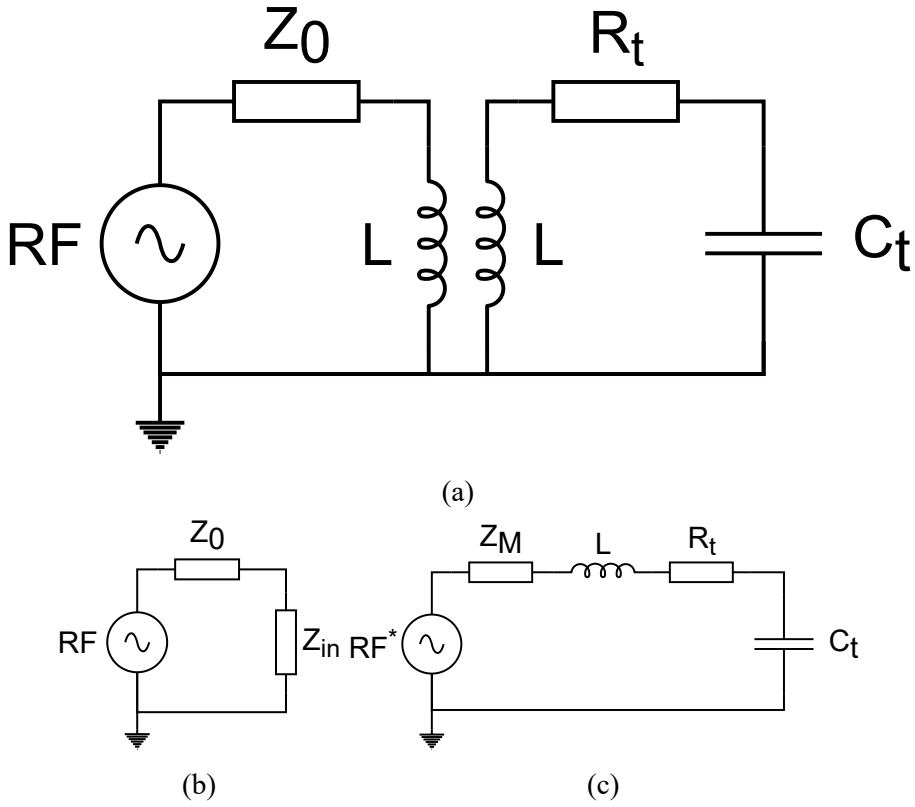

Figure 4.10 Circuit diagram of the helical resonator.

Fig 4.10 shows the circuit diagram of the helical resonator. Z_0 is the internal resistance of the RF signal source, Z_0 = 50 Ω, L is the inductance of the antenna and helical

copper wire, R_t is the AC resistance of the trap, C_t is the equivalent capacitance of the trap, Z_{in} is the equivalent impedance of the trap, and Z_M is the equivalent impedance of the mutual induction.

$$\begin{aligned} Z_{in} &= i\omega L + \frac{(k\omega L)^2}{i\omega L + R_t + \frac{1}{i\omega C}}, \\ Z_M &= \frac{k^2\omega^2 L^2}{i\omega L + Z_0}, \end{aligned} \tag{4.2}$$

where k is the coefficient of mutual induction. When the circuit is resonant, the imaginary part of the total impedance in Fig 4.10(c) is 0. The frequency at this point is,

$$\omega = \frac{Z_0}{L}\sqrt{\frac{\alpha - 1 + \sqrt{(\alpha+1)^2 - 4\alpha k^2}}{2\left(1-k^2\right)}}, \alpha = \frac{L}{Z_0^2 C}. \tag{4.3}$$

When we obtain impedance matching by adjusting the antenna coupling k, $Z_{in} = Z_0$ in Fig 4.10(b),

$$\begin{aligned} k &= \sqrt{\frac{R_t}{Z_0} + \frac{C}{L}R_t\left(Z_0 - R_t\right)}, \\ \omega &= \sqrt{\frac{Z_0}{LC(Z_0 - R_t)}}, \end{aligned} \tag{4.4}$$

We can now answer the question as to why the empirical operation of pulling a copper tube antenna out to impedance mismatch at room temperature is valid. During the cool-down process, R_t decreases continuously, so that K is smaller at low temperatures than at room temperature. The only experimental parameter that we have not been able to obtain so far is R_t at low temperature, which is difficult to predict theoretically, so we can derive this from a single cool-down progress.

CHAPTER 5 STABLE TRAPPING OF MULTIPLE IONS

For a newly built cryogenic trap system, the experimental implementation of stable trapping of multiple ions may take most of the project time before some quantum computing or quantum simulation experiments can be carried out. Experimental implementation of stable trapping of multiple ions involves not only achieving long-lived ion crystals, but also testing a stable standard experimental flow, debugging the experimental platform for various sources of noise, and developing an automatic experimental control system. From a project perspective, it is also a good idea to iterate and optimise the system while achieving stable trapping of multiple ions, and then try to solve the problem when the experiment gets stuck somewhere. Personally, I think more attention should be paid to experimental implementation of stable trapping of multiple ions, because for complex systems, the duplication of effort involved in finding a problem and then solving it can make the total time spent more than the time spent on building a stable experimental system in advance. However, the experimental implementation of stable trapping of multiple ions may not be well defined, and this may become a hole in the methodology.

5.1 Semi-automatic experimental control system

We usually divide the experimental tasks into daily operation tasks and current experiment tasks. The boundary between the two is not clear and we add some daily operation tasks by summarising some of the experimental tasks that have already been solved. Daily operation tasks can also be called experimental setup's parameters calibration tasks. For cryogenic trap systems, daily operation tasks also include the long-term monitoring of some system parameters. In an ideal laboratory environment it is possible to implement an automatic experimental control system, but in most laboratories we can only strive for a semi-automatic experimental control system. This is because some key points have to be controlled and checked by humans, mainly from some uncontrollable human disturbances.

Semi-automatic experimental control system mainly refers to the software system, which contains the front-end system, the back-end system, the database system and the experimental workflow.

The front-end system is the graphical interface that enables the experimenter to con-

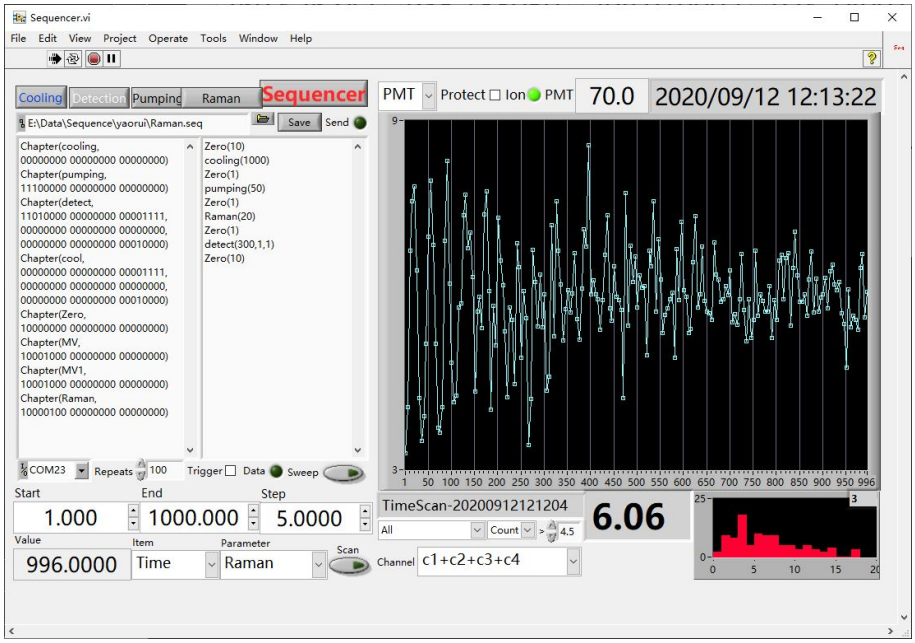

Figure 5.1 Labview front-end program (Sequencer).

duct experiments. The popular front-end technologies are client-side front-end technology and Web front-end technology. The more commonly used client-side front-end software in the laboratory are Labview, Mathematica, Matlab and other commercial software, which have rich functions and a friendly programming environment. I have written client-side front-end software based on python and pyqt5, as well as web front-end based on HTML5 technology in the course of my experiments. We can start building the experimental platform without focusing too much on front-end development, as these technologies are not necessary for physics research, and front-end technologies are rapidly growing, so it is possible to leave the front-end system to the professionals.

The back-end system is one of the core elements of the semi-automatic experimental control system. A unified back-end system will speed up the development of the entire semi-automatic experimental control system and facilitate communication and cooperation between project team members. We need the back-end system to control the experimental apparatus in a stable manner and in accordance with the experimental targets. There are a very large number of programming languages for developing back-end systems, suitable for use in the laboratory are C, python, etc. We can also consider using software that integrates front and back ends such as Labview, Mathematica, Matlab, etc. A good back-end system must adhere to lab safety rules, have a good logging system, have a good working state set, be stable over time and have a fast response time. If you are working with multiple people you need to consider version control and documentation

for development, such as code hosting. Long-term stability requires a good architecture, as instrument switches and new instrument additions occur frequently and the back-end system should not be offline too often. Instrument control protocols based on sockets and SCPI commands, mqtt protocol based instrument control protocols etc. can be considered. Fast response requires that the back-end program should have a response time of no more than 10-50 ms, which should be met in order to be able to perform complex operations.

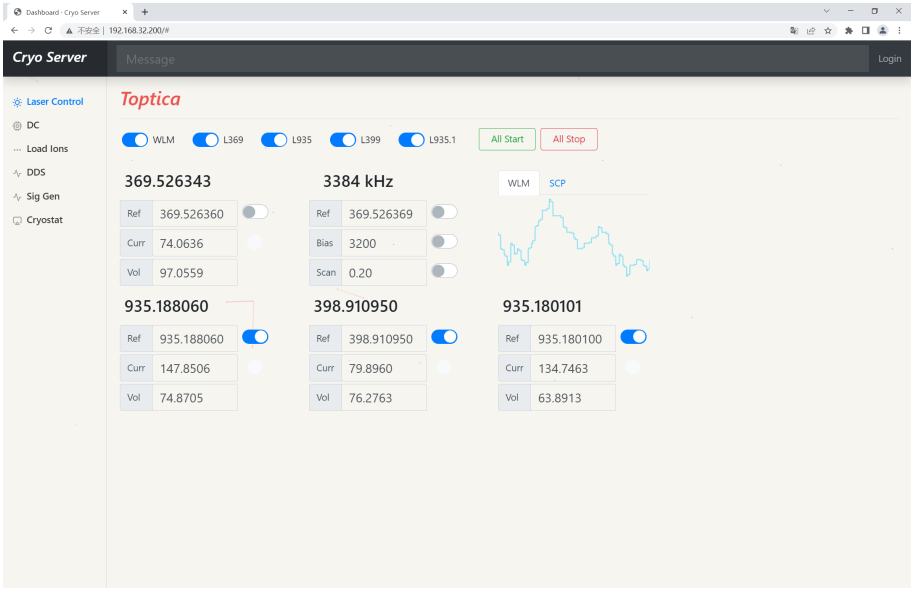

Figure 5.2 Web front-end program (Lasers etc.).

The database system has to take on the task of not only storing data but also taking into account data security. The database system on the experiment should take into account versatility and scalability, and should meet the needs of experimenters of different programming levels to use it. In addition to using SQL databases, InfluxDB, etc., it is also possible to use direct forms of experimental logs and file directory management, or even to use software such as excel directly for recording and management. In short, the database system should be compatible and easy to use as long as it exists and is standardised.

The experimental workflow does not primarily involve work on the code side of things. It is more like a framework bringing together the front-end system, the back-end system and the database system. We need to think about how to easily present the database and access historical data in the front-end system. We need to use it to log, deliver and present the results of experiments. We need to design daily operations and current experiments and easily code the corresponding tasks. Using Mathmatica's notebook or using something like IPython based Jypyter will allow us to do this very well.

During the early build of the lab, we should implement scripted, semi-automated

tests under the command of an experimental workflow as soon as possible. With this layout, instead of focusing on front-end system development, we can focus on experimental workflow and database system refinement, while the back-end system can be updated with versioning to patch bugs and improve performance.

5.2 Monitor axial electrical potential drift

We often perform parameter calibration operation at trapping around 10 ions, but if current experimental tasks require ion number between 100 and 200, we need to perform parameter calibration at this ion number scale. This is because repeatedly changing the number of ions in a trap is an operation we do not want to perform. For a well-built blade trap, the upper limit of the ion number of 1D ion chains that can be stably trapped is fixed. When the ion spacing is close to the diffraction limit of the imaging system, we cannot obtain precise information on the ion position from the CCD and the crosstalk between the ions during state detection is too large for high fidelity state detection. In this case we increase the radial trap frequency by increasing the RF power and decrease the axial trap frequency by decreasing the DC voltage. However, there is an upper limit to this method of regulation. When the radial trap frequency is too high, RF heating will occur and the ion crystal will not be stable and will dissolve. In addition, when the ion chain length exceeds the width of the central electrode, we find an asymmetry in the imaging and structure of the ion chain. The asymmetry in the imaging of the ion chain is due to the aberration of the imaging system, we can optimise the imaging system to achieve a field of view of 300 μm, but it may be more difficult to achieve 600 μm. The asymmetry of the ion chain structure is due to the asymmetry of the blade electrode and the drift of the background electrical potential.

It is difficult to investigate what the source of the background electrical potential is, but it is objective and there may be more than one source. This phenomenon is clearly observed when we make the ion chain length exceed the width of the central electrode. When the DC voltage is set to a symmetrical value, the ion chain configuration tends to be asymmetrical. This asymmetry also changes over time, either after a day or after a month. It is inevitable that we will do something to the trap in the meantime. This asymmetry can be clearly observed if the oven current is raised to observe the fluorescence of the Yb flux, and the ions can be loaded without turning on the oven during at least one day. This asymmetry changes slowly if more than 200 ions are repeatedly loaded at a time over a

period of more than a week, which can be explained by the ions adhering to the surface of the blade after the crystal has been destroyed. We can compensate the background electrical potential with the DC voltage and produce the desired harmonic potential, but when the background electrical potential exceeds the range we can compensate for, we should find a way to eliminate the causes of the background electrical potential drift.

For a complex system, a restart operation is often an effective method. I will try to raise the temperature to room temperature or above 40 K. Over the course of several experiments I have observed that the background electrical potential is removed, which can be quantified by the maximum number of ions that can be stably trapped, or characterised by the asymmetry of the background electrical potential. However, I have occasionally observed that this restart operation does not work completely, and in general this restart operation is effective, but lacks sufficient quantitative data to generalise the factors and values that are truly effective.

5.3 Calculate axial electrical potential with 1D ion chains

We can calculate the axial electrical potential with 1D ion chains. we can use a CCD to measure the position of each ion in the 1D ion chains. this measurement is usually subject to error, and the error is different for different positions of the ions. For a chain of ions, the aberration is smaller for ions near the centre of the field of view and larger for ions near the edge of the field of view. If the ion chain exceeds the edge length of the CCD sensor, we can also measure the position of the ions in sections by moving the objective. In addition to the measurement error, the algorithm used to calculate the ion position can also produce a corresponding error. Commonly used algorithms for measuring ion positions are linear algorithms based on computer vision, which have the advantage of being fast and able to give results within 10ms. The other algorithm is a fitting-based algorithm, which is less fast and less convergent and is very dependent on the signal-to-noise ratio, but can achieve high accuracy with the right parameters. We can then use the algorithm to find the equilibrium position of the ion chain for a given number of ions and the electrical potential parameter as a calculated value. The difference between the measured and calculated values can then be fed back to the electrical potential as a function of error, so that the parameter with the lowest error, i.e. the axial electrical potential at this point, can be iteratively found.

Fig 5.3(a) shows the use of Mathematica's code to identify a typical ion chain image.

```
IonPositionReadOutWithSpecialParameter[im_] :=
 Module[{filtedImage, edgeofImage, m, centerPosition, component},
  edgeofImage = EdgeDetect[im, 2.5`, 0.052`, Method → "Canny"];
  m = MorphologicalComponents[edgeofImage] // Colorize;
  component = ComponentMeasurements[m, {"Centroid", "FilledCircularity"}];
  centerPosition = Table[component[[i, 2, 1]], {i, 1, component // Length}]]
```

(a) Mathematica code.

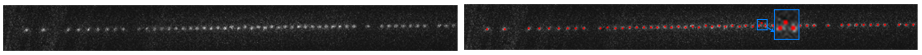

(b) Raw image. (c) Image after processing.

Figure 5.3 Usage of Mathematica's code to identify a typical ion chain image

Fig 5.3(b) and Fig 5.3(c) show the original image and the processed image respectively, with the red dots representing the centre of the identified ions. The background scattered light and the aberration of the image can have an effect on the result of the identification. As can be seen from the recognition results in the blue box in Fig 5.3(c), the trailing of a particular ion may be determined as a new ion, but the conformation of the ion chain precludes this possibility. Optimising the algorithm may be a good idea, but the noise introduced by the imaging system will not be eliminated. Even if the recognition algorithm is optimised using criteria such as no jump in neighbouring ion spacing, ion chain linearity judgement, etc., the noise will still reduce detection fidelity during state detection, and the benefit of reducing noise by optimising the imaging system is much greater. Fig 5.4 shows code using python to recognise an image of a long ion chain. The algorithms used are similar, so are prone to recognition errors for larger ion chains.

Now that we are able to obtain information on the location of the ions, we next use a ingenious algorithm proposed by Yukai Wu to calculate the axial electrical potential. The idea of the fitting is very simple. For given trapping potential, we can compute the equilibrium positions of the ions. Then we can adjust the trapping potential to get a best fit of the measured ion positions. For this purpose, it is desired to use a discrete set of parameters to describe the trapping potential. For example, here we use the Legendre polynomials. To get better convergence properties, we scale the axial positions to about $[-1, 1]$, which can be recovered in the end.

In Fig 5.5 we present the fitting results for various ion numbers under the same settings of potentials and the CCD camera. Fitting results for (a, b) N = 6, (c, d) N = 9, (e, f) N = 13, (g, h) N = 19. The fitting of the trapping potential uses up to 2nd order

```python
def CVIONS_FAST(image, LoG_sigma=1.5, threshold=0.3):
    # some computer vision algorithms
    image_log = gaussian_laplace(image, LoG_sigma)
    image_log = 1 - (image_log - np.min(image_log)) / (np.max(image_log) - np.min(image_log))
    image_bn = np.where(image_log > threshold, 1, 0)
    image_lb = label(image_bn)
    # label ions
    lb_num = np.max(image_lb)
    para_num = 4
    para_cv = np.zeros((lb_num, para_num))
    for lb in range(1, lb_num + 1):
        count = image[image_lb == lb]
        wgt = count / np.sum(count)
        y, x = np.where(image_lb == lb)
        max_count = np.max(count)
        x0 = np.average(x, weights=wgt)
        y0 = np.average(y, weights=wgt)
        s = np.count_nonzero(image_lb == lb)
        para_cv[lb - 1, :] = [max_count, x0, y0, s]
    # calculate ion positions
    order = np.argsort(para_cv[:, 1])
    for i in range(para_num):
        para_cv[:, i] = para_cv[order, i]
    return para_cv
```

(a) Python code.

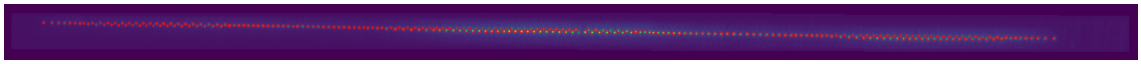

(b) Image of 245 ions.

Figure 5.4 Usage of Python code to calculate 245 ions' position.

polynomials(a, c, e, g) and up to 4th order polynomials (b, d, f, h). The blue and red dots are the measured positions and the fitted ones, respectively. The fitted data are lifted in the vertical direction to better distinguish the two sets of data. The green curves are the fitted axial trap potential. As we can see, 2nd order polynomials do not give good fitting results, but polynomials up to 4th order generally fit well.

Furthermore, we can see in Fig 5.6 that the fitted potentials for different ion numbers agree well with each other, apart from a constant shift which is not relevant to the equilibrium positions and has been removed. Fitted trapping potential for N = 6 (red), N = 9 (green), N = 13 (orange) and N = 19 (blue) ions.

Finally, we comment that the method can be applied to the case where dark ions exist, so long as we can identify the order of the bright and the dark ions. Then we simply use the positions of the bright ones in simulation to fit the trapping potential. As shown in Fig 5.7, the fitting results is almost the same if the number of dark ions is not too large. The fitting results for the N = 19 case in Fig 5.5 with the ion 6 and ion 9 chosen as dark ions. The fitted potential (green) almost overlaps with the previous one (black) where all the ions are bright.

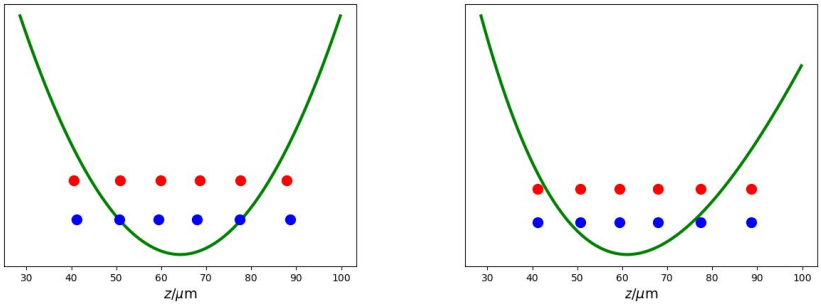

(a)

(b)

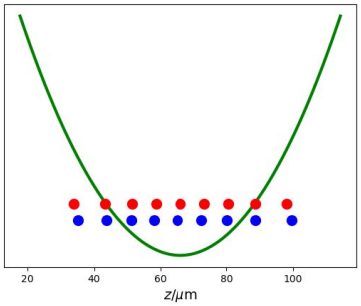

(c)

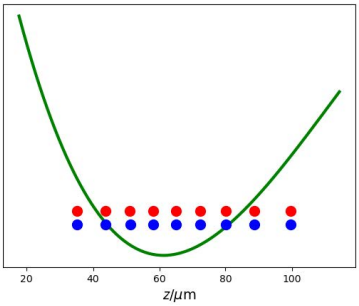

(d)

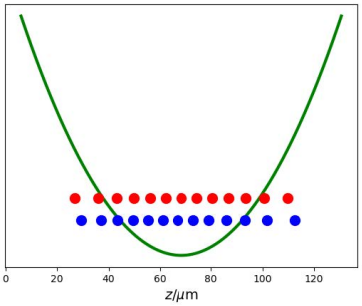

(e)

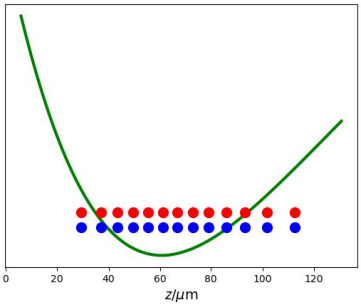

(f)

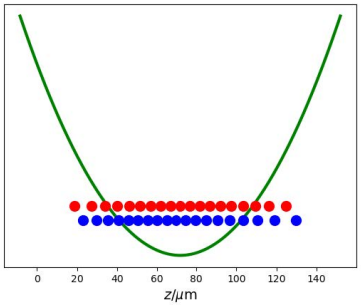

(g)

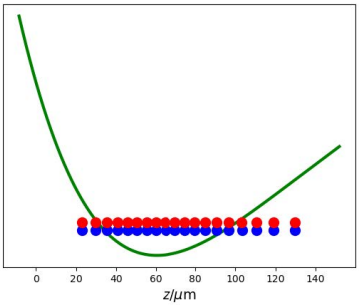

(h)

Figure 5.5 Fitting results for various ion numbers.

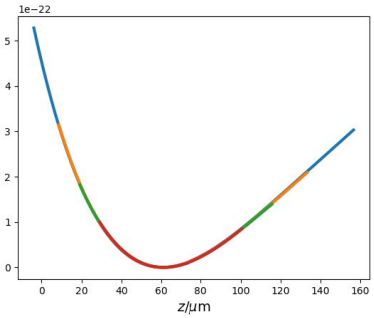

Figure 5.6 Fitted trapping potential for diferrent ion number.

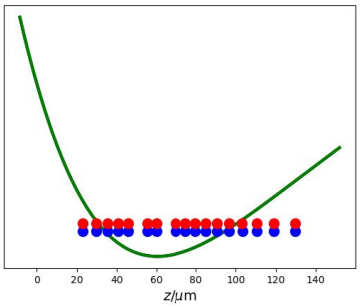

Figure 5.7 Fitted trapping potential with dark ions.

5.4 Fitting the electrical potential coefficient for each electrode

For a fixed electrical potential, we can capture different numbers of ions, as shown in Fig 5.8, 2, 12, 24, 34, 42. For each image, we can calculate the position of the ion and fit it to the electrical potential at that time. Red circles and dots on the right-hand side indicate the calculated position of the ion and the equilibrium position of the ion at the fitted electrical potential, respectively. The black dots indicate the presence of dark ions. The electrical potential can be expressed as

$$\phi_n(x) = \sum_{i=1}^{n} \alpha_i P_i(x), x = z/l_0, \tag{5.1}$$

where z is the true position of the ion, l_0 is half the length of the ion chain, $P_i(x)$ is the Legendre polynomial of degree i and α_i is the coefficient of the expansion.

Since the electrical potential has not changed, the fit should be consistent for different numbers of ions. As shown in Table 5.1, the coefficients of the Legendre polynomial have consistent convergence for data with 2 to 42 ions.

If we were to use this algorithm directly to calculate the coefficients of the electrical potential at different voltages, we would end up with scattered results due to overfitting.

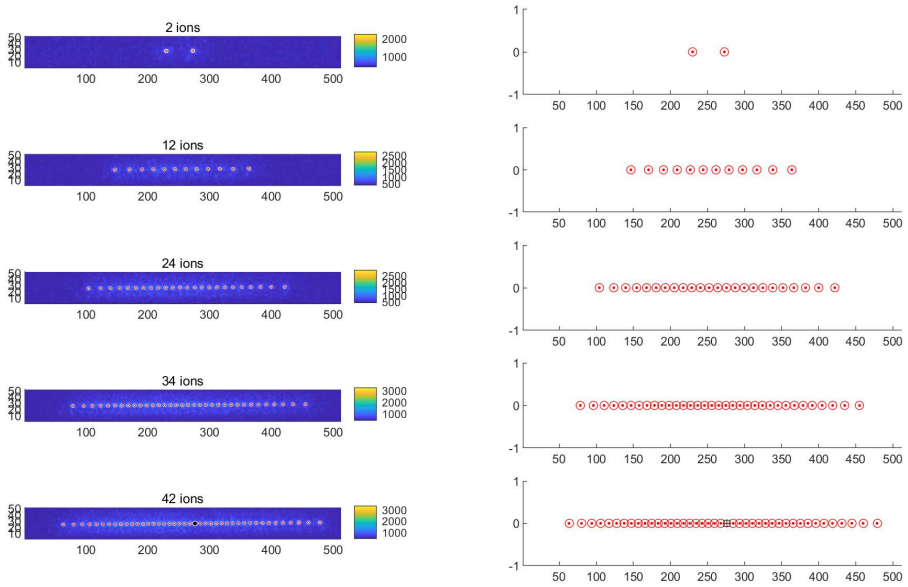

Figure 5.8 Fit trapping potential up to 42 ions.

Table 5.1 Fitting the electrical potential coefficient

Ion number	α_1	α_2	α_3	α_4
2	7.59183	212.463	0	0
12	12.5574	207.098	-45.04	40.0967
24	10.8866	204.913	-50.165	48.4474
34	10.8904	204.944	-49.784	48.0492
42	10.7205	205.988	-55.486	47.6406

So we need to assume that the coefficient of the electrical potential is fixed for each electrode and then decompose the electrical potential from the actual voltage into the sum of each electrode,

$$\alpha_i = \sum_{s=1}^{5} \alpha_i^s U_s \tag{5.2}$$

where α_i^s the coefficient of the electrical potential generated by each pair of DC electrodes, s is the order number of the electrodes, there are 5 pairs of electrodes in total. And U_s is the voltage applied to the electrodes.

I trapped 51 ions at a fixed electrical potential, as shown in Fig 5.9(a). Although the applied electrode voltage is symmetrical, the resulting potential field is asymmetrical, which is not what we want. I then added a fixed voltage to each pair of electrodes, at which point I could find the new electrical potential. The single result may have a large

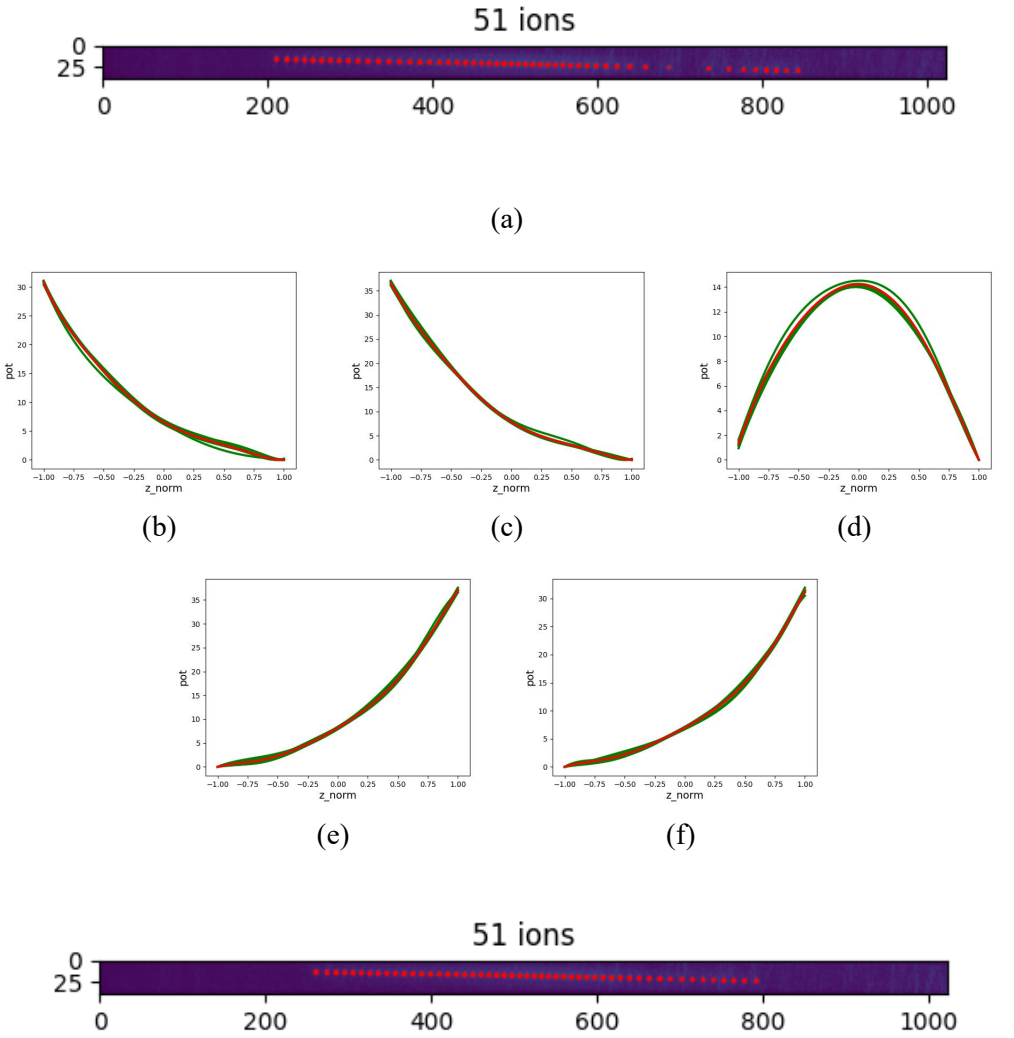

Figure 5.9 Fit the electrical potential coefficient for each electrode.

error, but if the voltage is increased in equal steps, it can be fitted to give α_i^s. In Fig 5.9(b)-(f), I have plotted the electrical potential generated by the 5 pairs of electrodes. The green line represents the increase in electrical potential for equal steps of increasing voltage, and you can see that the increase in electrical potential is fixed. The red line represents the average of these data, and I think this value can represent the coefficient of electrical potential generated by each pair of DC electrodes. Next I calculated at what voltage settings this asymmetry could be compensated for and then achieved the result shown in Fig 5.9(g), where the ions are equally spaced.

5.5 Stabilization of axial electrical potential

When the number of ions becomes larger, we encounter some challenges. On the one hand the applicability of the algorithm can be problematic. For a quasi-1D chain of 126 ions as shown in Fig 5.10(a), the original algorithm fails due to the emergence of the zig-zag configuration. Since the original algorithm is only valid for 1D ion chains, we can consider optimisation algorithms to solve this problem. On the other hand, when experimental parameters such as image aberrations, adjustable range of voltages, etc. can gradually become a major source of noise, they can cause excessive errors or be too unstable, and we can solve this problem by refining the physical system.

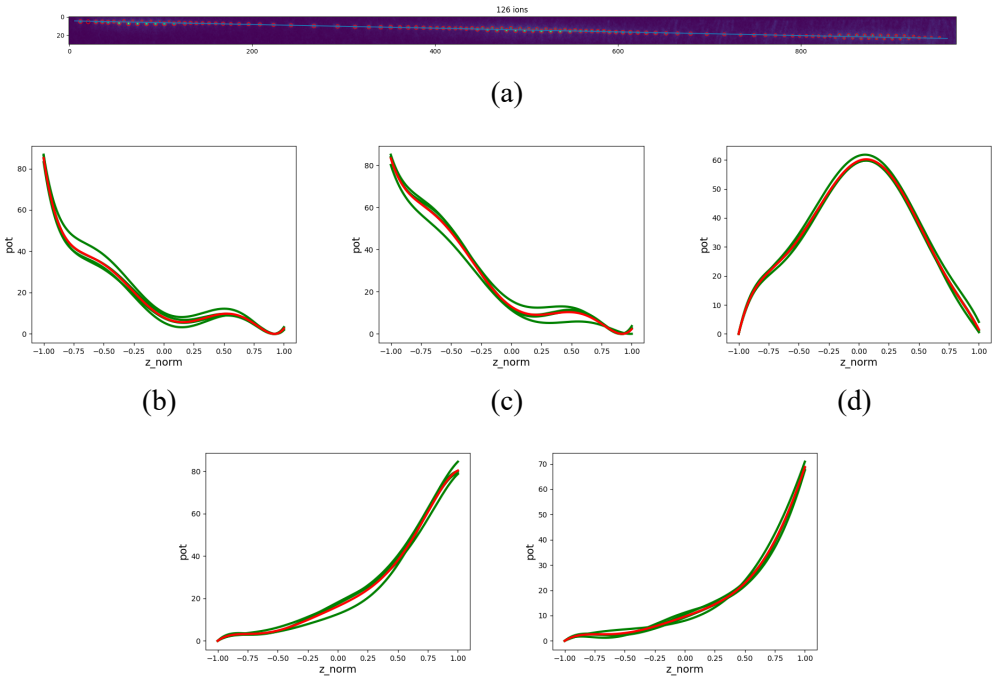

(a) (b) (c) (d) (e) (f)

Figure 5.10 Fit the electrical potential coefficient with a 126-ions quasi-1D chain.

There are a number of ideas for optimisation algorithms, one simple idea is to abandon the calculation of the theoretical equilibrium position for a given electrical potential and take the equilibrium position of the ion directly from the image and invert the electrical potential at this point according to Coulomb's law. Using this method we can obtain the electrical potential for five pairs of electrodes as shown in Fig 5.10(b)-(f). It can be seen that at this scale of ion numbers the error becomes larger.

CHAPTER 6 EXPERIMENTAL REALIZATION OF A 200-ION MULTI-QUBIT QUANTUM MEMORY

Storage lifetime and capacity are two important factors to characterize the performance of a quantum memory, which finds wide applications in quantum computers and quantum networks. The trapped ion system has reported the longest single-qubit storage lifetime above one hour, as well as the multi-qubit capacity up to tens of ions in shallow-depth quantum circuits. However, combining the two features still remains an experimental challenge due to the stronger noise in the multi-qubit environment. Here we report the stable trapping of above 200 ions in a zigzag structure, and demonstrate the combination of the multi-qubit capacity and long storage lifetime by measuring the coherence time of several arbitrarily chosen ions to be on the order of hundreds of milliseconds. We compare the performance of the quantum memory with and without the sympathetic cooling laser, thus unambiguously show the necessity of sympathetic cooling for the long-time storage of multiple ionic qubits.

6.1 Quasi-1D ion crystal

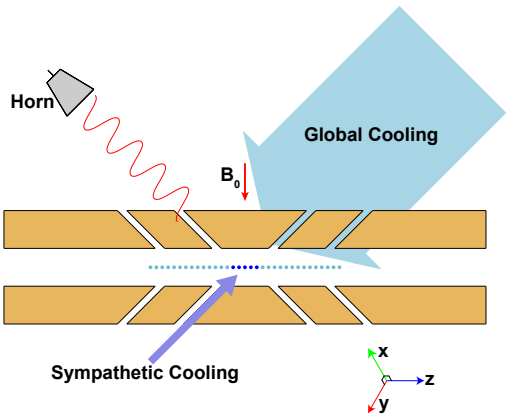

Figure 6.1 Schematic experimental setup.

To get a stable quasi-1D ion crystal, we use a blade trap in a closed-cycle cryostat[24] at a temperature of 6 K. As shown in Fig. 6.1, a 1D or quasi-1D ion crystal is confined in a blade trap under cryogenic temperature. A broad elliptic beam with tunable frequency and intensity can be used for global Doppler cooling, optical pumping and qubit state

detection, and a narrow sympathetic cooling beam propagating in the opposite direction can address about 5 central ions. A microwave horn antenna generates microwave signals to manipulate the states of the qubits. We apply a global Doppler cooling beam with nonzero angles to all the three principle axes. This global beam has 20 μW power and $\Delta = -2\pi \times 12$ MHz detuning, and is shaped into an ellipse with waist sizes of 15 μm×500 μm by a cylindrical lens. Opposite to this beam is a narrow 1 μW sympathetic cooling beam with the same detuning, which is focused to a beam waist of 10 μm to address about 5 ions in the center of the crystal. By setting the transverse trap frequencies $\omega_x \approx 1.6$ MHz, $\omega_y \approx 1.5$ MHz, and by engineering the axial trapping potential via the segmented electrodes (for the long ion crystal, the axial potential cannot be well approximated by a harmonic trap), we obtain a quasi-1D ion crystal of 218 $^{171}Yb^+$ ions in a zigzag shape, which can be stably trapped for hours under the global cooling beam.

Figure 6.2 The image of 218 ions in a zigzag structure.

An image of the 218 ions is shown in Fig. 6.2. The length of this quasi-1D crystal is about 800 μm and is wider than the FOV of the EMCCD camera of about 300 μm, so the image is stitched from three images taken sequentially with overlap in between. The blue arrows indicate the locations of five dark ions. The ions labelled as 1, 2 and 3 are used to demonstrate quantum storage in the following experiments. For an illustration of the whole ion crystal, we take photos sequentially for different parts of the ion crystal by shifting the position of the camera, and perform image stitching to combine them together. In the following when characterizing the storage capacity and the lifetime of the quantum memory, we apply sympathetic cooling laser to the middle ions[35] and store and read out qubit states on the edge, so that the shifting of the camera position is not needed.

6.2 Measure the storage time

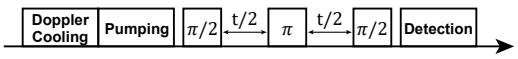

Figure 6.3 Experimental sequence.

We apply a global microwave to manipulate the qubit states through the spin-echo sequence shown in Fig. 6.3. We initialize the storage qubit in $|0\rangle \equiv |^2S_{1/2}, F = 0, m_F = 0\rangle$ of the $^{171}Yb^+$ ion (a dark state under 370 nm detection laser) through optical pumping,

and apply a $\pi/2$ pulse to prepare it in $(|0\rangle + e^{i\phi}|1\rangle)/\sqrt{2}$ where ϕ is the initial phase of the microwave signal. After the long-time storage with a spin echo (microwave π pulse) in the middle, we apply another microwave pulse to reverse the preparation step and finally measure the storage fidelity of the qubit state. Due to the nonuniformity of the microwave, we use SK1 composite pulses for the $\pi/2$ and π pulses to suppress the pulse area error. Ideally we will end in the state $|1\rangle \equiv |^2S_{1/2}, F = 1, m_F = 0\rangle$ (a bright state under the detection laser), and the decay in the population versus time can give us the storage lifetime of the quantum memory.

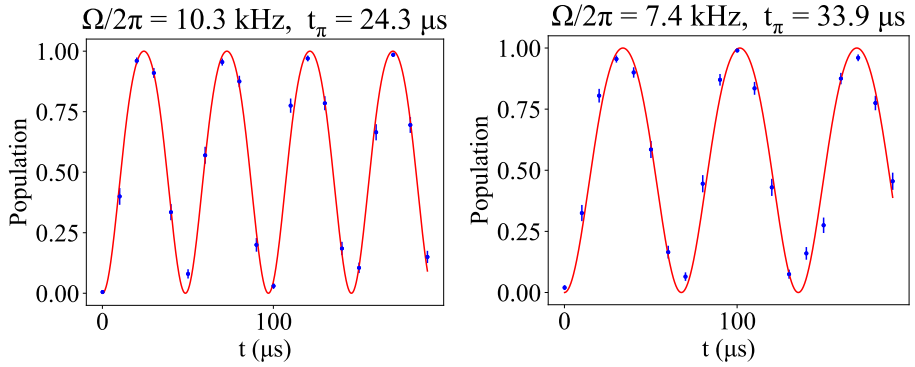

(a) Rabi oscillation of the ion on the left side of the ion chain.

(b) Rabi oscillation of the ion on the right side of the ion chain.

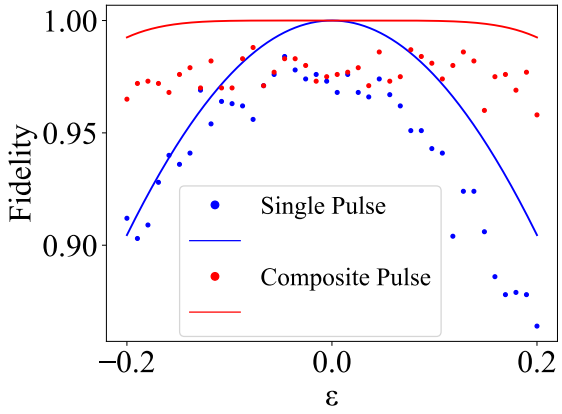

(c) Compare theoretical and experimental performance for the single pulse.

Figure 6.4 Usage of the SK1 composite pulse.

Due to the nonuniformity of the microwave signal, its Rabi frequency varies slightly for different ions, so we use the SK1 composite pulse[36-37] to suppress this pulse-area error to higher order. As shown in Fig. 6.4, there is about 30%-40% change in the Rabi frequency over 80 ion spacings, or about 0.5% change between adjacent ions, and the SK1 pulse can tolerate up to ±20% error in the Rabi frequency while still maintaining a fidelity above 99%. Here we use the Rabi oscillation of different sites in a chain of

about 100 ions to characterize the nonuniformity of the microwave signal. For two ions separated by 80 ion spacings, the Rabi frequencies of Fig 6.1 $2\pi \times 10.3\,\text{kHz}$ and Fig 6.2 $2\pi \times 7.4\,\text{kHz}$ are fitted. Fig 6.3 shows theoretical (solid curves) and experimental (dots) performance for the single pulse (blue) and the composite pulse (red) on a target ion. Theoretically, the SK1 composite pulse can tolerate up to $\pm 20\%$ pulse-area error while still maintaining a fidelity above 99%. Similar tendency is observed in the experiment and the overall reduction in the fidelity can be explained by the state-preparation-and-measurement (SPAM) error. Therefore, we can simultaneously initialize all the ions in the FOV of the CCD camera in the same state and operate them with the same gate, which allows efficient characterization of their storage lifetime without the need to repeat the experimental sequence for each ion. Note that here our purpose is to demonstrate the storage capacity and lifetime of individual ions in the crystal, so global operations plus individual detection suffice. In the future with an upgrade in the addressing system using focused Raman laser beams, the simultaneous storage of multiple qubits into nearby ions can also be achieved.

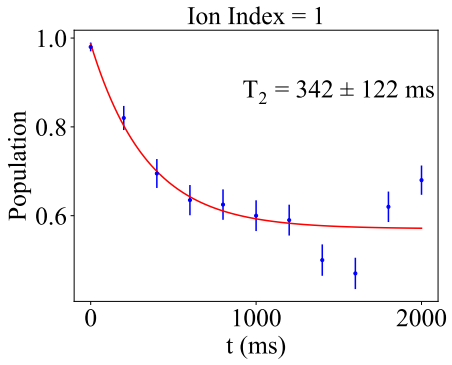

(a) Storage time for the 1st ions.

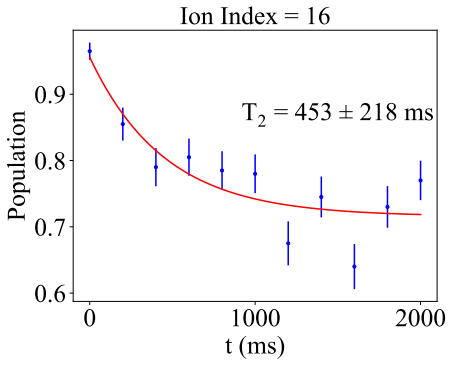

(b) Storage time for the 16th ions.

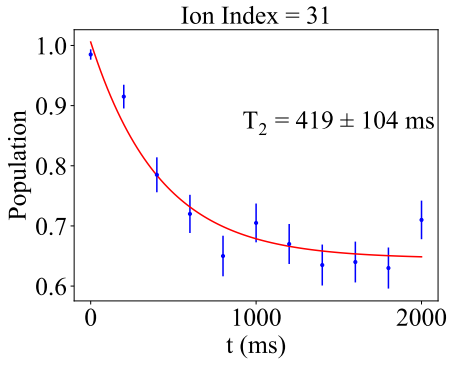

(c) Storage time for the 31st ions.

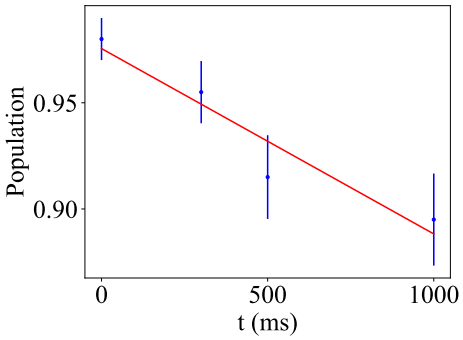

(d) The decay of the bright state population vs. storage time without the spin echo.

Figure 6.5 The measured storage fidelity vs. storage time.

We measure the storage lifetime of three typical ions [labeled as 1-3 in Fig. 6.2] away from the center of the ion crystal in Fig. 6.5(a)-(c). By executing the pulse sequence in Fig. 6.3, we get the average storage fidelity over the $|\pm\rangle = (|0\rangle \pm |1\rangle)/\sqrt{2}$ and $|L(R)\rangle = (|0\rangle \pm i|1\rangle)/\sqrt{2}$ bases[17], and fit the decoherence time $T_2 = (323 \pm 93)$ ms, (453 ± 218) ms and (419 ± 104) ms, respectively, for the three ions. The coherence time T_2 is fitted by the exponential function $F = A + Be^{-t/T_2}$. Each data point is repeated for 200 times with the error bar indicating one standard deviation. At large t, some data points deviate considerably from the exponential fitting function. This can be explained by the slow drift in the trap and laser parameters on the timescale of minutes to hours, and should not affect the extracted coherence time of hundreds of milliseconds. Nevertheless, a coherence time on the order of hundreds of milliseconds can be concluded. On the other hand, the $|0(1)\rangle$ basis is not subjected to the dephasing error and hence typically have longer coherence time[17]. For example, in Fig. 6.5(d) we see that, without the spin echo in the middle which does not affect the decoherence in the $|0(1)\rangle$ basis, the population decay from the bright state ($|1\rangle$) to the dark state ($|0\rangle$) for a typical ion has a timescale far above 1 s. Therefore we can bound the average storage lifetime over all possible qubit states by T_2 for individual ions.

6.3 Effect of the sympathetic cooling

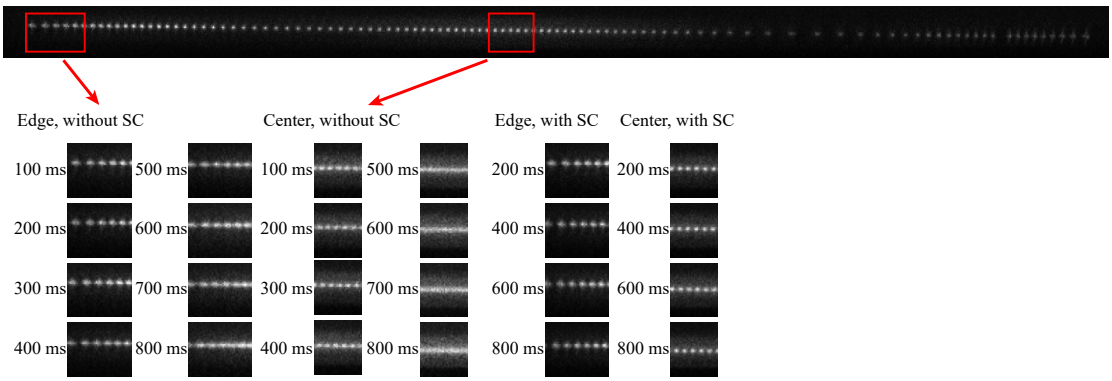

Figure 6.6 Compare the heating effect with or without sympathetic cooling.

The sympathetic cooling laser beam turns out to be critical for the functioning of this quantum memory: without the cooling beam, the ion crystal can quickly be heated up within hundreds of milliseconds that can cause difficulty in reading out the qubit state or even the meltdown of the whole ion crystal. Actually, for the quasi-1D 218-ion crystal, the heating dynamics is too fast to be examined from the images. Therefore we first

demonstrate the idea using a shorter chain of about 100 ions whose heating dynamics is slower.

The image of a 1D 103-ion chain under the same parameters as those for the crystal is shown in Fig. 6.6. To compare the heating effect with or without sympathetic cooling, we start from the same equilibrium state under global Doppler cooling, and then turn off the global cooling beam and evolve the system with the sympathetic cooling (SC) beam off or on. Each image is averaged over 200 repetitions.

The two columns on the left show the images of the edge ions and the central ions [indicated by the red boxes in (a)] with the sympathetic cooling beam turned off. As the heating dynamics proceeds, the spots of individual ions dim and expand, making it difficult to detect individual qubit states. The two columns on the right show the images of the same edge ions and the same central ions with the sympathetic cooling beam turned on. There is no visible change in these images after 800 ms evolution. We can conclude that without the sympathetic cooling, the spots of individual ions quick blur and mix up with each other. This process is fastest for the middle ions with small inter-ion distances, but even for ions on the edges it will finally become difficult to distinguish individual ions. On the other hand, with the sympathetic cooling beam turned on, the ions remain distinguishable and there is no visible change over 800 ms evolution time.

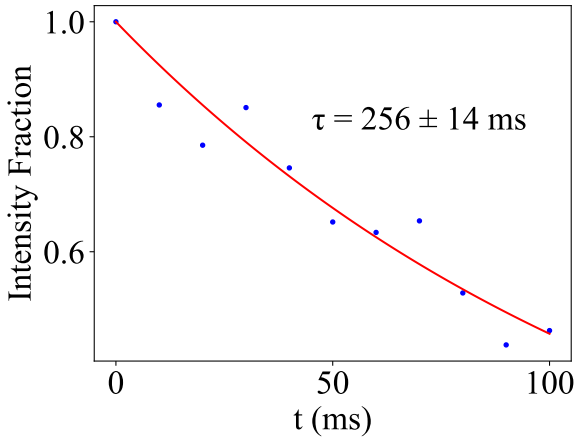

Figure 6.7 The decay of photon counts.

With this basic understanding about how the heating effects damage the qubit state detection, now we apply it to the 218-ion crystal. In Fig. 6.7 we pick up an ion (labeled as ion 1 above) and measure the photon counts in a 5 pixels×5 pixels box around it. With the sympathetic cooling beam turned off, the photon count quickly decays within 100 ms, and we estimate a decay time of $\tau = (256 \pm 14)$ ms from the simplest fitting model of $e^{-t/\tau}$. This decay comes from two effects: as the ion heats up, it is more likely to move outside

the selected region, and it scatters less photons due to the larger Doppler shifts. In the experiment, we use a threshold method to distinguish the bright ($|1\rangle$) and the dark ($|0\rangle$) state. Therefore the drop in the photon count of the bright state will significantly reduce the detection fidelity even before the timescale τ, and is shorter than the coherence time T_2 measured before under sympathetic cooling.

Although we show that sympathetic cooling is critical for the long-time storage of the qubit states in the multi-ion crystal, it is also well-known that the scattered photons from the cooling ions can lead to crosstalk on the storage ions and thus limit the storage lifetime. This is because of the same transition frequency between the cooling ions and the storage ions. Previously, this is solved by using different ion species to encode the two qubit types[17,32-34,38]. In the future, when combined with the dual-type qubit scheme which encodes the data qubits and the ancilla qubits into different clock states of the same ion species, the crosstalk can be suppressed to allow smaller distance between the two qubit types and an enhanced storage lifetime, without the need to manipulate multiple ion species.

To sum up, we have demonstrated the multi-ion storage capacity with sub-second lifetime in a quasi-1D crystal of above 200 ions. This capability to coherently store a large number of qubits for long time is crucial for the quantum computing tasks in the future with deep circuit depth. It is also necessary for ion-photon quantum networks since the entanglement generation between different ion trap modules through photon links is typically much slower than the local gate operations inside individual modules[20].

CHAPTER 7 CONCLUSION AND OUTLOOK

To sum up, we have shown the main processes and techniques used to build a quantum memory based on trapped ions, including the experimental setup, the cryogenic experimental techniques, stable trapping and experimental realization of quantum memory.

The rate of background gas collisions with the ion chain is one of the scaling challenges in an ion-trapped system. Thus, we have constructed an extreme high vacuum environment to reduce pressure of the background gas in this vacuum system. For a newly built cryogenic trap system, the experimental implementation of stable trapping of multiple ions may take most of the project time before some quantum computing or quantum simulation experiments can be carried out. Therefore we spent a lot of time getting stable trapping of 200 ions. In terms of experimental techniques, we have achieved high fidelity initial state preparation and final state detection (the EMCCD-based spatially resolvable detection system allows for minimal crosstalk between different ions with a fidelity of 97%), analyzed and suppressed the sources of noise from mechanical and electrical systems that induce decoherence. Finally, we report the stable trapping of above 200 ions in a zig-zag structure, and demonstrate the combination of the multi-qubit capacity and long storage lifetime by measuring the coherence time of several arbitrarily chosen ions to be on the order of hundreds of milliseconds. We compare the performance of the quantum memory with and without the sympathetic cooling laser, thus unambiguously show the necessity of sympathetic cooling for the long-time storage of multiple ionic qubits.

In the future, we can expect to upgrade various aspects of the cryostat design. To improve the scalability of the system, the implementation of a 2D ion crystal is a brilliant idea and one can try to combine monolithic trap and cryostat. Optimising the structure of the cryostat can further suppress vibration noise. Using laser ablation loading instead of oven loading can help to reduce the temperature and pressure of the background gas. The introduction of individual addressing into cryogenic trap systems can implement high fidelity quantum gate operations between arbitrary two qubits. Developments in cryogenic trap technology could be the future of trapped ion quantum computing.

REFERENCES

[1] Paul W. Electromagnetic traps for charged and neutral particles[J/OL]. Rev. Mod. Phys., 1990, 62: 531-540. https://link.aps.org/doi/10.1103/RevModPhys.62.531.

[2] Benioff P. The computer as a physical system: A microscopic quantum mechanical hamiltonian model of computers as represented by turing machines[J/OL]. Journal of Statistical Physics, 1980, 22(5): 563-591. https://doi.org/10.1007/BF01011339.

[3] Feynman R P. Simulating physics with computers[J/OL]. International Journal of Theoretical Physics, 1982, 21(6): 467-488. https://doi.org/10.1007/BF02650179.

[4] Ladd T D, Jelezko F, Laflamme R, et al. Quantum computers[J/OL]. Nature, 2010, 464(7285): 45-53. https://doi.org/10.1038/nature08812.

[5] Lvovsky A I, Sanders B C, Tittel W. Optical quantum memory[J]. Nature photonics, 2009, 3 (12): 706-714.

[6] Duan L M, Lukin M D, Cirac J I, et al. Long-distance quantum communication with atomic ensembles and linear optics[J]. Nature, 2001, 414(6862): 413-418.

[7] Sangouard N, Simon C, De Riedmatten H, et al. Quantum repeaters based on atomic ensembles and linear optics[J]. Reviews of Modern Physics, 2011, 83(1): 33.

[8] Gottesman D. Theory of fault-tolerant quantum computation[J]. Physical Review A, 1998, 57 (1): 127.

[9] Campbell E T, Terhal B M, Vuillot C. Roads towards fault-tolerant universal quantum computation[J]. Nature, 2017, 549(7671): 172-179.

[10] Huang H L, Wu D, Fan D, et al. Superconducting quantum computing: a review[J]. Science China Information Sciences, 2020, 63: 1-32.

[11] Yang S J, Wang X J, Bao X H, et al. An efficient quantum light–matter interface with sub-second lifetime[J]. Nature Photonics, 2016, 10(6): 381-384.

[12] Wang Y, Li J, Zhang S, et al. Efficient quantum memory for single-photon polarization qubits [J]. Nature Photonics, 2019, 13(5): 346-351.

[13] Ortu A, Holzäpfel A, Etesse J, et al. Storage of photonic time-bin qubits for up to 20 ms in a rare-earth doped crystal[J]. npj Quantum Information, 2022, 8(1): 29.

[14] Lago-Rivera D, Grandi S, Rakonjac J V, et al. Telecom-heralded entanglement between multimode solid-state quantum memories[J]. Nature, 2021, 594(7861): 37-40.

[15] Zhong M, Hedges M P, Ahlefeldt R L, et al. Optically addressable nuclear spins in a solid with a six-hour coherence time[J]. Nature, 2015, 517(7533): 177-180.

[16] Bradley C E, Randall J, Abobeih M H, et al. A ten-qubit solid-state spin register with quantum memory up to one minute[J]. Physical Review X, 2019, 9(3): 031045.

[17] Wang P, Luan C Y, Qiao M, et al. Single ion qubit with estimated coherence time exceeding one hour[J]. Nature communications, 2021, 12(1): 233.

[18] Blinov B B, Moehring D L, Duan L M, et al. Observation of entanglement between a single trapped atom and a single photon[J]. Nature, 2004, 428(6979): 153-157.

[19] Stute A, Casabone B, Schindler P, et al. Tunable ion–photon entanglement in an optical cavity [J]. Nature, 2012, 485(7399): 482-485.

[20] Hucul D, Inlek I V, Vittorini G, et al. Modular entanglement of atomic qubits using photons and phonons[J]. Nature Physics, 2015, 11(1): 37-42.

[21] Bock M, Eich P, Kucera S, et al. High-fidelity entanglement between a trapped ion and a telecom photon via quantum frequency conversion[J]. Nature communications, 2018, 9(1): 1998.

[22] Krutyanskiy V, Meraner M, Schupp J, et al. Light-matter entanglement over 50 km of optical fibre[J]. npj Quantum Information, 2019, 5(1): 72.

[23] Duan L M, Monroe C. Colloquium: Quantum networks with trapped ions[J]. Reviews of Modern Physics, 2010, 82(2): 1209.

[24] Pagano G, Hess P, Kaplan H, et al. Cryogenic trapped-ion system for large scale quantum simulation[J]. Quantum Science and Technology, 2018, 4(1): 014004.

[25] Li B W, Wu Y K, Mei Q X, et al. Probing critical behavior of long-range transverse-field ising model through quantum kibble-zurek mechanism[J]. PRX Quantum, 2023, 4(1): 010302.

[26] Egan L, Debroy D M, Noel C, et al. Fault-tolerant control of an error-corrected qubit[J]. Nature, 2021, 598(7880): 281-286.

[27] Postler L, Heuβen S, Pogorelov I, et al. Demonstration of fault-tolerant universal quantum gate operations[J]. Nature, 2022, 605(7911): 675-680.

[28] Leibfried D, Blatt R, Monroe C, et al. Quantum dynamics of single trapped ions[J]. Reviews of Modern Physics, 2003, 75(1): 281.

[29] Qiao M, Wang Y, Cai Z, et al. Double-electromagnetically-induced-transparency ground-state cooling of stationary two-dimensional ion crystals[J]. Physical Review Letters, 2021, 126(2): 023604.

[30] Feng L, Tan W, De A, et al. Efficient ground-state cooling of large trapped-ion chains with an electromagnetically-induced-transparency tripod scheme[J]. Physical Review Letters, 2020, 125(5): 053001.

[31] Joshi M, Fabre A, Maier C, et al. Polarization-gradient cooling of 1d and 2d ion coulomb crystals[J]. New Journal of Physics, 2020, 22(10): 103013.

[32] Chen J S, Brewer S M, Chou C, et al. Sympathetic ground state cooling and time-dilation shifts in an al 27+ optical clock[J]. Physical Review Letters, 2017, 118(5): 053002.

[33] Blinov B, Deslauriers L, Lee P, et al. Sympathetic cooling of trapped cd+ isotopes[J]. Physical Review A, 2002, 65(4): 040304.

[34] DeMarco B, Schaetz T, Meyer V, et al. Sympathetic cooling of 9 be+ and 24 mg+ for quantum logic[J]. Physical Review A, 2003, 68(4): 042302.

[35] Mao Z C, Xu Y Z, Mei Q X, et al. Experimental realization of multi-ion sympathetic cooling on a trapped ion crystal[J]. Physical Review Letters, 2021, 127(14): 143201.

[36] Brown K R, Harrow A W, Chuang I L. Arbitrarily accurate composite pulse sequences[J]. Physical Review A, 2004, 70(5): 052318.

[37] Bando M, Ichikawa T, Kondo Y, et al. Concatenated composite pulses compensating simultaneous systematic errors[J]. Journal of the Physical Society of Japan, 2012, 82(1): 014004.

[38] Home J P, McDonnell M, Szwer D, et al. Memory coherence of a sympathetically cooled trapped-ion qubit[J]. Physical Review A, 2009, 79(5): 050305.

ACKNOWLEDGEMENTS

衷心感谢导师 ××× 教授和物理系 ×× 副教授对本人的精心指导。他们的言传身教将使我终生受益。

在美国麻省理工学院化学系进行九个月的合作研究期间，承蒙 Robert Field 教授热心指导与帮助，不胜感激。

感谢 ××××× 实验室主任 ××× 教授，以及实验室全体老师和同窗们学的热情帮助和支持！

本课题承蒙国家自然科学基金资助，特此致谢。

声　明

本人郑重声明：所呈交的学位论文，是本人在导师指导下，独立进行研究工作所取得的成果。尽我所知，除文中已经注明引用的内容外，本学位论文的研究成果不包含任何他人享有著作权的内容。对本论文所涉及的研究工作做出贡献的其他个人和集体，均已在文中以明确方式标明。

签　名：_____ 日　期：_____

RESUME

个人简历

197× 年 ×× 月 ×× 日出生于四川 ×× 县。

1992 年 9 月考入 ×× 大学化学系 ×× 化学专业，1996 年 7 月本科毕业并获得理学学士学位。

1996 年 9 月免试进入清华大学化学系攻读 ×× 化学博士至今。

在学期间完成的相关学术成果

学术论文

[1] Yang Y, Ren T L, Zhang L T, et al. Miniature microphone with silicon-based ferroelectric thin films[J]. Integrated Ferroelectrics, 2003, 52:229-235.

[2] 杨轶, 张宁欣, 任天令, 等. 硅基铁电微声学器件中薄膜残余应力的研究 [J]. 中国机械工程, 2005, 16(14):1289-1291.

[3] 杨轶, 张宁欣, 任天令, 等. 集成铁电器件中的关键工艺研究 [J]. 仪器仪表学报, 2003, 24(S4):192-193.

[4] Yang Y, Ren T L, Zhu Y P, et al. PMUTs for handwriting recognition. In press[J]. (已被 Integrated Ferroelectrics 录用)

专利

[1] 任天令, 杨轶, 朱一平, 等. 硅基铁电微声学传感器畴极化区域控制和电极连接的方法: 中国, CN1602118A[P]. 2005-03-30.

[2] Ren T L, Yang Y, Zhu Y P, et al. Piezoelectric micro acoustic sensor based on ferroelectric materials: USA, No.11/215, 102[P]. (美国发明专利申请号.)

COMMENTS FROM THESIS SUPERVISOR

论文提出了……

RESOLUTION OF THESIS DEFENSE COMMITTEE

论文提出了……

论文取得的主要创新性成果包括：

1. ……

2. ……

3. ……

论文工作表明作者在 ××××× 具有 ××××× 知识，具有 ×××× 能力，论文 ××××，答辩 ××××。

答辩委员会表决，（× 票/一致）同意通过论文答辩，并建议授予 ×××（姓名）×××（门类）学博士/硕士学位。